Interaction between Static Magnetic Islands and Interchange Modes in Heliotron Plasmas

Kinya Saito

DOCTOR OF PHILOSOPHY

Department of Fusion Science
School of Physical Science
The Graduate University for Advanced Studies

2011

Abstract

Nonlinear interaction between static magnetic islands generated by an external field and a resistive interchange mode driven by pressure gradient is investigated in straight heliotron configurations by means of a numerical method based on the reduced magnetohydrodynamics (MHD) equations. For the comprehensive understanding of the interaction, two aspects are studied by utilizing different MHD equilibria. One is effects of the interchange mode on the change of the static island and the other is effects of the static island on the growth of the interchange mode.

Firstly, the former interaction aspect is studied with an equilibrium corresponding to nested magnetic surfaces. In this case, the interchange mode grows in spite of existence of a static magnetic island. The island width is changed in the nonlinear saturation phase of the interchange mode. The situation of the increase or decrease of the width depends on whether the diffusion of the equilibrium pressure in the direction parallel to the magnetic field is taken into account or not. In the case without the effect of the diffusion of the equilibrium pressure, there exist two solutions corresponding to the increase and the decrease of the island width. In this case, in spite of the nonlinear interaction, the total poloidal flux is approximately given by the linear sum of the poloidal flux generated by the interchange mode without a static island and the external poloidal flux for the generation of the static island. In the case with the effect of the diffusion of the equilibrium pressure, there exists only one solution corresponding to the increase of the width. This is due to the fact the parallel diffusion term generates a pressure term corresponding to the increase of the island width.

Next, the latter interaction aspect is studied. For this study, equilibria including static magnetic islands are necessary because the equilibrium pressure profile consistent with the magnetic islands has possibility to affect the stability of the interchange mode. We have developed a numerical code (FLEC) to calculate the equilibria and found that there exist two kinds of solutions. One is the equilibrium of which the pressure profile is flat at not only the O-point but also the X-point. In this case, the pressure gradient

is continuous at the separatrix. The other is the equilibrium of which the pressure profile is flat at the O-point and steep at the X-point. In this case, the pressure gradient is discontinuous at the separatrix of the magnetic island. The finite beta has a contribution to increase the island width.

Since it is known that the pressure profile with annular local flat structure around the resonant surface have a stabilizing contribution to the interchange mode, effects of the static island on the interchange mode is studied for the equilibrium with the steep gradient at the X-point. The linear growth rate of the interchange mode is decreased and the saturation level is reduced as the island width is increased. The mode is completely stabilized when the width exceeds threshold value. In the case that interchange modes are unstable in an equilibrium with a thin island width, there are two cases of the increase and the decrease of the island width in the nonlinear saturation of interchange modes as obtained in the study for the former interaction aspect.

Acknowledgements

First of all, I would like to thank Professor Katsuji Ichiguchi, who gave me the opportunity to study the plasma physics, fruitful guidance and warm encouragement throughout my doctoral course. I would also like to acknowledge Dr. Ryuichi Ishizaki for his valuable suggestion. This thesis is based on the discussion with them.

I would like to thank Dr. Yasuhiro Suzuki (NIFS) and Dr. Ryutaro Kanno (NIFS). They gave me useful suggestions and lots of comments for numerical calculation of magnetohydrodynamics equilibria including a static magnetic island. I also thank Emeritus Professor Nobuyoshi Ohyabu for his guidance.

I would also like to extend my appreciation to Professor Kiyomasa Watanabe (NIFS) and Dr. Satoru Sakakibara (NIFS). They provided me the LHD experimental data and allowed me to use the experimental data for my presentation.

I express my gratitude for Dr. Yoshiro Narushima (NIFS) and Dr. Shinichiro Toda (NIFS). A seminar with them helped me establish a firm foundation for ideal magnetohydrodynamics.

I would also like to acknowledge Professor Hideo Sugama (NIFS), Dr. Masaru Furukawa (Tokyo Univ.) and Professor Fumimichi Sano (Kyoto Univ.) for a lot of suggestions.

Dr. Seikichi Matsuoka (NIFS), Dr. Motoki Nakata (JAEA), Dr. Kunihiro Ogawa (Nagoya Univ.), Mr. Kohki Kumagai (IHI), Dr. Seiya Nishimura (NIFS) and Dr. Ryousuke Seki (NIFS) are acknowledged for their advise and suggestions of my thesis. Furthermore, I thank Dr. (to be) Akiyoshi Murakami (Sokendai), Dr. (to be) Shinya Maeyama (Tokyo Tech.) and Mr. Masahito Naito (SANSHODO) for their encouragement.

Finally, I would like to express my acknowledgments to my parents; Yoshikazu Saito and Chizuko Saito. They support me all the time.

Contents

Chapter 1

Introduction

In magnetic confinement of fusion plasmas, existence of nested magnetic surfaces is desirable for the good confinement. However, error magnetic fields originated from misalignment of field coils and the terrestrial magnetism induce static magnetic islands. The static islands have a possibility to degrade the plasma confinement substantially. Therefore, it is one of the essential themes in magnetic confinement systems to understand how such islands grow or decay in finite beta plasmas. Hence, such island behavior has been studied extensively in both tokamaks and heliotrons [1]. In tokamaks, a lot of efforts are paid for the control of the edge localized mode with the island generation by the application of resonant magnetic perturbations (RMP) [2]. In heliotrons, the growth and the decay of the static magnetic islands at finite beta are studied. Particularly, in the large helical device (LHD) [3], which is the largest heliotron device, the local island divertor (LID) coils are installed in the system [4]. The RMP or the error field can be generated actively by the currents in the LID coils and utilized for the study of the static islands behavior. The static magnetic islands are generated by the error field mainly with (m, n)=(1,1) and they affect plasma confinement and magnetohydrodynamics (MHD) properties. Here m and n are the poloidal and toroidal mode numbers, respectively. Spontaneous change in the islands and the influence on the confinement are analyzed in the experiments by controlling the static islands. Ohyabu et al. [5] studied the beta dependence of the self-healing of the islands. They found that the onset beta value of the self-healing is increased and nearly proportional to the externally imposed resonant error field. Narushima et al. [6] examined the dependence of the self-healing on the beta and the collisionality. They also showed that the sign of the perturbed magnetic field reversed suddenly when the beta exceeded the critical value of the self-healing.

The magnetic islands can also be generated by resistive MHD instabilities. In the heliotron configurations such as LHD, a net toroidal current is not needed for the generation of the confinement field. Therefore, tearing modes are not excited except a special case where a net toroidal current with a quite peaked profile flows in the plasma [7]. Instead, a magnetic hill usually exists in the plasma confinement region. Therefore, a resistive interchange mode driven by a pressure gradient can be excited in the configurations. Since the interchange modes can cause a collapse of the plasma [8], the stability control is important for a good confinement at high beta.

Thus, the interchange modes are the crucial MHD modes in the heliotron configurations, and therefore, a lot of theoretical analyses have been done for the behavior. Particularly, Ichiguchi et al. and Ishizawa et al. [9–11] showed that magnetic islands are generated by nonlinear saturation of interchange modes numerically. Therefore, it is expected that the change of the static island width is caused by the interchange modes. On the other hand, magnetic islands have a potential to affect the stability of interchange modes. That is, the magnetic islands and the interchange modes can interact with each other.

However, comprehensive theoretical study about the direct interaction between the interchange mode and the static islands has not been carried out. Only a few works treated the dynamics of the interchange mode in the existence of the static islands. Unemura et al. [12] discussed the variation in the island width and the pressure profile due to the nonlinear evolution of the interchange mode in a straight heliotron configuration. However, they used multi-helicity perturbations and evaluated the island width in transitional regions of the time evolution. Garcia et al. [13, 14] also studied the nonlinear coupling of a static magnetic island and the interchange mode. In the studies, the diamagnetic effect is involved to investigate the shear flow effect. Because of the diamagnetic flow, the island width is oscillating even in the saturation state of the interchange mode. Therefore, the fundamental mechanism in the interaction of the islands and the interchange mode is difficult to be understood from these previous works.

Thus, we analyze the fundamental interaction between the static magnetic islands and the dynamics of the interchange mode numerically based on the reduced MHD equations [15]. A straight LHD configuration is employed as the magnetic configuration to see the interaction clearly. In order to investigate the fundamental interaction, we focus on the interaction between the static islands with the mode number of (m, n)=(1,1) and the interchange mode with the same mode number.

Two aspects of the interaction are studied. One is the effect of the interchange mode on the change of the static island and the other is the effect of the existence of the static island on the growth of the interchange mode. We examine these aspects separately by employing two procedures with different pressure profiles.

For the analysis of the former aspect, a pressure profile corresponding to a nested magnetic surface is employed. In this case, we obtain an equilibrium with the pressure profile which is unstable for the interchange mode, firstly. Therefore, effects of the static island on the equilibrium quantities are not included. Then, both of an error field generating a static island and the perturbation of the interchange mode are imposed simultaneously. Since there exists a finite pressure gradient inside the separatrix of the island, the interchange mode grows. In the growth, the interchange mode interacts with the static island nonlinearly. We follow the nonlinear evolution of the mode and evaluate the change of the island in the saturation phase of the nonlinear evolution. This procedure is suitable for the study of the effect of the interchange mode on the static island because the growth of the mode is guaranteed. This procedure is also employed in the studies of Ref. [12–14].

For the analysis of the latter aspect, we employ a pressure profile corresponding to the island geometry. When the beta value is increased gradually from the vacuum magnetic surfaces without the self-healing of the island, an equilibrium is achieved with a pressure profile of which the gradient inside the separatrix is reduced. In the equilibrium, the growth of the interchange mode is affected by the pressure profile. In order to study the island effect on the mode, we develop a numerical code to calculate such an equilibrium with the pressure profile corresponding to the island geometry. Since the behavior of the interchange mode is examined with the reduced MHD equations, the equilibrium equations have to correspond to the reduced MHD equations, and therefore, they are coupled equations for the pressure and the poloidal magnetic flux.

The development of numerical codes to solve an equilibrium including magnetic islands has a long history. The pioneering work is the code developed by Chodura and Schlüter [16]. In this code, an equilibrium is obtained by minimizing the potential energy with a friction method on cylindrical coordinates based on the variational principle. Hender et al. developed the NEAR code by improving the Chodura-Schlüter code with the employment of vacuum flux surfaces for the reference coordinates [17]. Recently, the PIES code [18] and the HINT code [19, 20] or the HINT2 code [21] have been developed and widely used for the stellarator equilibrium studies. Both codes are

based on an iteration scheme of two steps. In the first step, the pressure profile consistent with the magnetic geometry with the magnetic field fixed. In the second step, the magnetic field satisfying the force balance equation is obtained with the pressure fixed. In the present work, we basically employ the two-step scheme.

The treatment in each step is different between the PIES and the HINT codes. In the first step of the PIES code, the pressure satisfying the equation of $\mathbf{B} \cdot \nabla P = 0$ for a given magnetic field $\mathbf{B}$ is obtained with the field line tracing. In the second step, the plasma current is calculated by using this pressure P and the field is obtained by solving the Ampére's law directly. Then, quasi magnetic coordinates are constructed with the field, and the next iteration is operated on the coordinates. The HINT code is based on the numerical scheme which was developed by Park et al. [19] for the reduced MHD equations, and is extended to the full MHD equations. Especially, the coordinate system twisted along the toroidal direction is employed for saving calculation regions. In the first step, the pressure satisfying $\mathbf{B} \cdot \nabla P = 0$ is obtained as in the PIES code. The code by Park et al. and the original HINT code solve the equation by making the magnetic sound wave decay. The HINT2 code is improved so as to solve the equation $\mathbf{B} \cdot \nabla P = 0$ directly by tracing the field lines. In the second step, a relaxation precess of the field is conducted with the equation of motion and the Faraday's law with P fixed for obtaining the magnetic field satisfying the force balance condition.

In the present study for the latter effect, two kinds of numerical approach are employed in developing the equilibrium code. Both of them are based on the two-step scheme employed in the code by Park et al. and the HINT code, however, the numerical approach in each step is different. One is the combination of a diffusion equation for the pressure and an ordinary equation for the force balance. The other is the combination of a field line tracing method for the pressure and a relaxation method. The equilibrium solutions are different depending on the approach, particularly in the structure of the pressure profile.

By utilizing the equilibrium solutions, we examine the dependence of the linear stability and the nonlinear saturation of the interchange mode on the island width. Particularly, we focus on the effect of the existence of the finite pressure gradient at the X-point, because the interchange mode is driven by the pressure gradient. The stabilization effect of the annular flat structure of the pressure profile was analyzed by Ichiguchi et al. [22, 23]. However, the effect of the local flat structure with a finite gradient at the X-point has not been examined. Thus, we study the dependence of the linear growth rate and the saturation level on the island width by utilizing the

equilibrium with such structure. We also analyze the effect of the nonlinear saturation of the interchange mode on the change of the island structure as well.

The framework of this thesis is shown in Fig.1.1. In Chapter 2, the reduced MHD equations used in the analysis of the interchange mode dynamics and the introduction of the static island are explained. In Chapter 3, the results of the effect of the interchange mode on the change of the static island with the pressure profile corresponding to the nested magnetic surfaces are shown. We mainly focus on the changes of the width and the phase of the island in the saturation of the interchange mode. We also show the dependence of the island change on the effect of the equilibrium pressure diffusion in the parallel direction of the field line and discuss the mechanism of the island behavior. In Chapter 4, the equilibrium calculation including the static island is discussed. The two approaches of the equilibrium calculation are explained. The obtained solutions are compared with each other and the reason of the difference is discussed. In Chapter 5, the effect of the existence of the static island in the equilibrium on the behavior of the interchange mode is studied. We discuss the dependence of the linear stability and the nonlinear saturation level. In Chapter 6, conclusions are given.

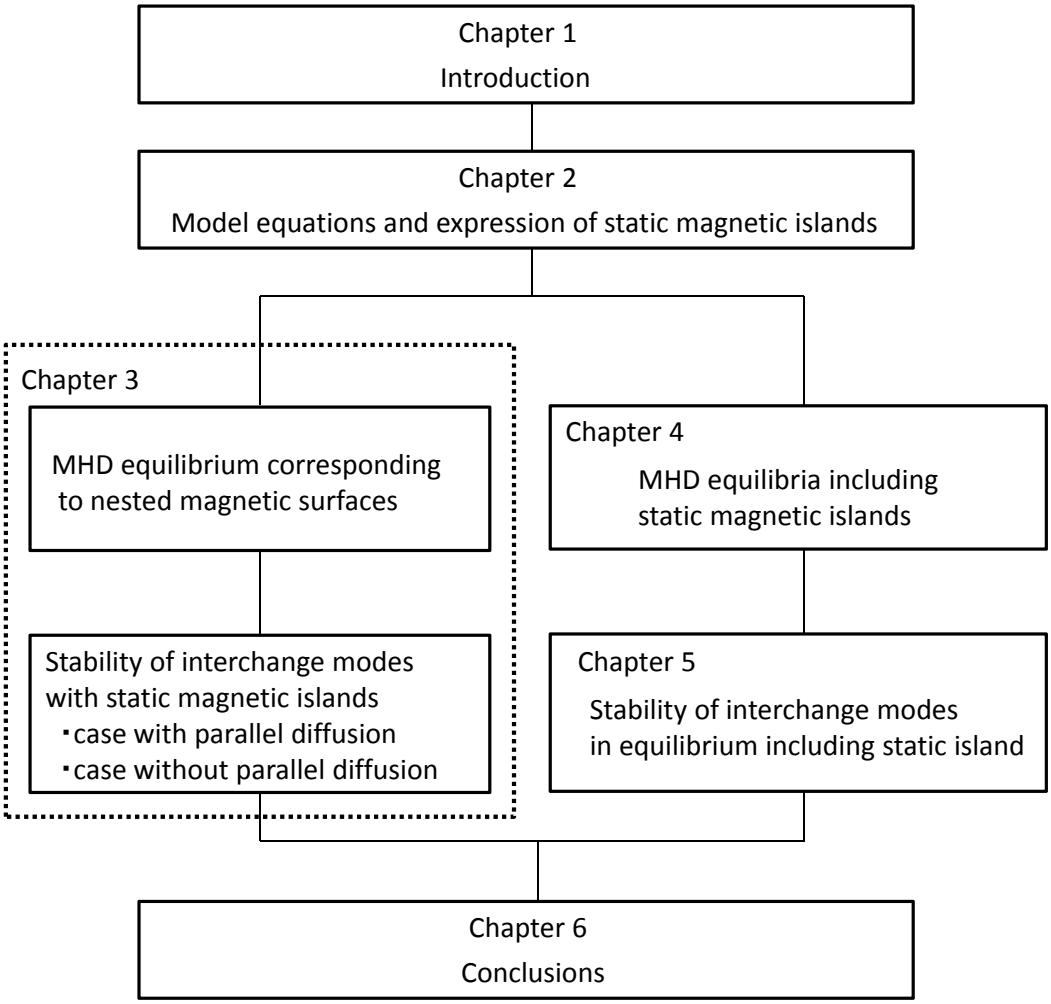

Figure 1.1: Framework of this thesis.

Chapter 2

Model Equations and Expression of Static Magnetic Islands

2.1 Reduced MHD equations

We study the interaction between the static islands and the interchange mode with (m, n)=(1,1). For the behavior of the plasma with such low mode numbers, the toroidally averaged field line curvature plays a dominant role. Therefore, the reduced MHD equations [15] are useful for this analysis, which are the equations for poloidal magnetic flux Ψ, stream function Φ and plasma pressure P. In a straight heliotron configuration, the normalized reduced MHD equations with the cylindrical coordinates (r,θ,z) are given by the Ohm's law,

$$\frac{\partial \Psi}{\partial t} = -\mathbf{B} \cdot \nabla \Phi + \frac{1}{S} J_z, \tag{2.1}$$

the vorticity equation,

$$\frac{dU}{dt} = -\mathbf{B} \cdot \nabla J_z + \frac{1}{2\epsilon^2} \nabla \Omega \times \nabla P \cdot \mathbf{z} + \nu \nabla_\perp^2 U \tag{2.2}$$

and the plasma pressure equation,

$$\frac{dP}{dt} = \kappa_\perp \nabla_\perp^2 P + \kappa_\parallel (\mathbf{B} \cdot \nabla)(\mathbf{B} \cdot \nabla) P. \tag{2.3}$$

The magnetic field $\mathbf{B}(r, \theta, z)$ is expressed as

$$\mathbf{B}(r, \theta, z) = \mathbf{z} + \mathbf{z} \times \nabla \Psi(r, \theta, z), \tag{2.4}$$

where $\mathbf{z}$ denotes the unit vector in the z direction. Here Jz, U and $\nabla\Omega$ denote the current density in the z direction, the vorticity in the negative z direction and the

averaged magnetic field line curvature, respectively. The convective time derivative is given by

$$\frac{d}{dt} = \frac{\partial}{\partial t} + \mathbf{v}_\perp \cdot \nabla. \tag{2.5}$$

Here the velocity $\mathbf{v}_\perp$ is given by

$$\mathbf{v}_\perp = \nabla_\perp \Phi \times \mathbf{z}, \tag{2.6}$$

where the operator $\nabla_\perp$ is defined as

$$\nabla_\perp = \nabla - \mathbf{z}\left(\frac{\partial}{\partial z}\right). \tag{2.7}$$

The resistivity, the viscosity, the perpendicular and parallel heat conductivities are introduced with the coefficients of S, ν, $\kappa_\perp$ and $\kappa_\parallel$, respectively. Here, S denotes the magnetic Reynolds number expressed as

$$S = \tau_R/\tau_A, \tag{2.8}$$

where the Alfvén time τ_A and the resistive diffusion time τ_R are given by $\tau_A = R_0\sqrt{\mu_0\rho}/B_0$ and $\tau_R = \mu_0 a^2/\eta$, respectively. The quantities R_0, μ_0, ρ, B_0, a, η and ϵ denote the major radius of the corresponding torus, the vacuum permeability, the mass density, the magnetic field at the magnetic axis, the plasma radius, the resistivity and the inverse aspect ratio, respectively. In this study, we employ $\epsilon = 0.16$, which corresponds to the LHD plasma. The quantities $(r, z, t, \Psi, \Phi, P, U, Jz, \nu, \kappa_\perp, \kappa_\parallel)$ are normalized by (a, R_0 , τ_A, a^2B_0/R_0, a^2/τ_A, $B_0^2/2\mu_0$, $1/\tau_A$, $B_0/\mu_0 R_0$, $\rho a^2/\tau_A$, a^2/τ_A, R_0^2/τ_A), respectively.

We analyze the interaction by tracing the time evolution of the interchange mode with the NORM code [9] numerically. The original NORM code solves the reduced MHD equations without the effect of the static islands. The equations are formulated in the time evolution form of the perturbed variables in the following way:

$$\frac{\partial \tilde{\Psi}}{\partial t} = -\mathbf{B}\cdot\nabla\tilde{\Phi} + \frac{1}{S}\tilde{J}_z, \tag{2.9}$$

$$\frac{d\tilde{U}}{dt} = -(\mathbf{B}\cdot\nabla\tilde{J}_z + \tilde{\mathbf{B}}\cdot\nabla J_{z\,eq}) + \frac{1}{2\epsilon^2}\nabla\Omega_{eq}\times\nabla\tilde{P}\cdot\mathbf{z} + \nu\nabla_\perp^2\tilde{U} \tag{2.10}$$

and

$$\frac{d\tilde{P}}{dt} = (\mathbf{z}\times\nabla\tilde{\Phi})\cdot\nabla P_{eq} + \kappa_\perp\nabla_\perp^2\tilde{P} + \kappa_\parallel(\mathbf{B}\cdot\nabla)(\mathbf{B}\cdot\nabla)\tilde{P}. \tag{2.11}$$

The subscript of ' eq ' refers to the equilibrium quantity. The tilde means the perturbed quantity. The magnetic field $\mathbf{B}$ is written as

$$\mathbf{B} = \mathbf{B}_{eq} + \tilde{\mathbf{B}}, \tag{2.12}$$

where $\mathbf{B}_{eq}$ and $\tilde{\mathbf{B}}$ are defined as

$$\mathbf{B}_{eq} = \mathbf{z} + \mathbf{z} \times \nabla \Psi_{eq} \quad and \quad \tilde{\mathbf{B}} = \mathbf{z} \times \nabla \tilde{\Psi}, \tag{2.13}$$

respectively. Here, $\tilde{J}_z$ and $\tilde{U}$ are expressed as

$$\tilde{J}_z = \nabla_\perp^2 \tilde{\Psi} \quad and \quad \tilde{U} = \nabla_\perp^2 \tilde{\Phi}, \tag{2.14}$$

respectively, where $\nabla_\perp^2$ is given by

$$\nabla_\perp^2 = \frac{1}{r}\frac{\partial}{\partial r}\left(r\frac{\partial}{\partial r}\right) + \frac{1}{r^2}\frac{\partial^2}{\partial \theta^2}. \tag{2.15}$$

For the study of the interaction, we modify Eqs.(2.9)-(2.11) so as to include the effects of the islands. The modified equations are expressed in Chapter 3 and 5.

We study the direct interaction between the static island with the mode number of $(m, n) = (1, 1)$ and the interchange mode with same mode number. In order to see the interaction clearly, we assume that the perturbations have a single helicity with $n/m = 1/1$ as follows:

$$\tilde{\Psi}(r, \theta, z) = \sum_{n=0, m=n}^{N_{pe}} \tilde{\Psi}_{m,n}, \quad \tilde{\Psi}_{m,n} = \hat{\Psi}_{m,n}(r)\cos(m\theta - nz), \tag{2.16}$$

$$\tilde{\Phi}(r, \theta, z) = \sum_{n=0, m=n}^{N_{pe}} \tilde{\Phi}_{m,n}, \quad \tilde{\Phi}_{m,n} = \hat{\Phi}_{m,n}(r)\sin(m\theta - nz), \tag{2.17}$$

$$\tilde{P}(r, \theta, z) = \sum_{n=0, m=n}^{N_{pe}} \tilde{P}_{m,n}, \quad \tilde{P}_{m,n} = \hat{P}_{m,n}(r)\cos(m\theta - nz), \tag{2.18}$$

where " $\wedge$ " means the Fourier coefficients. Here, N_{pe} denotes the highest mode number used in the numerical calculation. In this study, we employ $N_{pe} = 30$.

The NORM code solves Eqs.(2.9)-(2.11) as an initial value problem. As the initial perturbations for $\hat{X}_{m,n} = (\hat{\Psi}_{m,n}, \hat{\Phi}_{m,n}, \hat{P}_{m,n})$, the function of

$$\hat{X}_{m,n} = \sigma f(r) \tag{2.19}$$

is employed. Here, σ denotes the sign taking the value of +1 or -1 and $f(r)$ should be a small and arbitrary function except eigenfunctions. In this study, the function of

$$f(r) = 10^{-16}\left\{1 - 4\left(r - \frac{1}{2}\right)^2\right\}^2 \tag{2.20}$$

is used.

We monitor the time evolution of the these quantities to know how the mode grows. For this purpose, the kinetic energy E_K and the magnetic energy E_M are calculated, where E_K and E_M are given by

$$E_K = \sum_{n=0,m=n}^{N_{pe}} E_K^{m,n}, \quad E_K^{m,n} = \frac{1}{2}\int |\nabla_\perp \Phi_{m,n} \sin(m\theta - nz)|^2 dV \tag{2.21}$$

and

$$E_M = \sum_{n=0,m=n}^{N_{pe}} E_M^{m,n}, \quad E_M^{m,n} = \frac{1}{2}\int |\nabla_\perp \Psi_{m,n} \cos(m\theta - nz)|^2 dV, \tag{2.22}$$

respectively. Here, $\int dV$ denotes the integral over the plasma volume. The growth rate of the interchange mode γ is calculated from E_K as

$$\gamma = \frac{1}{2}\frac{1}{E_K}\frac{dE_K}{dt}. \tag{2.23}$$

2.2 External poloidal flux

The static island generated by an error field is incorporated by assuming that the (m, n)=(1,1) component of the poloidal flux has a finite value at the boundary, $r = 1$. Here, we introduce an external poloidal flux $\Psi_{m,n}^{ext}$ given by

$$\Psi_{m,n}^{ext}(r, \theta, z) = \hat{\Psi}_{m,n}^{ext}(r) \cos(m\theta - nz). \tag{2.24}$$

Since the external poloidal flux $\Psi_{m,n}^{ext}$ does not induce any current density, $\Psi_{m,n}^{ext}$ satisfies the equation

$$\nabla_\perp^2 \Psi_{m,n}^{ext} = 0 \tag{2.25}$$

with the boundary conditions,

$$\hat{\Psi}_{m,n}^{ext}(r = 0) = 0 \tag{2.26}$$

and

$$\hat{\Psi}_{m,n}^{ext}(r = 1) = \Psi_b = constant. \tag{2.27}$$

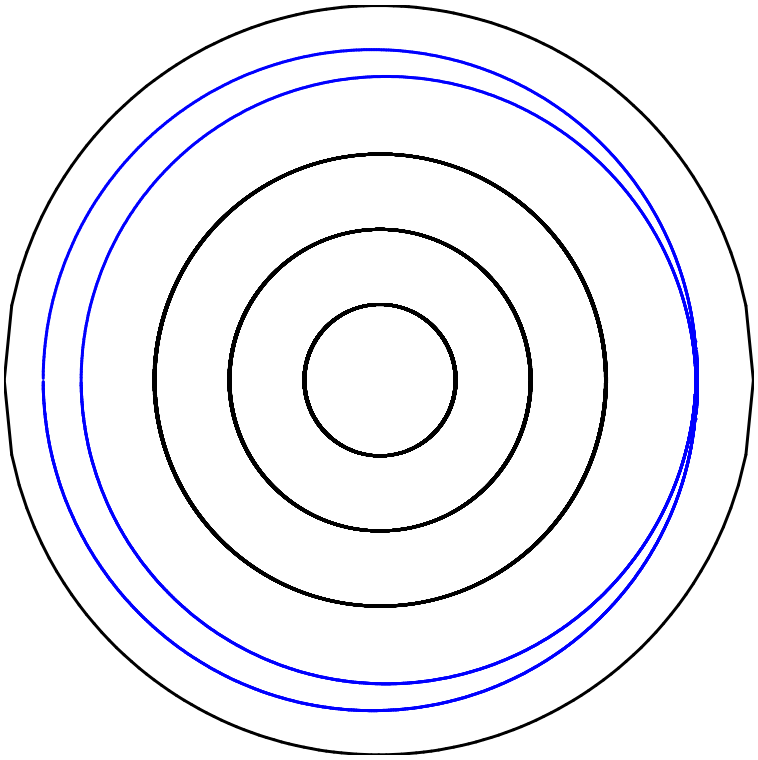

Figure 2.1: Magnetic surfaces for $\Psi_b = +2.0\times10^{-3}$. Blue line indicates the separatrix of the island. The island width is 1.01×10^{-1} normalized by plasma radius.

Here, Ψ_b denotes the external poloidal flux at $r = 1$. Substituting Eqs.(2.15) and (2.24) to Eq.(2.25), Eq.(2.25) becomes

$$\frac{d^2\hat{\Psi}^{ext}_{m,n}}{dr^2} + \frac{1}{r}\frac{d\hat{\Psi}^{ext}_{m,n}}{dr} - \frac{m^2}{r^2}\hat{\Psi}^{ext}_{m,n} = 0. \tag{2.28}$$

The solution of Eq.(2.28) is the linear combination of r^m and r^{-m}. In the case of $(m, n) = (1, 1)$, $\Psi^{ext}_{1,1}(r)$ is given by

$$\Psi^{ext}_{1,1} = \hat{\Psi}^{ext}_{1,1}(r)\cos(\theta - z), \qquad \hat{\Psi}^{ext}_{1,1}(r) = \Psi_b r. \tag{2.29}$$

Figure 2.1 shows magnetic surfaces for $\Psi_b = +2.0 \times 10^{-3}$. Blue line indicates the separatrix of the island. The island width is 1.01×10^{-1} normalized by plasma radius. The static island width can be controlled by changing the value of Ψ_b.

Chapter 3

Effects of Interchange modes on Behavior of Static Magnetic Islands

3.1 Introduction

The effect of the interchange modes on the change of the static islands is studied in this Chapter. In order to understand the effect clearly, we assume an MHD equilibrium having nested magnetic surfaces firstly, then we impose the static island and perturbations of the interchange mode. We obtain the equilibrium quantities by averaging the three-dimensional equilibrium quantities based on the modified stellarator expansion method [24]. Such a treatment of the static island is also utilized in Ref. [12–14]. This situation may be close to the experiment by Sakakibara et al. [25]. They observed a collapse in the profile of the electron temperature (T_e). The T_e profile had a finite gradient at the $\iota = 1$ surface before the collapse in spite of that a natural error field with $(m, n) = (1, 1)$ existed, where ι indicates the rotational transform. The formation of local flat structure is observed in the T_e profile during the collapse at the $\iota = 1$ surface. This observation may indicate the static island appeared when an instability occurred.

We focus on the change of the island width and the island phase after the nonlinear saturation of the interchange mode. For this purpose, we trace the nonlinear time evolution of the interchange mode by using the NORM code. The mechanism of the changes in the island by the nonlinear saturation is discussed. As a general property of the interchange mode, the linear growth rate is increased with the mode number in the case without the dissipation effects of viscosity and heat conductivity. Inclusion

of the dissipations reduces the growth rate the more effectively for the higher mode number. Since we study the interaction between the interchange mode and the static island with the mode number of $(m, n) = (1, 1)$, we choose appropriate coefficients of the dissipations so that the (m, n)=(1,1) mode has the largest growth rate in the single helicity perturbations.

We also study the effect of the heat conductivity for the equilibrium pressure in the direction parallel to the magnetic field. This conductivity gives a qualitative difference to the island behavior because the conductivity term is an inhomogeneous term in the reduced MHD equations. This term generates an initial perturbation of the interchange mode.

This chapter is organized as follows. In Section 3.2, the equilibrium and the linear analysis are described, and then, the change of the magnetic island in the nonlinear evolution of the interchange mode is discussed. In Section 3.3, the effect of parallel heat conductivity for equilibrium pressure on the island behavior is analyzed. In Section 3.4, a summary is given.

3.2 Change of magnetic island in nonlinear evolution of interchange modes

3.2.1 Equilibrium and linear analysis

We use a straight heliotron equilibrium corresponding to the LHD configuration with the vacuum magnetic axis located at 3.6m. The equilibrium is constructed by utilizing a three-dimensional equilibrium, which is calculated with the VMEC code [26] under the no net toroidal current and the free boundary conditions. We employ the equilibrium pressure profile given by

$$P_{eq} = \beta_0 (1 - r^4)^2. \tag{3.1}$$

Here, the beta value at the axis of $\beta_0 = 4.0\%$ is employed. Figure 3.1 shows the profiles of P_{eq}, ι and Ω_{eq}. The profile of Ω_{eq} is given by [24]

$$\Omega_{eq}(r) = \frac{1}{4\pi^2} \int_0^{2\pi} d\theta \int_0^{2\pi} d\zeta \left(\frac{R}{R_0}\right)^2 \left(1 + \frac{|\mathbf{B}_{eq}^{3D} - \overline{\mathbf{B}_{eq}^{3D}}|^2}{B_0^2}\right), \tag{3.2}$$

where ζ and R are the toroidal angle and the major radius, respectively. Here, $\mathbf{B}_{eq}^{3D}$ denotes the three-dimensional equilibrium field. The bar denotes the quantity averaged

toroidally over a field period. Dashed lines show the position of the rational surface with $\iota = 1$. The surface is located at $r = 0.85$ where a substantial pressure gradient exists. The gradient of Ω_{eq} is positive at the surface, which corresponds to a bad curvature of the field line and indicates a potential to drive a resistive interchange mode.

For the study of the interaction with the (m, n)=(1,1) island, the (m, n)=(1,1) component in the interchange mode has to be dominant in the nonlinear state. In order to obtain this situation, we determine the dissipation parameters of ν, $\kappa_\perp$ and $\kappa_\parallel$ so that the component of (m, n)=(1,1) has the largest linear growth rate. We also employ a high resistivity to enhance the effect of the interchange mode. The NORM code is also utilized for the linear analysis. As the initial perturbations, Eq.(2.19) is employed. As the result of the linear mode analysis, the parameters of

$$S = 10^4, \nu = 8.0 \times 10^{-5}, \kappa_\perp = 10^{-5}, \kappa_\parallel = 1.0 \tag{3.3}$$

are found to be suitable for the present analysis. Figure 3.2 shows the dependence of γ given by Eq.(2.23) on n for $\Psi_b = 0$ and $\sigma = +1$. Only the $n = 1$ and $n = 2$ modes are unstable, and the others are stable. The growth rate of the $n = 1$ mode is 1.9 times larger than that of the $n = 2$ mode. Figure 3.3 shows the linear eigenfunctions of the $n = 1$ mode. The poloidal flux $\hat{\Psi}_{1,1}$ is a nearly odd function with respect to the resonant surface of $\iota = 1$. The stream function $\hat{\Phi}_{1,1}$ and the pressure $\hat{P}_{1,1}$ are nearly even functions, both of which are localized around the resonant surface. These eigenfunctions show typical mode structures of the resistive interchange mode. In the change of σ, the sign of the eigenfunctions is opposite and the growth rate is unchanged because they are linear solutions.

3.2.2 Behavior of interchange mode without static magnetic islands

Before the discussion of the case with the static islands, we examine the dynamics of interchange modes under no static island. In the study of this Section, Eqs.(2.9)-(2.11) are utilized. Figure 3.4 shows the nonlinear time evolution of the kinetic energy and the magnetic energy for $\Psi_b = 0$ and $\sigma = +1$.

After the linear growth($t \gtrsim 8500\tau_A$), a steady state appears. The $n = 1$ component is dominant in the steady state. Figure 3.5 shows the mode structure of the $n = 1$ component at $t = 10000\tau_A$. The structure is similar to that of the linear eigenfunctions

(a)

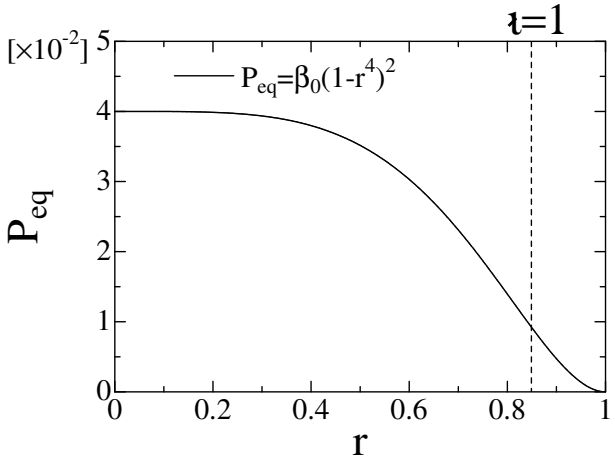

(b)

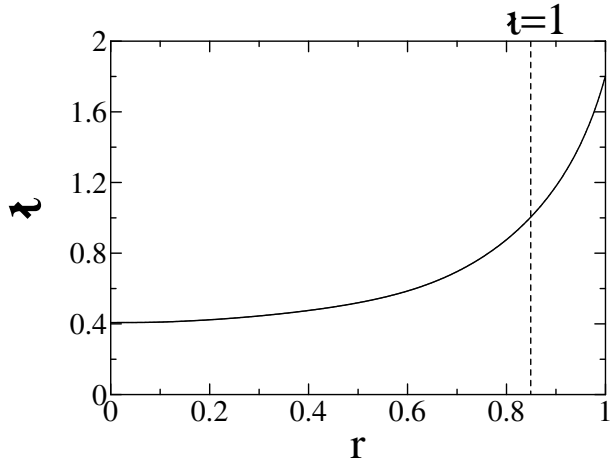

(c)

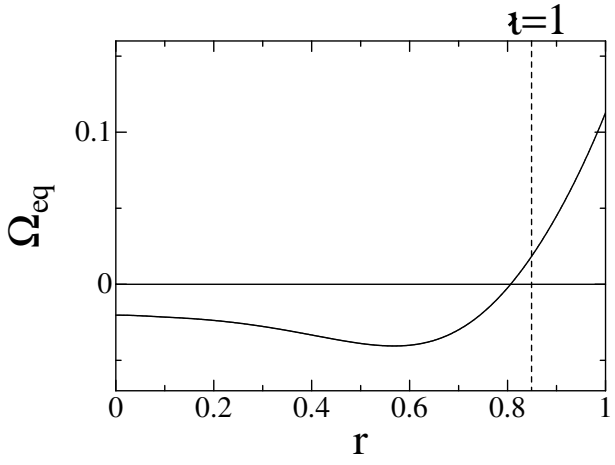

Figure 3.1: Profiles of (a) pressure, (b) rotational transform and (c) average field line curvature in the straight heliotron equilibrium at $\beta_0 = 4.0\%$. Dashed lines show position of the resonant surface.

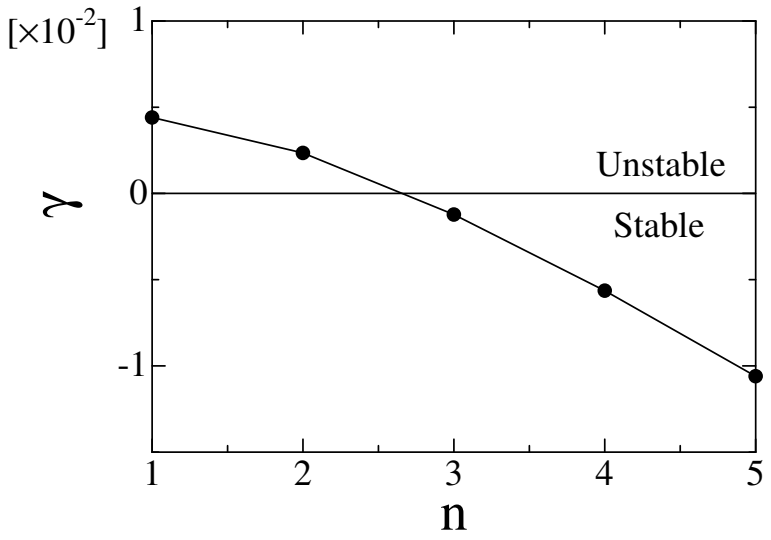

Figure 3.2: Linear growth rate γ of the interchange mode with $\Psi_b = 0$ as a function of toroidal mode number n for $S = 10^4, \nu = 8.0 \times 10^{-5}, \kappa_\perp = 10^{-5}$ and $\kappa_\parallel = 1.0$.

shown in Fig.3.3, which implies that the properties of interchange mode remain in the steady state after the nonlinear saturation. As shown in Fig.3.5(a), $\hat{\Psi}_{1,1}$ has a substantial value at the rational surface with $\iota = 1$, which corresponds to a magnetic island with a significant width. This is due to the assumption of the cylindrical geometry and the large resistivity. The sign of the mode structure changes depending on the value of σ.

In order to evaluate the width of the magnetic islands, we introduce the helical magnetic flux, which is defined as

$$\Psi_h(r, \theta, z) = \Psi_{eq}(r) - \frac{r^2}{2}\frac{n}{m} + \tilde{\Psi}(r, \theta, z). \tag{3.4}$$

Figure 3.6 shows the contour of the helical magnetic flux in the $z = 0$ cross section at $t = 10000\tau_A$ for $\Psi_b = 0$ and $\sigma = +1$. The flow pattern of the vortex calculated from $\tilde{\Phi}$ is also plotted. The $m = 1$ magnetic island is seen in Fig.3.6(a). The X-point and the O-point are located at $\theta = 0$ and $\theta = \pi$, respectively. The width evaluated from the contour is 5.3×10^{-2}. The vortices are seen in Fig.3.6 (b). The radial flow at $\theta = 0$ and $\theta = \pi$ is weak but finite. Compared with Fig.3.6 (a), the direction is radially outward at the X-point and inward at the O-point. In the case of $\sigma = -1$, an island with an opposite phase is obtained where the X-point and the O-point is located at $\theta = \pi$ and $\theta = 0$, respectively. The vortices have the flow in the opposite direction. Since the positions of the X-point and O-point are exchanged and the flow direction is reversed,

(a)

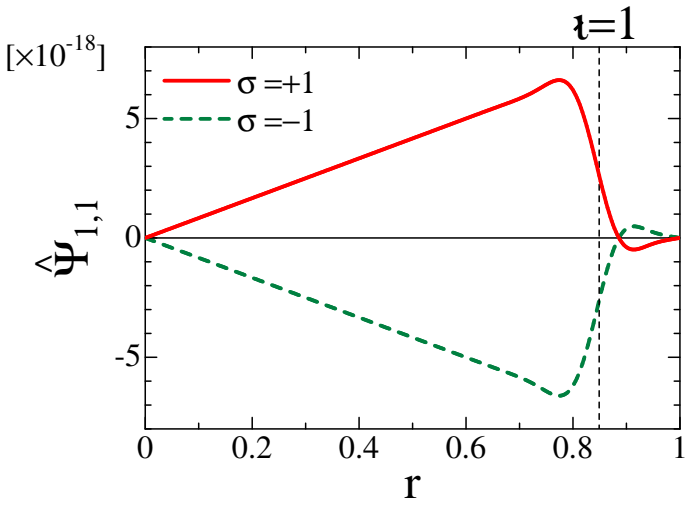

(b)

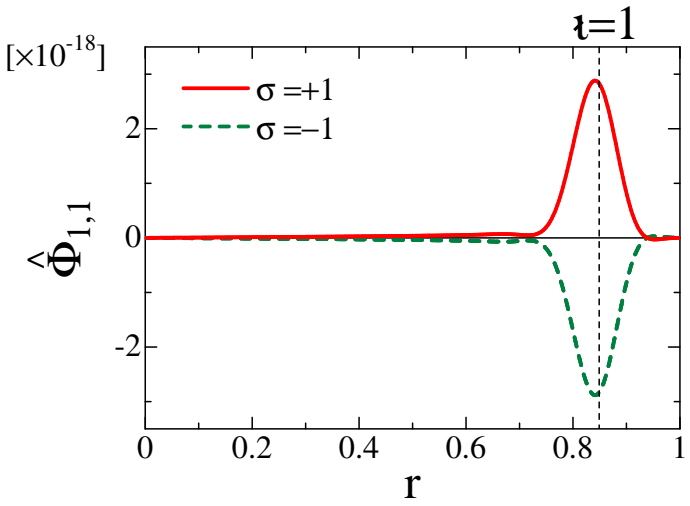

(c)

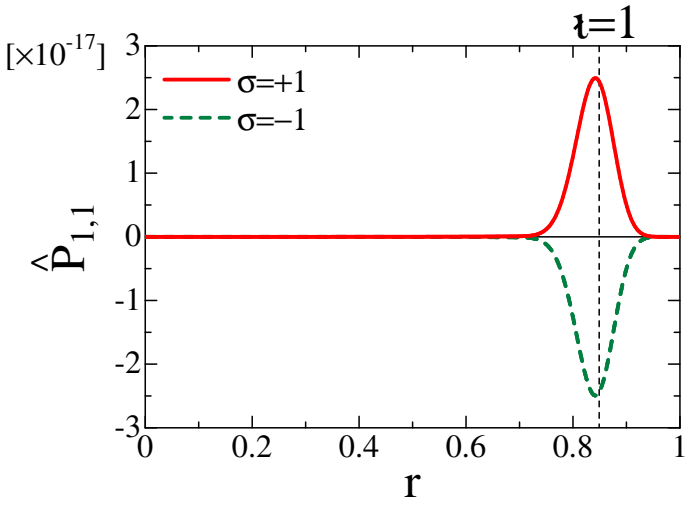

Figure 3.3: Profiles of linear eigenfunction for $(a)\hat{\Psi}_{1,1}$, $(b)\hat{\Phi}_{1,1}$ and (c) $\hat{P}_{1,1}$.

the flow direction is still radially outward in the X-point and inward in the O-point even in the change of σ.

Figure 3.7 shows the variation of the pressure profile along the line connecting the points of $(r = 1, \theta = 0, z = 0)$ and $(r = 1, \theta = \pi, z = 0)$ between $t = 0$ and $t = 10000\tau_A$ for $\Psi_b = 0$ and $\sigma = +1$. The deformation due to the interchange mode around the resonant surface with $\iota = 1$ is seen. This deformation is generated by the convection of the radial flow. The pressure is increased in the X-point at $\theta = 0$ and decreased in the O-point at $\theta = \pi$. It is also obtained that the pressure is decreased at $\theta = 0$ and increased at $\theta = \pi$ for $\sigma = -1$.

3.2.3 Interaction between static magnetic island and interchange mode

Development of interchange mode with static magnetic island

Next, we consider the nonlinear time evolution of the interchange mode under the existence of the static island with the mode number of $(m, n) = (1, 1)$. In this Chapter, the effect of the external poloidal flux $\Psi^{ext}_{1,1}$ given by Eq.(2.29) is included in $\tilde{\Psi}_{1,1}$ like Ref. [12–14]. By solving Eqs. (2.9)-(2.11) under the boundary condition,

$$\hat{\Psi}_{1,1}(r = 1) = \Psi_b, \tag{3.5}$$

we can analyze the dynamics including the effect of static island. For the analysis, the boundary condition of Eq.(3.5) has to be satisfied even in the finite beta plasma where the interchange mode develops. However, the boundary condition of Eq.(3.5) was not satisfied in the original NORM code. Therefore, the code is improved so that the boundary condition of Eq.(3.5) should be satisfied. The improvement of the NORM code is explained in Appendix A. Here, $\tilde{\Psi}_{1,1}$ coincides with $\Psi^{ext}_{1,1}$ at $t = 0$. It is noted that the force balance is satisfied even in the case of $\Psi_b \neq 0$ because $\Psi^{ext}_{1,1}$ does not induce any current density. However, the equilibrium pressure given by Eq.(3.1) is not constant along the field line in the case of $\Psi_b \neq 0$.

Here, $\Psi^{ext}_{1,1}$ generates no initial perturbation. Therefore, the initial condition of $\hat{\Psi}_{1,1}$,

$$\hat{\Psi}_{1,1} = \sigma f(r) + \Psi_b r \tag{3.6}$$

is used. We employ Eq.(2.19) as the initial perturbation except $\hat{\Psi}_{1,1}$. The value of Ψ_b varies from -2.0×10^{-3} to $+2.0 \times 10^{-3}$ in this Chapter. Figure 3.8 shows the time

(a)

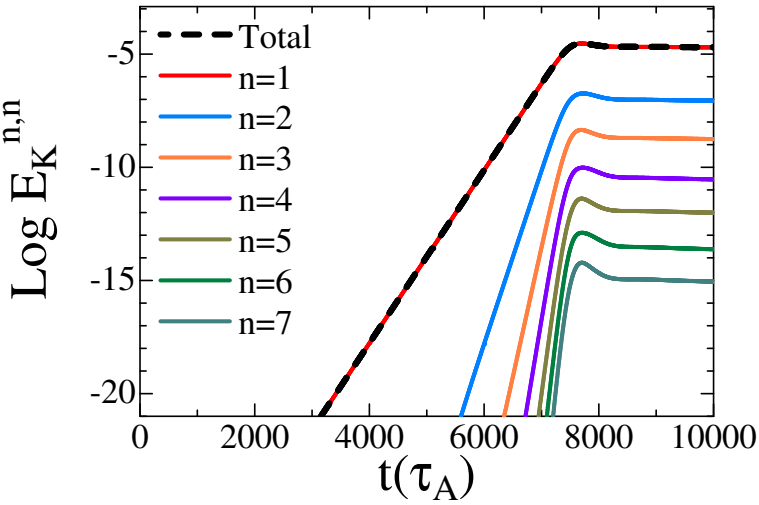

(b)

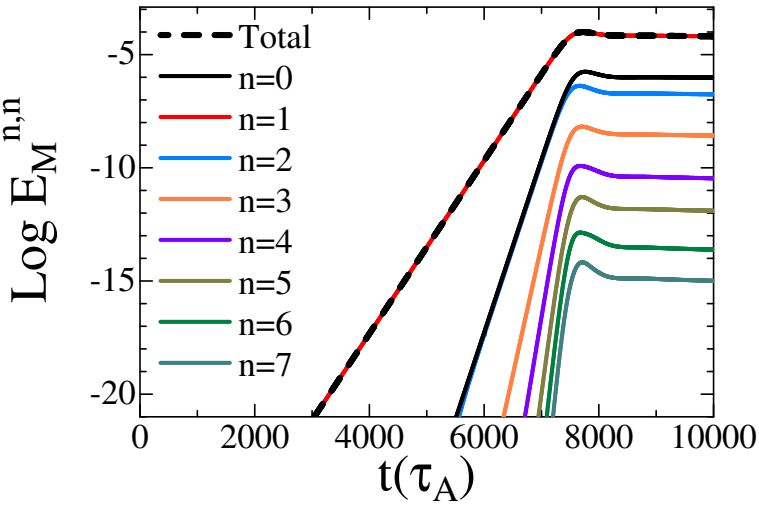

Figure 3.4: Time evolution of (a) kinetic energy and (b) magnetic energy for $\Psi_b = 0$ and $\sigma = +1$.

(a)

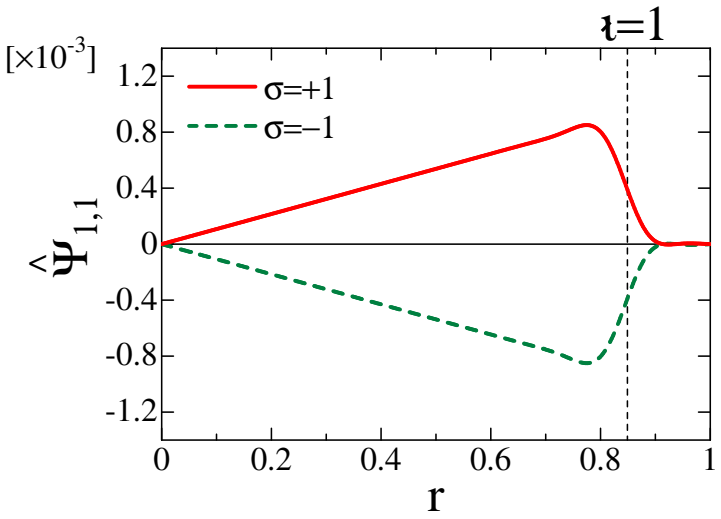

(b)

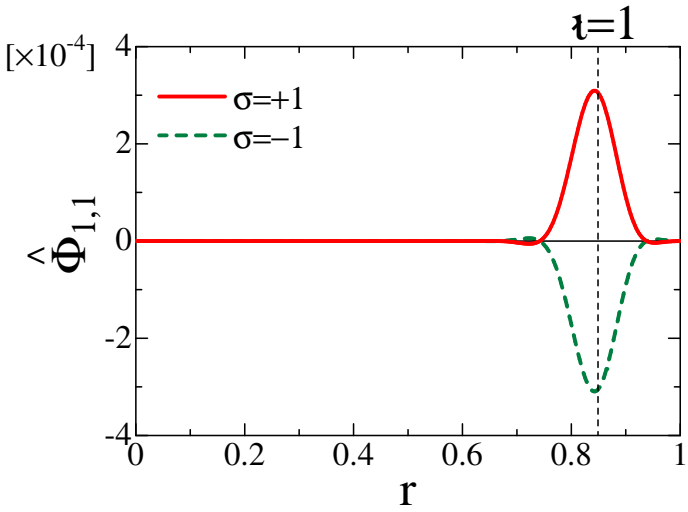

(c)

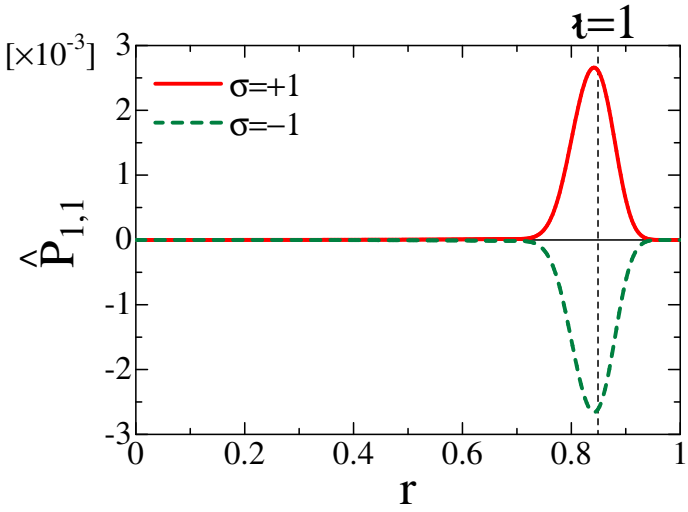

Figure 3.5: Profiles of $(a)\hat{\Psi}_{1,1}$, $(b)\hat{\Phi}_{1,1}$ and $(c)\hat{P}_{1,1}$ for $\Psi_b = 0$ at $t = 10000\tau_A$.

(a)

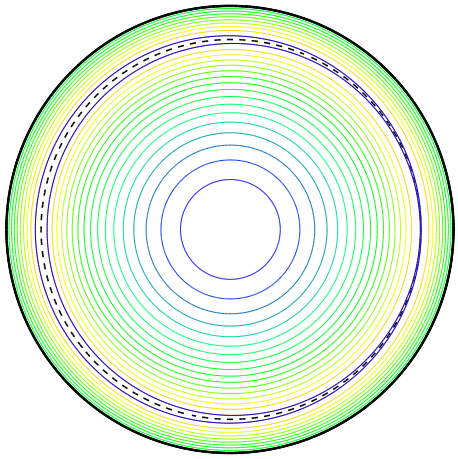

(b)

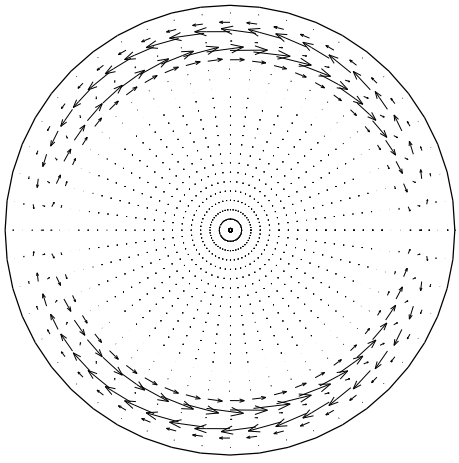

Figure 3.6: (a) Contour of helical magnetic flux and (b) flow pattern in z=0 poloidal cross section at $t = 10000\tau_A$ for $\Psi_b = 0$ and $\sigma = +1$. Dashed line shows position of the resonant surface.

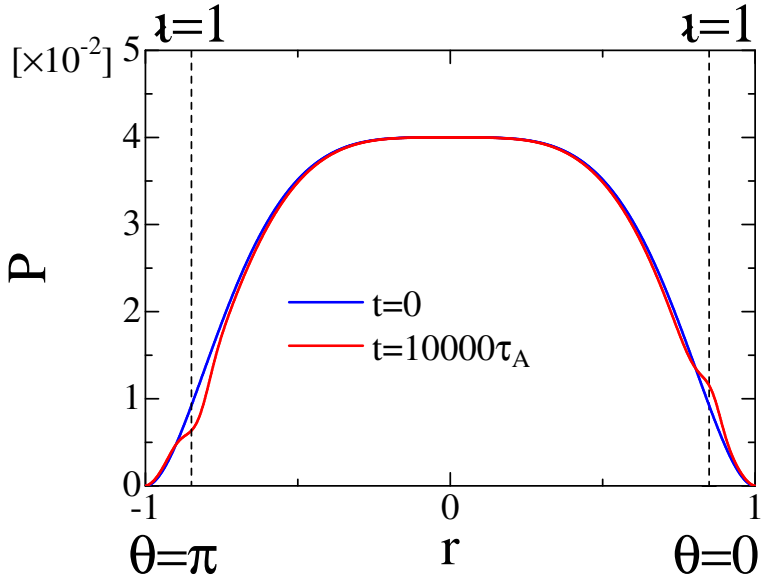

Figure 3.7: Pressure profile at $t = 0$ and $t = 10000\tau_A$ for $\Psi_b = 0$ and $\sigma = +1$ along the line connecting $(r = 1, \theta = 0, z = 0)$ and $(r = 1, \theta = \pi, z = 0)$. Radial coordinate at $\theta = \pi$ is made negative.

evolution of the kinetic energy and the magnetic energy of the interchange mode for $\Psi_b = +2.0\times10^{-3}$ and $\sigma = +1$. The $n = 1$ component is dominant in the whole region as in the case of $\Psi_b = 0$. There exists a steady state after the linear growth($t > 8000\tau_A$). Since the static island is incorporated, $E_M^{1,1}$ is large from $t = 0$. In the case of $\sigma = -1$, the time evolution of the kinetic energy and the magnetic energy are the same as those in the case of $\sigma = +1$.

There exists a difference in the linear growth rate of each component between the cases of $\Psi_b = 0$ and $\Psi_b \neq 0$. In the case of $\Psi_b = 0$, the linear growth rate of $E_K^{n,n}$ and $E_M^{n,n}$ except for $n = 0$ increases with n as shown in Fig.3.4. On the other hand, the linear growth rates of $E_K^{n,n}$ and $E_M^{n,n}$ except for $E_M^{1,1}$ in the linear region are almost the same in the case of $\Psi_b \neq 0$. The reason of this difference is explained as follows. When the component of $(m, n) = (1, 1)$ is dominant, the Ohm's law for $\tilde{\Psi}_{n,n}$ can be approximated as

$$\frac{\partial \tilde{\Psi}_{n,n}}{\partial t} \simeq -\nabla \tilde{\Psi}_{1,1} \times \nabla \tilde{\Phi}_{n-1,n-1} \cdot \mathbf{z}. \tag{3.7}$$

Assuming the time dependence of $\tilde{\Psi}_{n,n}$ and $\tilde{\Phi}_{n,n}$ in the linear region to be $e^{\gamma_n t}$ and $e^{\gamma'_n t}$, respectively, we obtain

$$\gamma_n \simeq \gamma_1 + \gamma'_{n-1}. \tag{3.8}$$

(a)

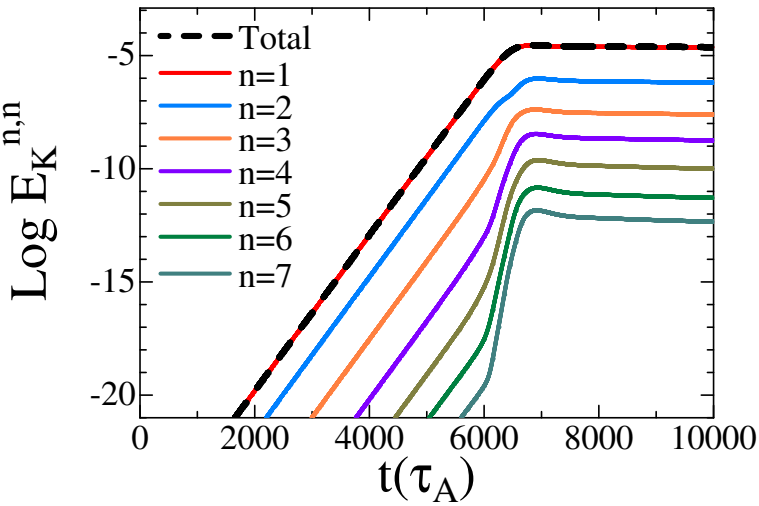

(b)

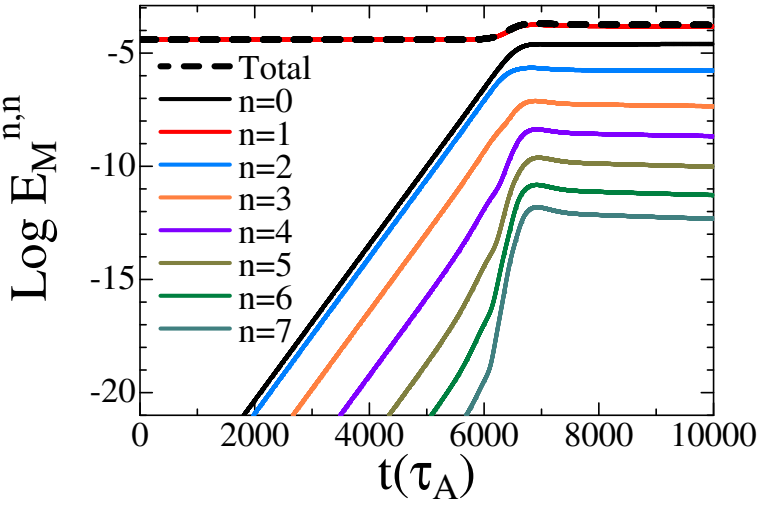

Figure 3.8: Time evolution of (a) kinetic energy and (b) magnetic energy for $\Psi_b = +2.0 \times 10^{-3}$ and $\sigma = +1$.

In the case of $\Psi_b = 0$, γ_n is given by

$$\gamma_n \simeq n\gamma_1 \tag{3.9}$$

because $\gamma_n = \gamma'_n$ for each n. On the other hand, in the case of $\Psi_b \neq 0$, $E_M^{1,1}$ is large and almost constant in the linear region. It implies $\gamma_1 \simeq 0$, and therefore, $\gamma_n \simeq \gamma'_{n-1}$ for $n \geq 2$. Since $\gamma_n \simeq \gamma'_n$ for $n \geq 2$, the relation of

$$\gamma_n \simeq \gamma'_1 \qquad (n \neq 1) \tag{3.10}$$

is obtained. Hence, $E_K^{n,n}$ and $E_M^{n,n}$ except for $E_M^{1,1}$ have almost the same growth rate. This feature of the growth rate is common for all $\Psi_b \neq 0$.

Behavior of magnetic islands in saturation of interchange mode

Behavior of the magnetic islands at the steady state after the saturation of the interchange mode is discussed. Figure 3.9 shows the dependence of the island width on Ψ_b. Positive values correspond to the islands with the X-point at $\theta = 0$ and the O-point at $\theta = \pi$. Negative values correspond to the islands with the X-point at $\theta = \pi$ and the O-point at $\theta = 0$. Here, w^h is the island width evaluated from the Ψ_h-contour. The subscript ' i ' and ' s ' denote the initial static island width at $t = 0$ and the island width after nonlinear saturation at $t = 10000\tau_A$, respectively.

The initial static island width w_i^h increases with Ψ_b as shown in Fig.3.9. On the other hand, in the cylindrical geometry, the island width with the poloidal mode number m can be evaluated by [27]

$$w_i^B = 4\hat{\Psi}_{m,n}\sqrt{\frac{1}{mr|\hat{\Psi}_{m,n}|\iota'}}\Bigg|_{r=r_s}, \tag{3.11}$$

where r_s is the radius at the resonant surface. Here, the prime denotes the derivative with respect to r. The blue line in Fig.3.9 shows w_i^B with $\hat{\Psi}_{1,1}$ given by Eq.(3.6). Good agreement between w_i^h and w_i^B is obtained, which confirms that w_i^h has the dependence of $\sqrt{\Psi_b}$.

The magnetic islands are changed by the nonlinear saturation of the interchange modes. There is a global tendency that w_s approaches w_i as $|\Psi_b|$ increases as shown in Fig.3.9. For a fixed σ, the sign of $w_s - w_i$ is independent of Ψ_b, which is the same as the sign of w_s for $\Psi_b = 0$. On the other hand, the change in the structure of the island is different depending on Ψ_b. Not only the width but also the phase of the islands can

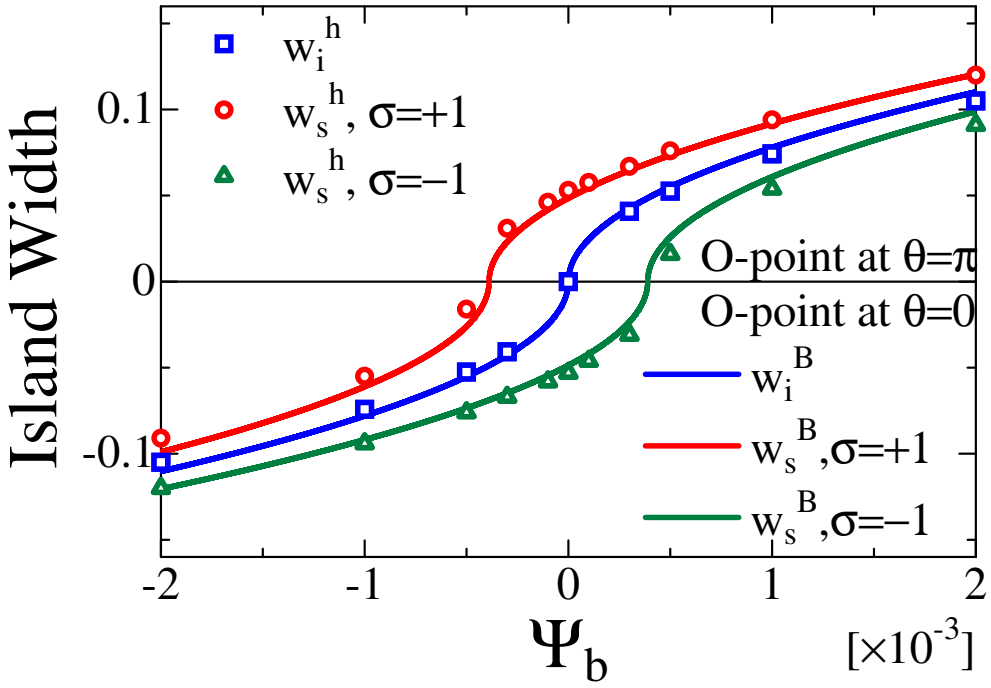

Figure 3.9: Dependence of island width on Ψ_b. Squares show the width of the initial static island. Triangles and circles show the width of the island at t=10000τ_A in the saturation region of the interchange mode. The values indicated by these marks are evaluated from the Ψ_h-contour. Solid lines are the plots of the analytic expressions given by Eq.(3.11) (blue) and Eq.(3.15) (red, green). Positive and negative values correspond to the islands with the X-point located at $\theta = 0$ and at $\theta = \pi$, respectively.

change. The change of the island structure can be classified by introducing a function,

$$C_w = \frac{|w_s| - |w_i|}{|w_s - w_i|}. \tag{3.12}$$

The values of $C_w > 0$ and $C_w < 0$ indicate the increase and the decrease of the island width, respectively. In the case of $|C_w| = 1$, the phase of the island does not change, that is, the X-point and the O-point after the saturation exist on the same positions of the static island. In the case of $|C_w| < 1$, the island phase changes and the positions of the X-point and the O-point exchange each other. Figure 3.10 shows C_w as a function of Ψ_b. In the case of $\sigma = +1$, the island width increases for $\Psi_b \gtrsim -2 \times 10^{-4}$ and decreases for other value of Ψ_b. The island phase changes for $-4 \times 10^{-4} \lesssim \Psi_b < 0$ and does not change for other value of Ψ_b.

As shown in Fig.3.9 and Fig.3.10, for a fixed value of Ψ_b, we obtain two different values of w_s depending on the value of σ. However, it is obtained that the relations of w_s, $w_s(-\sigma, -\Psi_b) = -w_s(\sigma, \Psi_b)$, $\hat{X}_{1,1}(-\sigma, -\Psi_b) = -\hat{X}_{1,1}(\sigma, \Psi_b)$ for $\hat{X}_{1,1} = (\hat{\Psi}_{1,1}, \hat{\Phi}_{1,1}, \hat{P}_{1,1})$

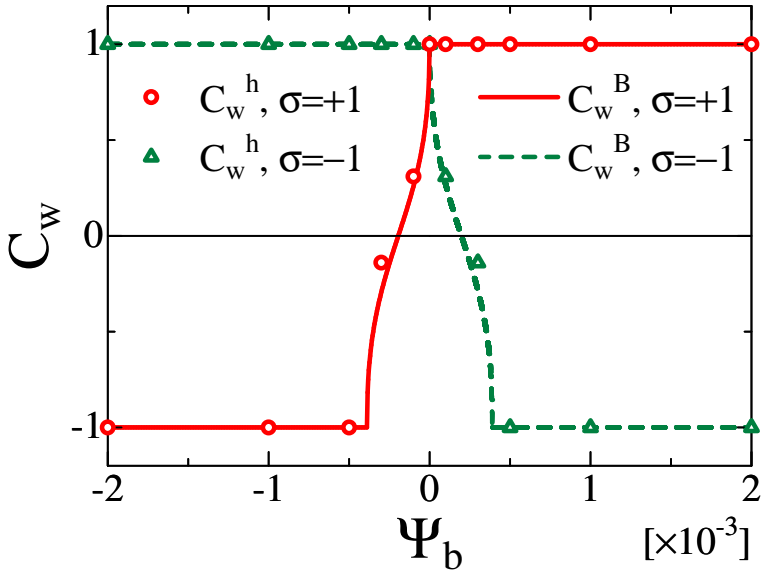

Figure 3.10: Plots of C_w given by Eq.(3.12). Triangle and circles show the values evaluated from the Ψ_h-contour. Solid lines show the value with the analytic expression of Eqs.(3.11) and (3.15) for w^B.

are valid in the accuracy with the relative error less than 0.6%. Therefore, only the case of $\sigma = +1$ is discussed in this section.

Figures 3.11, 3.12 and 3.13 show the contours of the helical flux and the flow patterns for $\Psi_b = +3.0 \times 10^{-4}, -5.0 \times 10^{-4}$ and -3.0×10^{-4}, respectively, which correspond to $C_w = +1, -1$ and -0.14. Figures 3.11 and 3.12 show the case of the increase and the decrease of the width without the change of the phase, respectively. Figure 3.13 shows the decrease of the width with the change of the phase. As shown in Figs.3.11(c), 3.12(c) and 3.13(c), the flow direction is the same independent of Ψ_b. As shown in Fig.3.14, where the profile of $\hat{\Phi}_{1,1}$ for $\Psi_b = +2.0 \times 10^{-3}$, 0 and -2.0×10^{-3} and the maximum value of $\hat{\Phi}_{1,1}$ as a function of Ψ_b are plotted, not only the direction but also the absolute value of the flow is almost constant for all Ψ_b.

Since the phase of the island changes depending on Ψ_b, the relation between the phase of island and the direction of flow varies. In the case of $\Psi_b = +3.0 \times 10^{-4}$, the flow direction is radially outward at the X-point and inward at the O-point of the initial static island as shown in Fig.3.11(a) and (c). In the case of $\Psi_b = -5.0 \times 10^{-4}$, the flow directions are radially inward at the X-point and outward at the O-point as shown in Fig.3.12(a) and (c). These results imply that if the phase of island does not change, the island width increases when the flow direction is radially outward at the X-point

(a)

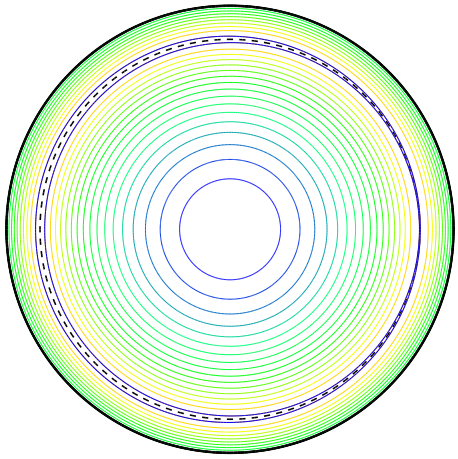

(b)

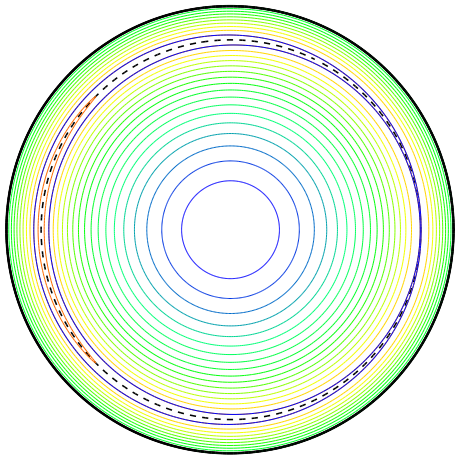

(c)

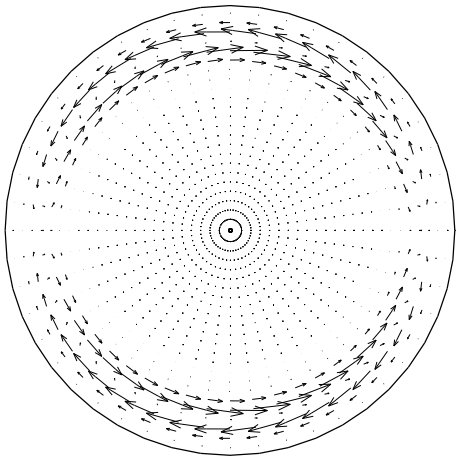

Figure 3.11: Contour of helical magnetic flux at (a) $t = 0$ and (b) $t = 10000\tau_A$ and (c) flow pattern at $t = 10000\tau_A$ for $\Psi_b = +3.0 \times 10^{-4}$ and $\sigma = +1$. Dashed lines show positions of the resonant surface.

(a)

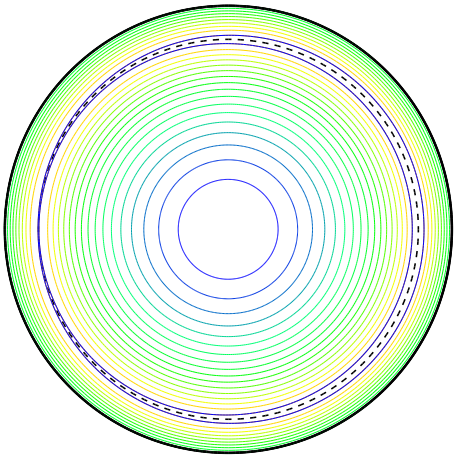

(b)

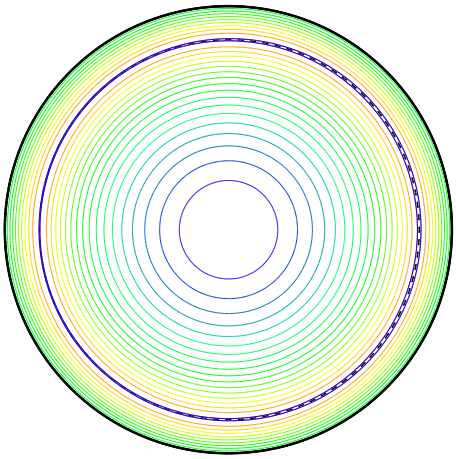

(c)

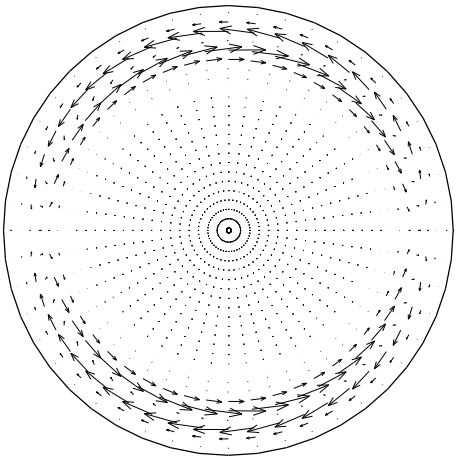

Figure 3.12: Contour of helical magnetic flux at (a) $t = 0$ and (b) $t = 10000\tau_A$ and (c) flow pattern at $t = 10000\tau_A$ for $\Psi_b = -5.0 \times 10^{-4}$ and $\sigma = +1$. Dashed lines show positions of the resonant surface.

(a)

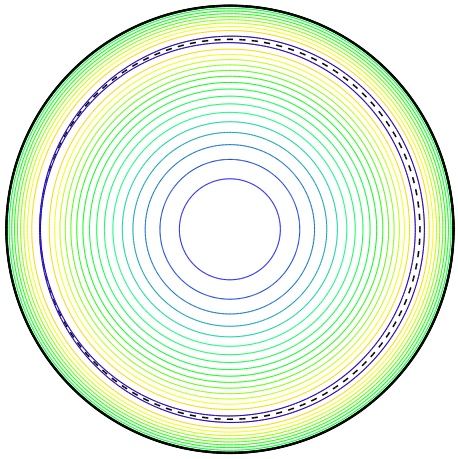

(b)

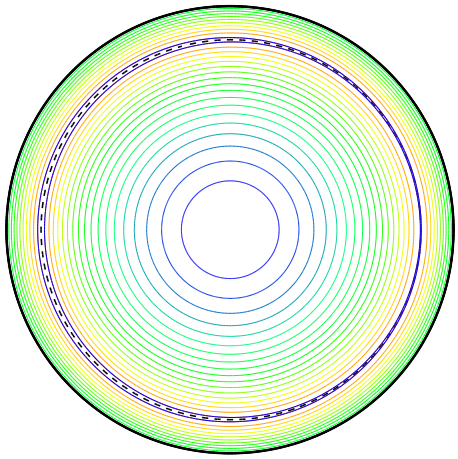

(c)

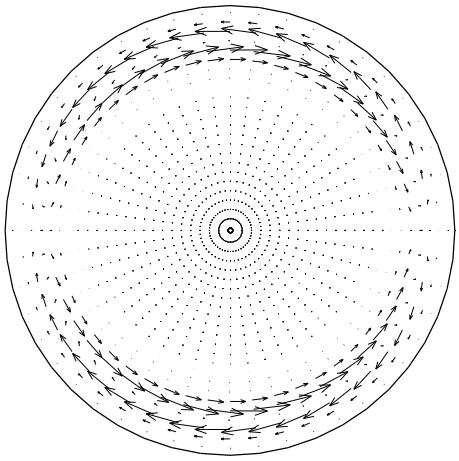

Figure 3.13: Contour of helical magnetic flux at $(a)t = 0$ and (b) $t = 10000\tau_A$ and (c) flow pattern at $t = 10000\tau_A$ for $\Psi_b = -3.0 \times 10^{-4}$ and $\sigma = +1$. Dashed lines show positions of the resonant surface.

(a)

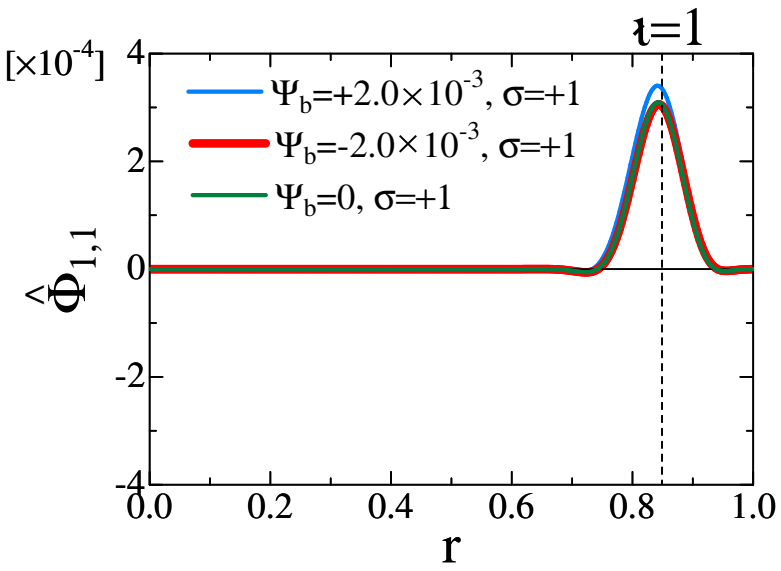

(b)

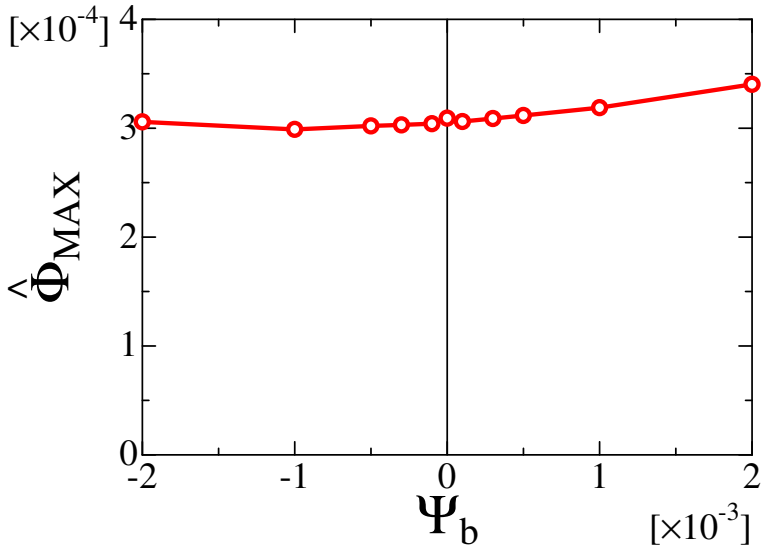

Figure 3.14: (a)Profiles of $\hat{\Phi}_{1,1}$ at $t = 10000\tau_A$ for $\Psi_b = -2.0 \times 10^{-3}, 0$ and $+2.0 \times 10^{-3}$ and $\sigma = +1$ and (b) dependence of maximum amplitude of $\Phi_{1,1}$ on Ψ_b for $\sigma = +1$.

of the initial static island, and the island width decrease when the flow direction is radially inward at the X-point. In the case of $\Psi_b = -3.0 \times 10^{-4}$, the flow direction is radially inward at the X-point and outward at the O-point of the initial static island as shown in Fig.3.13(a) and (c). This result implies that the phase of the island can change when the flow direction is radially inward at the X-point of the static islands. The phase change occurs in either case of the increase or the decrease of the width. The radially outward shift of the plasma shrinks the distance between the flux surfaces, which enhances the reconnection of the field lines. Therefore, it is considered that the radial direction of the flow is consistent with the driven reconnection of the field lines.

Mechanism of change in magnetic islands

We consider the mechanism of the change of the magnetic island due to the nonlinear interaction with the interchange modes. Since the island width is determined by the perturbed poloidal flux, we focus on the time evolution of $\hat{\Psi}_{1,1}$. Figure 3.15 shows the profiles of $\hat{\Psi}_{1,1}$ at $t = 0$ and $t = 10000\tau_A$ for $\Psi_b = +3.0 \times 10^{-4}$, -3.0×10^{-4} and -5.0×10^{-4}. Compared with Fig.3.5(a), this figure indicates that $\hat{\Psi}_{1,1}$ at $t = 10000\tau_A$ for $\Psi_b \neq 0$ is given by a superposition of $\Psi_b r$ corresponding to the initial static island and $\hat{\Psi}_{1,1}$ at $t = 10000\tau_A$ for $\Psi_b = 0$. In order to confirm it, we evaluate the contribution by the interchange mode to $\hat{\Psi}_{1,1}$ at $t = 10000\tau_A$, which is defined as

$$\hat{\Psi}^{Int}_{1,1}(\Psi_b, r) = \hat{\Psi}_{1,1}(\Psi_b, r) - \Psi_b r. \tag{3.13}$$

As shown Fig.3.16, $\hat{\Psi}^{Int}_{1,1}$ at $r = r_s$ is almost constant independent of Ψ_b. This means that $\hat{\Psi}^{Int}_{1,1}$ is hardly affected by the existence of the static islands. Therefore, we can set $\hat{\Psi}^{Int}_{1,1}(\Psi_b, r) \simeq \hat{\Psi}^{Int}_{1,1}(\Psi_b = 0, r)$ for any Ψ_b. As a result, we obtain

$$\hat{\Psi}_{1,1}(\Psi_b, r) \simeq \hat{\Psi}^{Int}_{1,1}(\Psi_b = 0, r) + \Psi_b r. \tag{3.14}$$

From this equation, we can conclude that $\hat{\Psi}_{1,1}$ for a finite Ψ_b is almost given by the *linear* sum of the poloidal fluxes of the initial static island and of the interchange mode without the static island, in spite of the fact that $\hat{\Psi}_{1,1}$ is obtained as a result of the *nonlinear* interaction of them.

By using Eq.(3.14), the island width after the nonlinear saturation of the interchange mode can be evaluated. Substituting Eq.(3.14) into Eq.(3.11), we find

$$w^B_s \simeq 4 \left. \frac{\hat{\Psi}^{Int}_{1,1}(\Psi_b = 0, r) + \Psi_b r}{\sqrt{mr\boldsymbol{\iota}'|\hat{\Psi}^{Int}_{1,1}(\Psi_b = 0, r) + \Psi_b r|}} \right|_{r=r_s}. \tag{3.15}$$

(a)

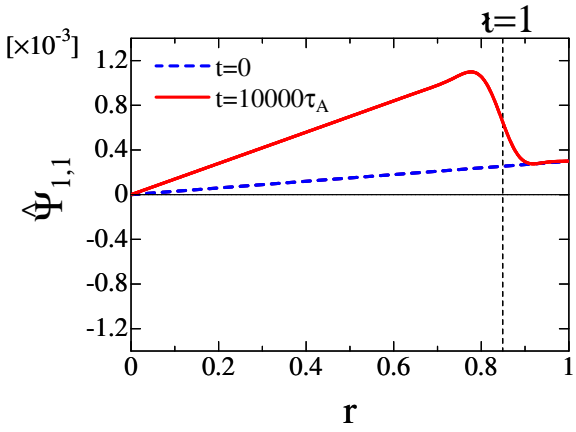

(b)

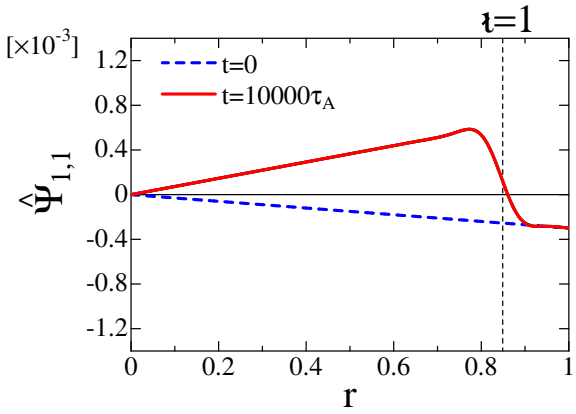

(*c*)

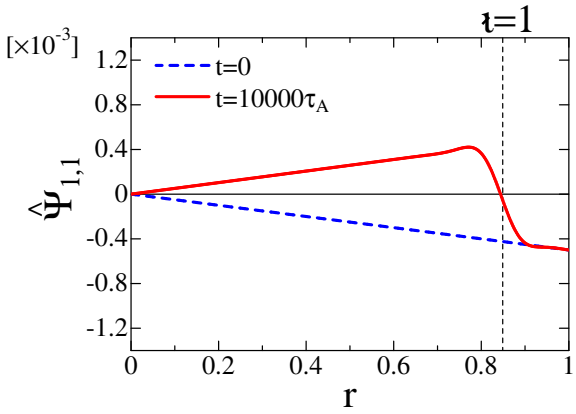

Figure 3.15: Profiles of $\hat{\Psi}_{1,1}$ at $t = 0$ and $t = 10000\tau_A$ for (a)$\Psi_b = +3.0 \times 10^{-4}$, (b) $\Psi_b = -3.0 \times 10^{-4}$ and (c) $\Psi_b = -5.0 \times 10^{-4}$ and $\sigma = +1$.

The value of C_w^B can also be evaluated by substituting Eq.(3.15) into Eq.(3.12). Good agreements between w_s^h and w_s^B and between C_w^h and C_w^B are obtained as shown in Figs.3.9 and 3.10. Furthermore, we can explain the reason why the island width after the saturation of the interchange mode approaches the initial static island width in the increase of $|\Psi_b|$. From Eq.(3.15), the difference of the widths $\Delta w = |w_s^B| - |w_i^B|$ can be written as

$$\Delta w = 4\frac{\sqrt{|\hat{\Psi}_{1,1}^{Int}(\Psi_b = 0, r_s) + \Psi_b r_s|} - \sqrt{|\Psi_b r_s|}}{\sqrt{m r_s t'}}. \tag{3.16}$$

This equation implies that Δw approaches to zero as $|\Psi_b|$ increases since $\hat{\Psi}_{1,1}^{Int}$ is constant.

The relation of the poloidal flux given by Eq.(3.14) also allows us to understand the change of the width and the phase of the islands due to the interchange mode. For $\sigma = +1$, $\hat{\Psi}_{1,1}^{Int}(\Psi_b = 0, r_s)$ is positive. In the case of $\Psi_b > 0$, $\hat{\Psi}_{1,1}^{Int}(\Psi_b = 0, r_s)$ has the same sign as $\Psi_b r_s$. Therefore, the absolute value of $\hat{\Psi}_{1,1}$ is increased from the value of $\Psi_b r_s$ after the nonlinear saturation of the interchange mode. This change of the island corresponds to the superposition of two islands with the same phase, and therefore, the island width increases with keeping the phase. On the other hand, in the case of $\Psi_b < 0$, the sign of $\hat{\Psi}_{1,1}^{Int}(\Psi_b = 0, r_s)$ is different from that of $\Psi_b r_s$. This case corresponds to the superposition of two islands with the opposite phase. In this case, the change of the island depends on the size of $|\hat{\Psi}_{1,1}^{Int}(\Psi_b = 0, r_s)|$ and $|\Psi_b r_s|$. When $|\Psi_b|$ is large enough to satisfy $|\Psi_b r_s| > |\hat{\Psi}_{1,1}^{Int}(\Psi_b = 0, r_s)|$, that is, $\Psi_b < -\hat{\Psi}_{1,1}^{Int}(\Psi_b = 0, r_s)/r_s$, the sign of $\hat{\Psi}_{1,1}$ is not changed by $\hat{\Psi}_{1,1}^{Int}$. Therefore, the island width decreases without the change of the phase. In the case of $|\Psi_b r_s| < |\hat{\Psi}_{1,1}^{Int}|$, that is, $\Psi_b > -\hat{\Psi}_{1,1}^{Int}(\Psi_b = 0, r_s)/r_s$, the phase of the island changes because the sign of $\hat{\Psi}_{1,1}$ is different from that of $\Psi_b r_s$. In this case, the island width increases for $\Psi_b > -\hat{\Psi}_{1,1}^{Int}(\Psi_b = 0, r_s)/(2r_s)$, and decreases for $\Psi_b < -\hat{\Psi}_{1,1}^{Int}(\Psi_b = 0, r_s)/(2r_s)$.

As a summary of the change for $\sigma = +1$, the width decreases without the phase change for $\Psi_b < -\hat{\Psi}_{1,1}^{Int}(\Psi_b = 0, r_s)/r_s$, the width decreases with the phase change, for $-\hat{\Psi}_{1,1}^{Int}(\Psi_b = 0, r_s)/r_s < \Psi_b < -\hat{\Psi}_{1,1}^{Int}(\Psi_b = 0, r_s)/(2r_s)$, the width increases with the phase change for $-\hat{\Psi}_{1,1}^{Int}(\Psi_b = 0, r_s)/(2r_s) < \Psi_b < 0$, and the width increases without the phase change for $\Psi_b > 0$. Above discussion can be applied to the case of $\sigma = -1$.

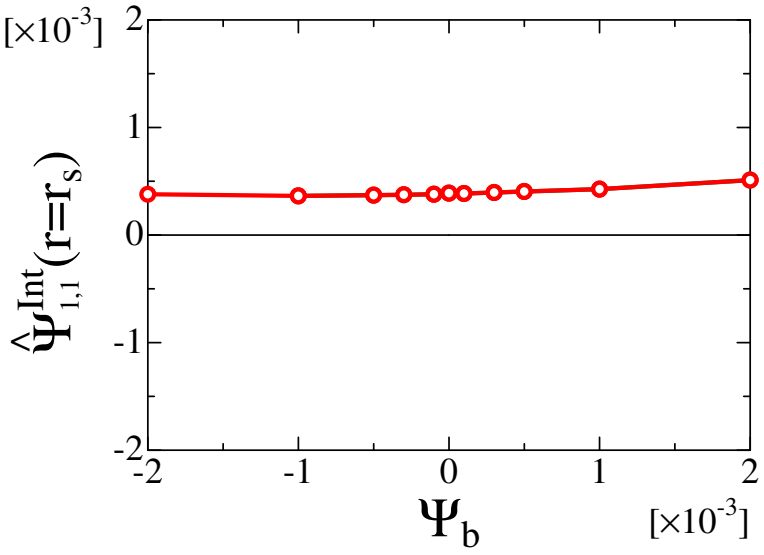

Figure 3.16: Dependence of contribution of interchange mode in total poloidal flux at $t = 10000\tau_A$ on Ψ_b.

Effect of static magnetic island on saturated pressure profile

The static islands affects the variation of the pressure profile in the nonlinear evolution of the interchange modes. Figure 3.17 shows pressure profiles at $t = 0$ and $t = 10000\tau_A$ along the line connecting the points of $(r = 1, \theta = 0, z = 0)$ and $(r = 1, \theta = \pi, z = 0)$ for $\Psi_b = +2.0 \times 10^{-3}$ and $\Psi_b = -2.0 \times 10^{-3}$ in the case of $\sigma = +1$. The X-point and the O-point are located at $\theta = 0$ and $\theta = \pi$ for $\Psi_b = +2.0 \times 10^{-3}$, respectively, and located at $\theta = \pi$ and $\theta = 0$ for $\Psi_b = -2.0 \times 10^{-3}$. The pressure profiles varies around the rational surface with $\iota = 1$ in both cases as shown in Fig.3.17. Here, we define the variation of pressure profile at the surface as

$$\Delta P(\theta_i, \Psi_b) = P(r_s, \theta_i, z = 0, \Psi_b, t = 10000\tau_A) - P(r_s, \theta_i, z = 0, \Psi_b, t = 0), \qquad (3.17)$$

where θ_i takes the value of zero or π. Both cases in Fig.3.17 show $\Delta P(\theta_i = 0, \Psi_b) > 0$ and $\Delta P(\theta_i = \pi, \Psi_b) < 0$ as in the case of $\Psi_b = 0$ shown in Fig.3.7. Therefore, each position of the increase or the decrease of the pressure does not depend on the phase of the island. This is due to the fact that the flow direction the vortices is independent of Ψ_b as shown in Fig.3.14 and the convection due to the flow brings the pressure variation. However, the absolute value of ΔP is different depending on the sign of Ψ_b even at the same θ_i. This difference is attributed to the topology of the initial static island at $\theta = \theta_i$, X-point or O-point. In order to clarify the effect of the topology of the static island on the pressure variation, we compare the two pressure profiles for

(a)

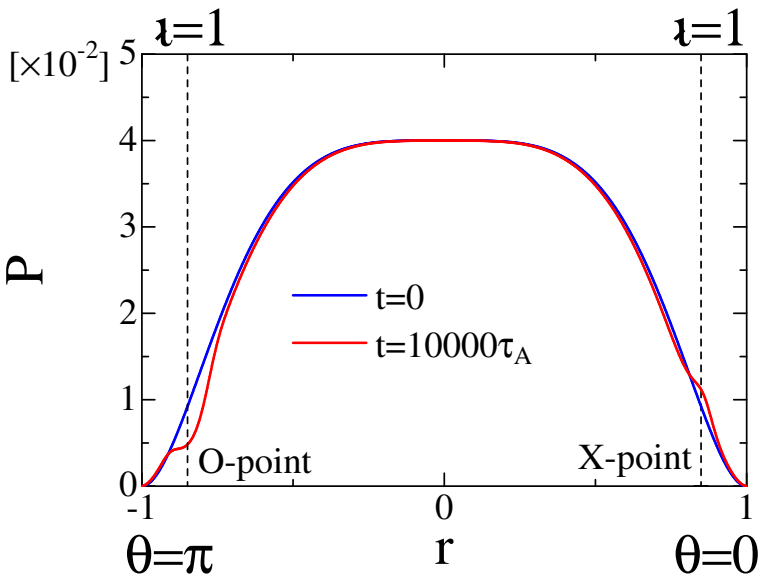

(b)

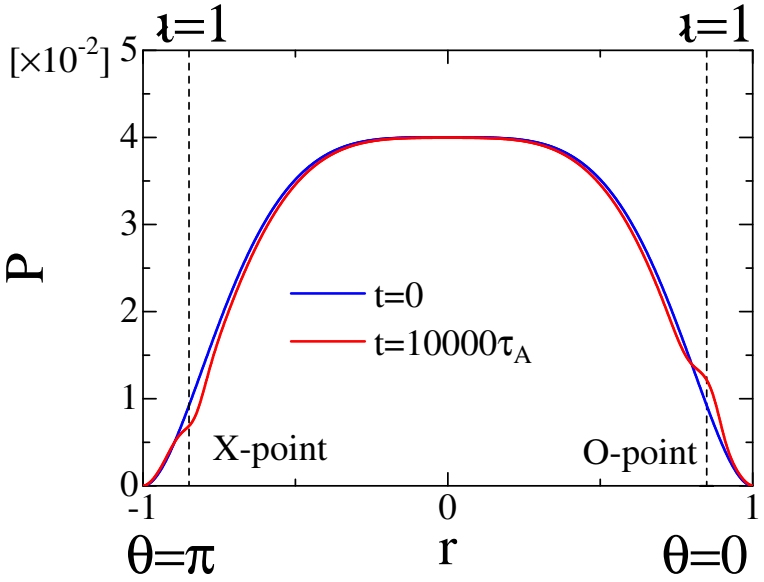

Figure 3.17: Pressure profile at $t = 0$ and $t = 10000\tau_A$ along the line between $(r = 1, \theta = 0, z = 0)$ and $(r = 1, \theta = \pi, z = 0)$ for (a)$\Psi_b = +2.0 \times 10^{-3}$ and $\sigma = +1$ and (b) $\Psi_b = -2.0 \times 10^{-3}$ and $\sigma = +1$. Radial coordinate at $\theta = \pi$ is made negative.

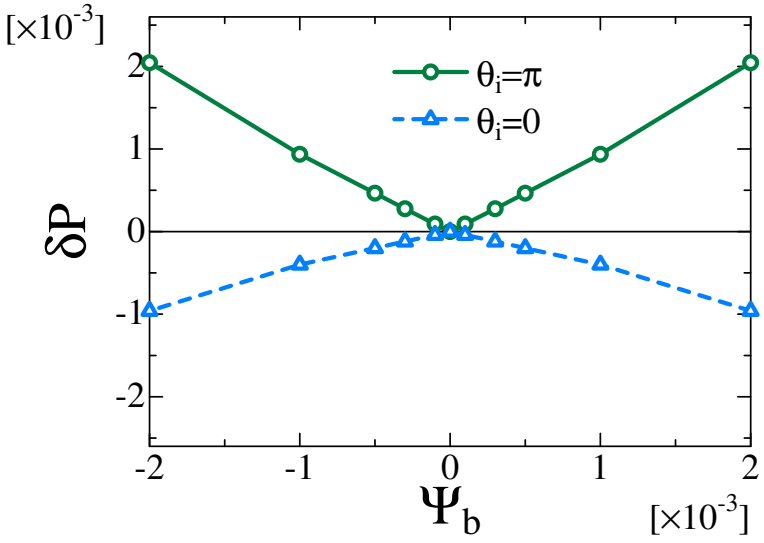

Figure 3.18: Difference of pressure variation between at X-point and at O-point given by Eq. (3.18).

$|\Psi_b|$ and $-|\Psi_b|$. In this case, the topology of the initial static island at $\theta = \theta_i$ is always different, that is, one is the X-point and the other is the O-Point as in the case of Fig.3.17. By utilizing $\delta P(\theta_i, \Psi_b)$ defined as

$$\delta P(\theta_i, \Psi_b) = |\Delta P(\theta_i, |\Psi_b|)| - |\Delta P(\theta_i, -|\Psi_b|)|, \tag{3.18}$$

we can examine the difference of the pressure variation between at the X-point and at the O-point. In the case of $\theta_i = 0$, the first and second terms of the right hand side in Eq.(3.18) show the pressure variations at the X-point and the O-point of the initial static islands, respectively. Therefore, $\delta P(\theta_i = 0, \Psi_b)$ means the subtraction of the pressure variation at the X-point from that at the O-point. Similarly, $\delta P(\theta_i = \pi, \Psi_b)$ is the subtraction of the pressure variation at the O-point from that at the X-point. As shown in Fig.3.18, $\delta P(\theta_i = 0, \Psi_b) \leq 0$, $\delta P(\theta_i = \pi, \Psi_b) \geq 0$ for any Ψ_b. Hence, the pressure variation at the O-point of the initial static island is larger than that at the X-point, whichever the pressure increases or the decreases.

3.2.4 Discussion

In this section, we discuss the reason why there exist two independent solutions of the saturated islands for each value of Ψ_b as shown in Fig.3.9 and the reason why the poloidal flux in the saturation is almost given by the linear sum of the poloidal fluxes of the initial static island and the interchange mode without the static island.

At first, we discuss the reason for the existence of two solutions for each value of Ψ_b. This result is attributed to the fact that the parallel heat conductivity of equilibrium pressure is not included in Eq.(2.11). In this case, imposing the static islands dose not excite any interchange modes, because the static island generates no current as shown in Eq.(2.25). If we put $\sigma = 0$ in the initial condition given by Eq.(3.6) for $\hat{\Psi}_{1,1}$ and Eq.(2.19) for other perturbations, nothing grows even in the case of a finite Ψ_b in principle, although an unphysical current corresponding to the static island due to truncation errors can excite the interchange mode in actual numerical calculations. On the other hand, the interchange mode with $\Psi_b = 0$ has two solutions for finite initial perturbations or $\sigma = \pm 1$. The solutions of the poloidal flux have different signs depending on the choice of σ as shown in Fig.5. The solutions are physically identical, however, the finite Ψ_b affects each solution in a different way. That is, it increases or decreases $\hat{\Psi}_{1,1}$ if Ψ_b has a sign the same as or opposite to the sign of $\hat{\Psi}_{1,1}$ obtained with $\Psi_b = 0$, respectively. As a result, two different solutions exist for each Ψ_b. Note that the amplitude of $f(r)$ in Eqs.(2.19) and (3.6) is chosen to be large enough so that the effect of the truncation error should be negligible in the calculations for Fig.3.9. If the parallel heat conductivity of the equilibrium pressure exists, the finite Ψ_b can induce an initial perturbation with a definite sign and an amplitude larger than that of the truncation error even in the case of $\sigma = 0$. Therefore, a single solution is obtained corresponding to the initial perturbation for each Ψ_b in this case.

Next we consider the reason for the linear relation given by Eq.(3.14). The reason is attributed to the following factors : the $(m, n) = (1, 1)$ component is dominant compared with other components, the parallel heat conductivity of P_{eq} is not included as mentioned above, and Ψ_b is small. By integrating the Ohm's law given by Eq.(2.9) formally, we obtain the solution for $\tilde{\Psi}_{1,1}$ given by

$$\tilde{\Psi}_{1,1} = \Psi_b r \cos(\theta - z) + \int_0^t dt \left\{ -\mathbf{B}_{eq} \cdot \nabla \tilde{\Phi}_{1,1} - (\tilde{\mathbf{B}} \cdot \nabla \tilde{\Phi})_{1,1} + \frac{1}{S} \tilde{J}_{z1,1} \right\}. \qquad (3.19)$$

The first term is the initial condition which is kept during the time evolution owing to the boundary condition Eq.(2.27). The second integral term corresponds to $\hat{\Psi}^{Int}_{1,1}$ in Eq.(3.13). The integrand becomes zero at the saturation of the interchange mode. In the integrand, the dominant terms are the first and the third terms because the $(m, n) = (1, 1)$ components are dominant in the perturbations. Therefore, the solution of $\tilde{\Psi}_{1,1}$ at the saturation is almost determined when these terms are balanced including $\tilde{\Phi}_{1,1}$. On the other hand, the saturation of the interchange mode occurs when the gradient of average pressure given by $P_{eq} + \tilde{P}_{0,0}$ is reduced sufficiently and a local

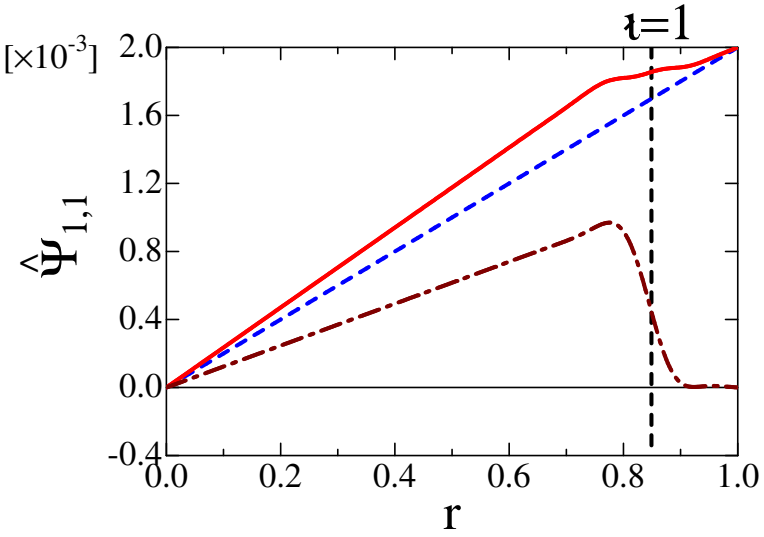

Figure 3.19: Profiles of $\hat{\Psi}_{1,1}$ for $\Psi_b = 2.0 \times 10^{-3}$ at $t = 0$ (dashed line) and saturation phase (solid line) and for $\Psi_b = 0$ (dashed and dotted line) in the case of $S = 10^4$, $\nu = 6.4 \times 10^{-5}$, $\kappa_\perp = 0.8 \times 10^{-5}$ and $\kappa_\parallel = 0.8$.

flat region is generated in the average pressure profile around the resonant surface. The effect of the static island on the generation of the flat region is weak because only the parallel heat conductivity of the perturbed pressure is included and not the equilibrium pressure. The value of $\tilde{\Phi}_{1,1}$ at the saturation is determined mainly by the average pressure with the flat region in the vorticity equation of Eq.(2.10). Therefore, the $\tilde{\Phi}_{1,1}$ is almost independent of Ψ_b. This situation is confirmed with the results in Fig.3.14. Hence, the integrand of Eq.(3.19) is also almost independent of Ψ_b, and therefore, the integrand with finite Ψ_b is approximated by that with $\Psi_b = 0$, as shown in Fig.3.16. It follows that the value of $\hat{\Psi}_{1,1}$ at the saturation is mainly given by the sum of $\Psi_b r$ and $\hat{\Psi}^{Int}_{1,1}$ with $\Psi_b = 0$.

On the contrary, when the parallel heat conductivity of P_{eq} is included, the profile of the average pressure profile at saturation can be changed depending on Ψ_b. Then, there is a possibility that the integrand also depends on Ψ_b through the change of $\tilde{\Phi}_{1,1}$. Besides, the integrand can depend on Ψ_b if the contribution of the second nonlinear term of the integrand becomes significant, even when the parallel heat conductivity of P_{eq} is not included. In the second nonlinear term, Ψ_b is included in the form of $\nabla[\Psi_b r \cos(\theta - z)] \times \nabla\tilde{\Phi}_{2,2} \cdot \mathbf{z}$. Therefore, when both Ψ_b and $\tilde{\Phi}_{2.2}$ are large enough, this term affects the linear relation of the poloidal fluxes. We obtain one of the examples of such case, which is shown in Fig.3.19. In this case, we employ the dissipation

parameters as $S = 10^4$, $\nu = 6.4 \times 10^{-5}$, $\kappa_\perp = 0.8 \times 10^{-5}$ and $\kappa_\parallel = 0.8$ instead of Eq.(3.3). In the time evolution, the growth rate of the $(m, n) = (2, 2)$ component is slightly larger than that of the $(m, n) = (1, 1)$ component in the linear phase, while the $(m, n) = (1, 1)$ component is dominant in the magnetic energy in the saturation phase. As shown in Fig.3.19, the sum of $\hat{\Psi}^{Int}_{1,1}(\Psi_b = 0)$ and $\Psi_b r$ is much larger than $\hat{\Psi}_{1,1}(\Psi_b = 2.0 \times 10^{-3})$ at the resonant surface. We also obtain that the linear sum is still a good approximation in the case of a smaller Ψ_b ($\Psi_b = 1.0 \times 10^{-4}$) for the above dissipation parameters. Since we focus on the interaction between the $(m, n) = (1, 1)$ static island and the interchange mode of which the dominant component has the same mode number in the present work, systematic analysis of the cases where the $(m, n) = (2, 2)$ component has the largest linear growth rate is out of our scope.

3.3 Effect of parallel diffusion of equilibrium pressure on island behavior

3.3.1 Island evolution due to interchange mode

In the previous Section, two solutions are obtained for a given error field depending on the sign of initial perturbations in the nonlinear saturation phase of the interchange mode. One corresponds to the increase in the island width and the other the decrease. In the previous Section, effect of the diffusion parallel to the magnetic field is included only for the perturbed pressure. As the next step to consider more realistic situation, we include the effect of the parallel diffusion for the equilibrium pressure in this Section. In this case, the term of the parallel diffusion of the equilibrium pressure in the plasma pressure equation automatically generates an initial perturbation. Therefore, the solution can be uniquely determined, which corresponds to the increase or the decrease of the island width. The plasma pressure equation including the parallel diffusion of the equilibrium pressure instead of Eq.(2.11), which is given by

$$\frac{d\tilde{P}}{dt} = (\hat{z} \times \nabla\tilde{\Phi}) \cdot \nabla P_{eq} + \kappa_\perp \nabla^2_\perp \tilde{P} + \kappa_\parallel (\mathbf{B} \cdot \nabla)(\mathbf{B} \cdot \nabla)(P_{eq} + \tilde{P}). \tag{3.20}$$

Here, the term of equilibrium pressure,

$$Q = \kappa_\parallel (\mathbf{B} \cdot \nabla)(\mathbf{B} \cdot \nabla) P_{eq}, \tag{3.21}$$

is involved. Equations (2.9) and (2.10) are employed as the Ohm's law and the vorticity equation, respectively.

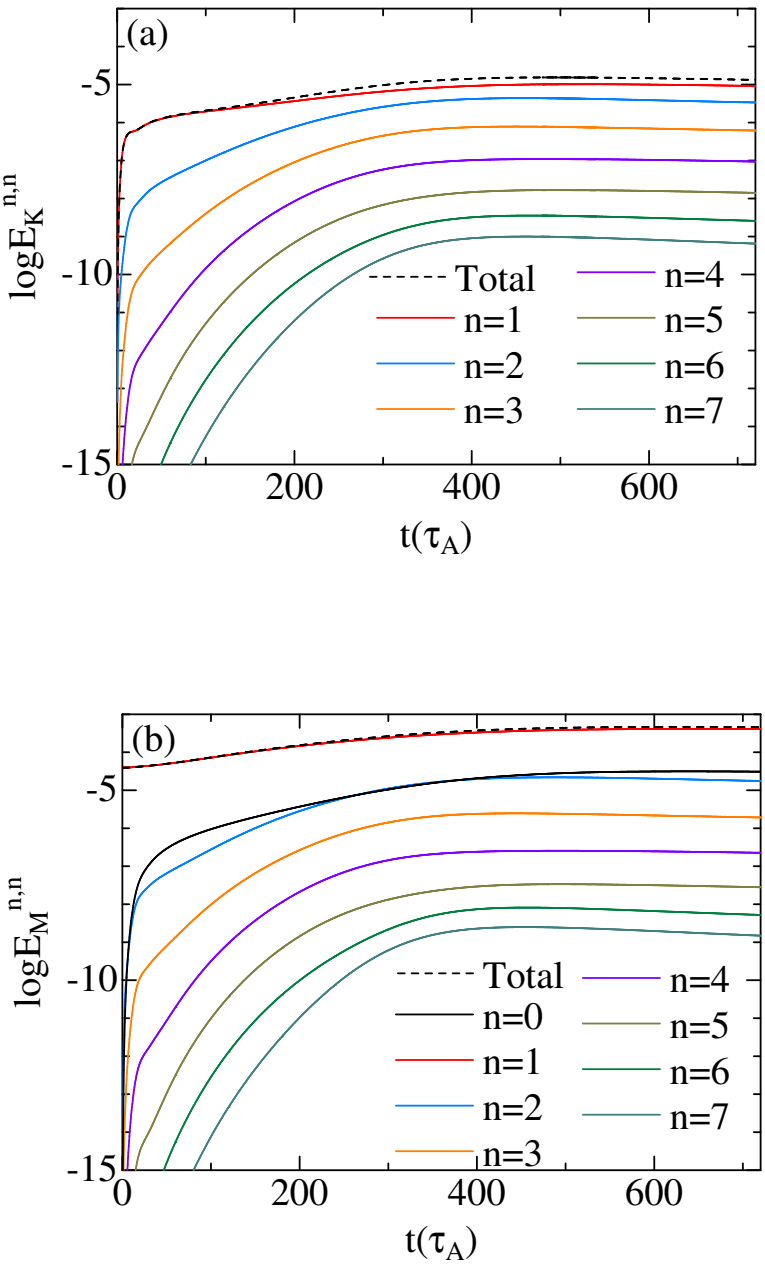

Figure 3.20: Time evolution of (a) kinetic energy and (b) magnetic energy for $\Psi_b = 2.0 \times 10^{-3}$.

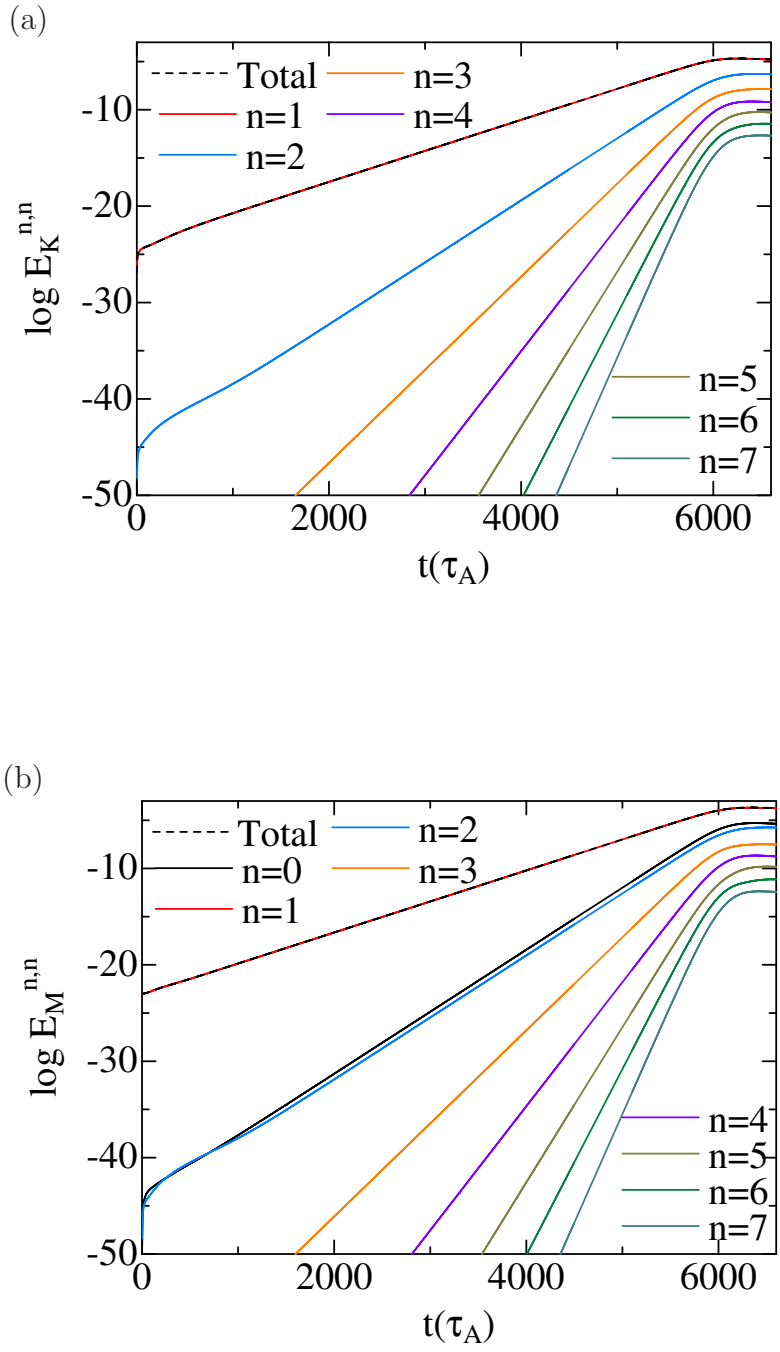

Figure 3.21: Time evolution of (a) kinetic energy and (b) magnetic energy for $\Psi_b = 1.0 \times 10^{-12}$.

(a)

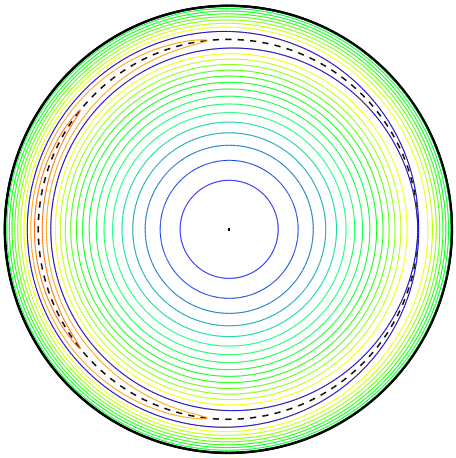

(b)

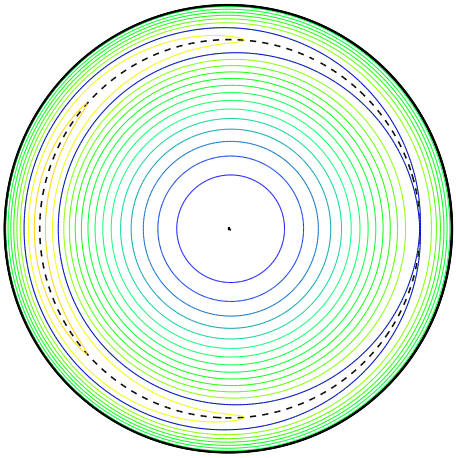

Figure 3.22: Contour of helical magnetic flux on $z = 0$ poloidal cross section for $\Psi_b = 2.0 \times 10^{-3}$ at (a) $t = 0$ and (b) $t = 720\tau_A$.

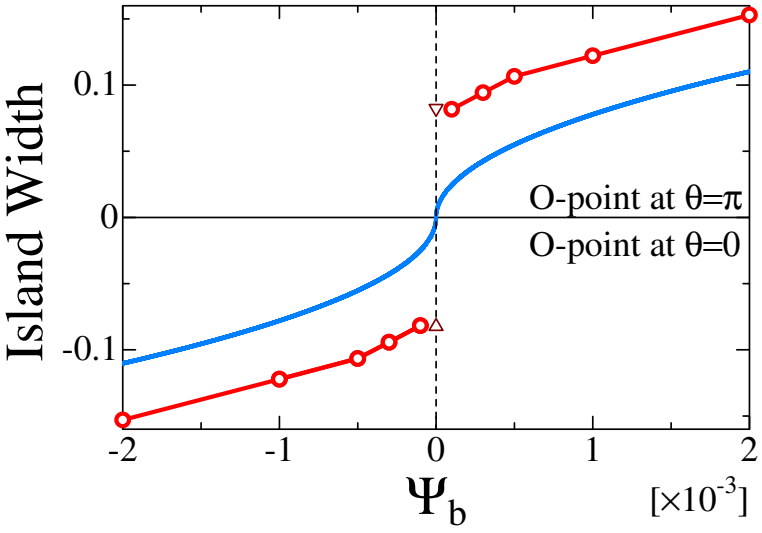

Figure 3.23: Dependence of island width on Ψ_b. Blue line shows the width at $t = 0$ evaluated with the analytic expression (3.11). Triangle and circles show the width in the saturation of interchange mode for $\Psi_b = 0$ and finite values of Ψ_b, respectively.

We follow the nonlinear evolution of the interchange mode with the static island by introducing finite Ψ_b. In this case, at the first time step of $t = \Delta t$, the parallel diffusion of the equilibrium pressure Q generates an initial perturbation of pressure P

$$P_b = Q\Delta t|_{t=0} = -\kappa_{\parallel}(1-\epsilon)\Psi_b \frac{dP_{eq}}{dr}\Delta t. \tag{3.22}$$

Therefore, any explicit external initial perturbation is not given.

Figure 3.20 shows the time evolution of the kinetic energy and the magnetic energy of the interchange mode for $\Psi_b = 2.0 \times 10^{-3}$. The dissipation parameters of

$$S = 10^4, \nu = 1.5 \times 10^{-4}, \kappa_{\perp} = 10^{-5}, \kappa_{\parallel} = 1.0 \tag{3.23}$$

are employed so that the $n = 1$ component is dominant. A steady state is obtained after the nonlinear saturation of the interchange mode. Linearly growing phase does not appear for $\Psi_b = 2.0 \times 10^{-3}$, not like the case without a static island. This difference is due to the fact that the inhomogeneous term Q is added continuously in Eq.(3.20). As shown in Eq.(3.21), the absolute value of $|Q|$ is decreased as $|\Psi_b|$. It is obtained that the linearly growing phase becomes seen explicitly as $|\Psi_b|$ is decreased as shown in Fig. 3.21.

In order to observe the change in the island due to the nonlinear saturation of the interchange mode, we plot the contour of the magnetic helical flux Ψ_h. Figure 3.22 shows the flux surfaces at $t = 0$ before the growth of the interchange mode and

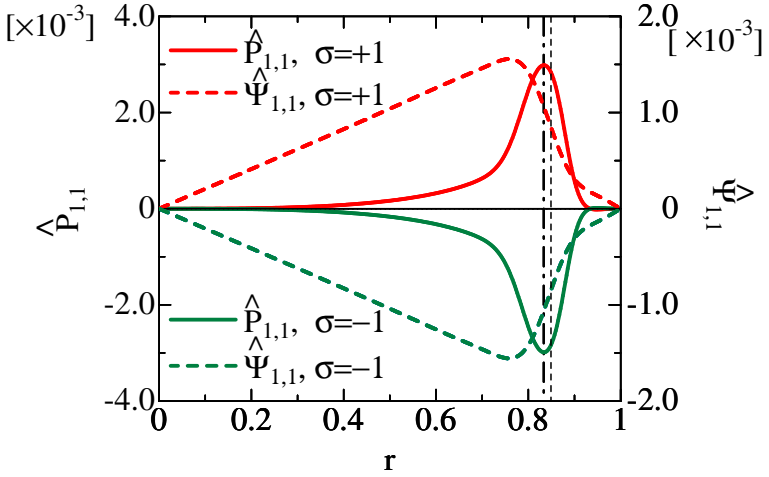

Figure 3.24: Profiles of $\hat{P}_{1,1}$ and $\hat{\Psi}_{1,1}$ for $\Psi_b = 0$ in the saturation phase of interchange mode. Dashed and chain lines indicate the positions of $r = r_s$ and $r = r_m$, respectively.

$t = 720\tau_A$ after the nonlinear saturation of the mode. The island width is 0.105 at $t = 0$ and 0.153 at $t = 720\tau_A$. Figure 3.23 shows the dependence of the island width on Ψ_b. The sign of the island width means the island phase as Fig.3.9. The blue line shows the island width at $t = 0$, which is obtained by the analytical expression Eq.(3.11). The agreement between w_B and the island width evaluated by Ψ_h contour is already confirmed in Fig.3.9. The red circles show the island width after the saturation of interchange mode for each Ψ_b. For finite Ψ_b, the island width after the saturation is always larger than that at $t = 0$. That is, the island width increases due to the nonlinear evolution of the interchange mode. The phase of the island is not changed by the mode. This property is independent of the sign of Ψ_b.

The island width after the nonlinear saturation increases as $|\Psi_b|$. However, the increment of the island width due to the interchange mode is almost independent of $|\Psi_b|$. This is attributed to the fact that the increase of the island width after the saturation is mainly brought by that of the static island width.

3.3.2 Mechanism of increase in island width

Here we discuss the reason why the island width increases due to the interchange mode in the case with the parallel diffusion of equilibrium pressure. For this purpose, we consider the property of the mode structures of the interchange mode by utilizing the case $\Psi_b = 0$ at first. In this case, P_b given by Eq.(3.22) is zero. Therefore, in the case without external initial perturbations, nothing happens. Thus, we employ a pressure

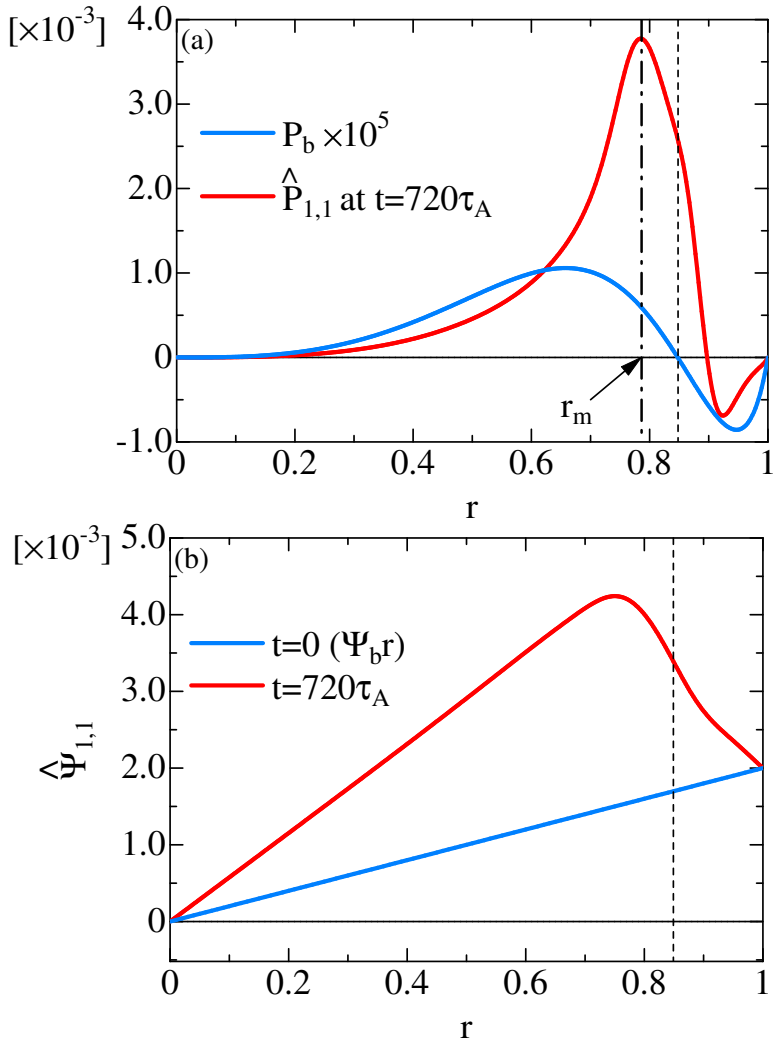

Figure 3.25: Profiles of $(a) P_b \times 10^5$ and $\hat{P}_{1,1}$ at $t = 720\tau_A$ and (b) $\hat{\Psi}_{1,1}$ at $t = 0$ and $t = 720\tau_A$. Dashed and chain lines indicate the position of $r = r_s$, and $r = r_m$, respectively.

perturbation given by

$$P_{ini} = \sigma f(r) \tag{3.24}$$

as the initial perturbation for the calculation. Here, $\sigma f(r)$ is given by Eq.(2.19). In this case, there exist two solutions with the same absolute value and different sign depending on the value of σ as shown in Figs. 3.23 and 3.24.

Equation (3.24) and Fig.3.24 show that the sign of the initial and the saturation values of $\hat{P}_{1,1}(r_m)$ is positive for $\sigma = +1$ and negative for $\sigma = -1$, where r_m denotes the position where the saturated $\hat{P}_{1,1}$ has the maximum absolute value. That is, the sign of the saturated $\hat{P}_{1,1}(r_m)$ is determined by that of P_{ini}. This is because the function of

P_{ini} involves a component which grows to the saturated $\hat{P}_{1,1}$, and therefore, the sign of the component is succeeded to the saturated $\hat{P}_{1,1}$. Figure 3.24 also shows that the signs of $\hat{\Psi}_{1,1}(r_s)$ and $\hat{P}_{1,1}(r_m)$ are the same in the saturation of the interchange mode in either case of σ. Note that $r_m < r_s$.

We utilize this property of the interchange mode in the consideration for the case of finite Ψ_b. In this case, P_{ini} is given by P_b instead of Eq.(3.24). Figure 3.25 (a) shows the profile of P_b and the saturated $\hat{P}_{1,1}$ for $\Psi_b = 2.0 \times 10^{-3}$. The profile of P_b has a positive value for $r < r_s$. Therefore, $\hat{P}_{1,1}$ grows so as to be positive at $r = r_m$. Figure 3.25 (b) shows the initial and the saturated profiles of $\hat{\Psi}_{1,1}$. At $t = 0$, $\hat{\Psi}_{1,1}$ already has a positive value at $r = r_s$ because $\hat{\Psi}_{1,1}$ is given by $\Psi_b r_s$ with positive Ψ_b. The change of $\hat{\Psi}_{1,1}(r_s)$ due to the interchange mode is also positive because $\hat{P}_{1,1}(r_m) > 0$. As a result, the absolute value of $\hat{\Psi}_{1,1}(r_s)$ increases as the mode grows. This means that the island width is increased because the width is proportional to the square root of $|\hat{\Psi}_{1,1}(r_s)|$. The same result is obtained also in the negative Ψ_b case.

3.4 Summary

The effect of the resistive interchange mode with the mode number of (m, n)=(1,1) on the static magnetic island with the same mode number generated by an externally imposed poloidal flux and in a straight heliotron plasma is studied numerically. The single helicity perturbations are employed and the poloidal uniform flow is not included. A high resistivity is assumed for the enhancement of the effect of the interchange mode. The viscosity and the heat conductivity are chosen so that the (m, n)=(1,1) component of the interchange mode is dominant in the nonlinear calculation. All physical quantities are evaluated at the steady state after the saturation of interchange mode.

Since we employ high resistivity ($S = 10^4$), a significant island is generated in the nonlinear saturation of the interchange mode even without the static island. In the case with the static island, the interchange mode grows and saturates nonlinearly as in the case without the static island. The width of the magnetic island is changed by the nonlinear saturation of the interchange mode. The situation of the increase or decrease of the width depends on whether the diffusion of the equilibrium pressure in the direction parallel to the magnetic field is taken into account or not.

In the case without the effect of the diffusion of the equilibrium pressure, there exist two solutions increasing and decreasing the island width for a given external poloidal

flux. Such changes of the island are determined by the total perturbed poloidal flux in the saturation state. In spite of the nonlinear interaction, the total poloidal flux is given by the linear sum of the poloidal flux generated by the interchange mode without a static island and the external poloidal flux for the generation of the static island. The poloidal flux generated by the interchange mode is almost constant for the variation of the external poloidal flux. Therefore, the changes of the width and the phase of the island depend on the value of the external poloidal flux. As the absolute value of the external poloidal flux increases, the contribution of the poloidal flux generated by the interchange mode becomes relatively small. Since the island width is proportional to the square root of the total perturbed poloidal flux, the island width after the saturation approaches the width of the static island as the absolute value of the external poloidal flux increases.

It is obtained that the stream function after the nonlinear saturation is almost constant for the variation of the external poloidal flux. However, the relation between the phase of the static island and the flow is changed depending on the sign of the external poloidal flux. In the case where the radially outward flow is generated at the X-point of the static island, the island width increases without the phase change. In the case where the radially inward flow is generated at the X-point, the phase change occurs or the island width is decreased. From the point of view of the driven magnetic reconnection, the flow direction is consistent with the change of the width and the phase of the island.

The flow generated by the interchange mode brings the local variation of the pressure through the convection. In the case with the static island, since the flow direction is not changed for the change of the external poloidal flux, the positions of the pressure increase and the pressure decrease are fixed independent of the topology at the position, X-point or O-point. However, the absolute value of the pressure variation depends on the topology at the position. The absolute value is larger at the O-point in the initial static island than at the X-point. This tendency is obtained in either case of that the pressure increases or decreases.

In the case of the effect with the diffusion of the equilibrium pressure, only the saturation solution indicating the increase of the island width is obtained. This result is due to the fact that the parallel diffusion term generates a pressure component which increases the poloidal flux at the resonant surface. The term also accelerates the growth of the interchange mode to reduce the duration of the linear phase. Other property in the behavior and the interchange mode is similar to those in the case without the

parallel diffusion.

Chapter 4

MHD Equilibria including Static Magnetic Islands

4.1 Introduction

Next, we study the effect of the existence of the static island on the growth of the interchange mode. For this study, an equilibrium with the pressure consistent with the static magnetic island is required. Thus, in this Chapter, we develop a numerical code to obtain MHD equilibria consistent with the static magnetic island with the mode numbers of (m, n)=(1,1), which correspond to the reduced MHD equations in a straight heliotron configuration.

As mentioned in Chapter 1, the numerical calculation method in this study is based on the two-step approach of the code by Park et al. [19] and the HINT code [20] which are developed for the three-dimension equilibrium including the magnetic islands and stochastic regions. In the first step, the equation of $\mathbf{B} \cdot \nabla P = 0$ is solved, and in the second step, the force balance equation is solved. Since we treat more simple geometry, we develop a more effective method to solve the equations than these codes. We develop two kinds of equilibrium code with the different treatment of continuity of the pressure gradient across the separatrix of the island. One gives a solution with a continuous pressure gradient at the separatrix and the other gives a solution with a jump of the pressure gradient at the separatrix.

In the former code, the Fourier expansion is employed in the poloidal and the toroidal directions. In the first step, a method utilizing a diffusion equation parallel to the magnetic field is employed. The continuity of the pressure gradient is naturally

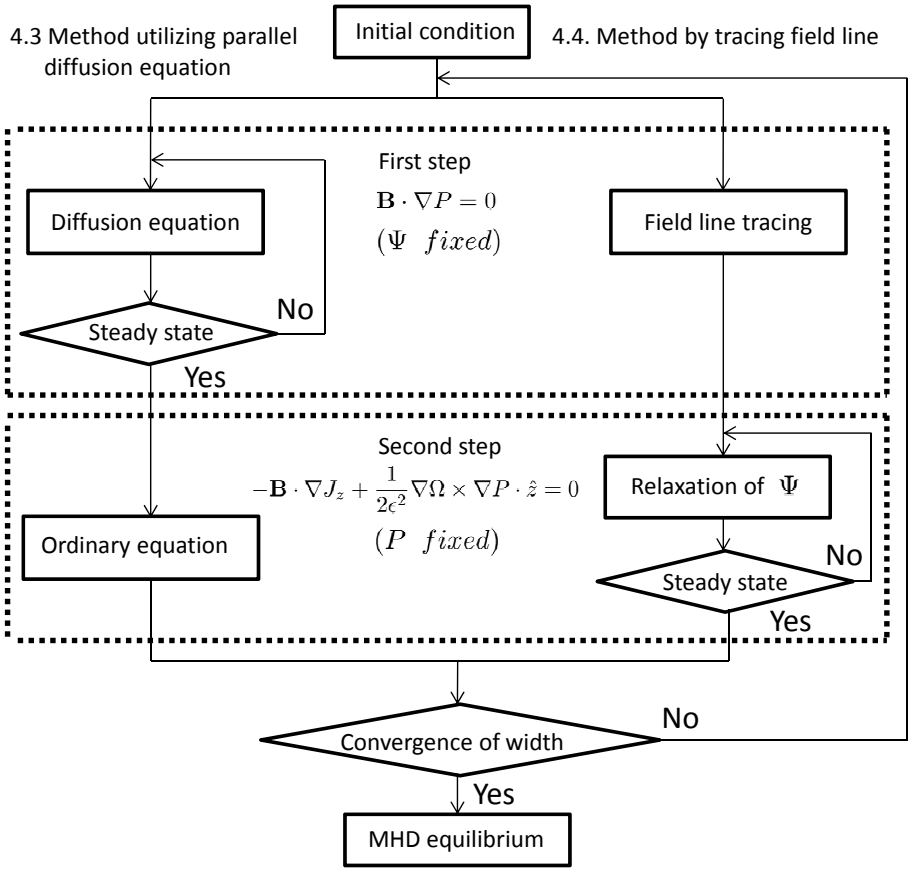

Figure 4.1: Flow chart of the schemes.

assumed in the formulation of the diffusion equation. In the second step, an ordinary differential equation derived from the force balance equation is solved. In general, not only the pressure diffusion parallel to the field but also the diffusion perpendicular to field can affect the equilibrium pressure profile. Thus, we extend the code so as to include the diffusion perpendicular to the field in the first step and study the effect on the equilibrium.

In the calculation with the parallel diffusion equation, the resultant equilibrium pressure profile is flat at both the O-point and the X-point of the magnetic island. The equilibrium is useful for the study of the effect of the local annular flat structure of the pressure profile on the stability of the interchange mode, but not for the pressure profile which is steep at the X-point and flat at the O-point. Ichiguchi et al. [22, 23] examined the effect of the annular flattening of the pressure profile on the stability of the interchange mode. They showed that the marginal width is about quater of the half-width of the mode in the case without the flattening. However, they did not show the stability for the case with the pressure gradient at the X-point. Thus, we

improve a numerical scheme to calculate equilibria with such pressure profile. In this scheme, a field line tracing method is utilized in the first step. We keep the continuity of the pressure at the separatrix by fixing the initial points of the field line tracing. In the second step, a relaxation method is employed, which is similar to the method by Park et al. [19]. This scheme allows us to obtain both solutions of which the pressure gradient is continuous and discontinuous.

This Chapter is organized as follows. The equilibrium equation to be solved is explained in Section 4.2. The scheme with the diffusion equation is explained and the result is discussed in Section 4.3. The tracing field line method is explained in Section 4.4. It is shown that two different solutions are obtained with this method. The difference of the two solutions is discussed in Section 4.5. Summary is given in Section 4.6.

4.2 Coupled equations for equilibrium calculation

The equilibrium corresponding to Eqs.(2.1)-(2.3) has to satisfy the condition that the pressure is constant along a field line, which is given by

$$\mathbf{B} \cdot \nabla P = 0, \tag{4.1}$$

in arbitrary topology and the force balance equation,

$$-\mathbf{B} \cdot \nabla J_z + \frac{1}{2\epsilon^2} \nabla\Omega \times \nabla P \cdot \mathbf{z} = 0. \tag{4.2}$$

Equations (4.1) and (4.2) are the coupled equations for $P(r, \theta, z)$ and $\Psi(r, \theta, z)$ to be solved. The coupled equations are iteratively solved by utilizing two steps employed in the codes of Refs. [18–21]. For the equilibrium calculation, the Field Line Equilibrium Calculation (FLEC) code is developed. The details of the numerical schemes are explained in Appendix B. Here, $\mathbf{B}$ is given by

$$\mathbf{B}(r, \theta, z) = \mathbf{z} + \mathbf{z} \times \nabla\Psi(r, \theta, z). \tag{4.3}$$

We express $\Psi(r, \theta, z)$ as the sum of the cylindrical symmetry component and other components as follows:

$$\Psi(r, \theta, z) = \Psi_{sym}(r) + \Psi^{ext}_{1,1}(r, \theta, z) + \tilde{\Psi}(r, \theta, z). \tag{4.4}$$

Here, "sym" denotes the symmetry components which gives a reference equilibrium with nested magnetic surfaces, and $\Psi^{ext}_{1,1}$ is the external poloidal flux given by Eq.(2.29).

The tilde indicates the variation quantity of equilibrium due to the static island. In this Chapter, $\iota(r)$ is decomposed corresponding to the components of Ψ as

$$\iota(r) = \iota_{sym}(r) + \tilde{\iota}(r), \tag{4.5}$$

where

$$\iota_{sym}(r) = \frac{1}{r}\frac{d\Psi_{sym}(r)}{dr} \quad and \quad \tilde{\iota}(r) = \frac{1}{r}\frac{d\hat{\Psi}_{0,0}(r)}{dr}. \tag{4.6}$$

Here, $\hat{\Psi}_{0,0}$ indicates the Fourier component of $\tilde{\Psi}$ with mode number (m, n)=(0,0). Hereafter, we utilize the model expression for the vacuum field in the straight helical configuration, Ω_{eq} which is given by [28]

$$\Omega_{eq}(r) = \frac{N_t \epsilon^2}{l}\left(r^2 \iota_{sym} + 2\int r\iota_{sym} dr\right), \tag{4.7}$$

where N_t and l are the toroidal period number and the pole number, respectively.

We solve MHD equilibria with two different methods. Figure 4.1 shows the flow chart of the schemes for the equilibria calculation. Left and right charts show the two schemes. In the left chart, the parallel diffusion equation is utilized in the first step. The pressure is solved until the steady state is obtained. In the second step, Ψ satisfying the force balance is obtained by solving an ordinary equation. In right chart, a field line tracing method is utilized to make the pressure constant along the field line in the first step. In the second step, Ψ satisfying the force balance is obtained by utilizing a relaxation method. In both charts, the coupled equations are iteratively solved until the island width is converged. When the island width is converged, we judge that MHD equilibrium is obtained.

4.3 Equilibrium calculation utilizing diffusion equation parallel to the field line

4.3.1 Numerical method

In this Section, MHD equilibrium is discussed by means of the method utilizing diffusion equation parallel to the field line. Here, P is expressed as the sum of the cylindrical symmetry component and other components as in Eq.(4.4)

$$P(r, \theta, z) = P_{sym}(r) + \tilde{P}(r, \theta, z). \tag{4.8}$$

In the case that the system is cylindrical symmetry without an external field, any functions of r for $P_{sym}(r)$ and $\Psi_{sym}(r)$ are the solutions of Eqs.(4.1) and (4.2).

We express $\tilde{P}$ and $\tilde{\Psi}$ with the Fourier series to solve Eqs.(4.1) and (4.2) as follows:

$$\tilde{P}(r,\theta,z) = \sum_{m,n} \tilde{P}_{m,n}, \quad \tilde{P}_{m,n} = \hat{P}_{m,n}(r)\cos(m\theta - nz). \tag{4.9}$$

$$\tilde{\Psi}(r,\theta,z) = \sum_{m,n} \tilde{\Psi}_{m,n}, \quad \tilde{\Psi}_{m,n} = \hat{\Psi}_{m,n}(r)\cos(m\theta - nz). \tag{4.10}$$

In the case that there exists only the static magnetic island with a single mode, only the single helicity modes of $m/n = const.$ are sufficient in the expression of Eqs.(4.9) and (4.10) because of the helical symmetry.

We solve Eqs.(4.1) and (4.2) in two separate steps as shown Fig.4.1. These two steps are iterated until the MHD equilibrium is obtained. In the first step, P satisfying Eq.(4.1) is obtained with Ψ fixed. In this Section, in order to solve Eq.(4.1), we employ a diffusion equation parallel to the field given by

$$\frac{\partial P}{\partial t} = \kappa_{\parallel}(\mathbf{B}\cdot\nabla)(\mathbf{B}\cdot\nabla)P. \tag{4.11}$$

The pressure P constant along the field line is obtained when the stationary state of Eq.(4.11) is achieved. This equation is expanded in the Fourier series. In the present calculation, the modes in the range of $0 \le n \le N_p$ with $N_p = 2$ are employed in Eq.(4.9). Then, P is expressed as

$$P(r,\theta,z) = P_{sym}(r) + \sum_{n=0}^{2} \hat{P}_{n,n}(r)\cos(n\theta - nz). \tag{4.12}$$

The Fourier component of Eq.(4.11) for each mode number of n is written as follows:

$$\frac{\partial \hat{P}_{0,0}}{\partial t} = \frac{\kappa_{\parallel}\Psi_b}{2}\Big[\frac{(1-\epsilon)}{r}\hat{P}_{1,1} + \frac{\Psi_b}{r}\frac{d}{dr}(P_{sym}+\hat{P}_{0,0}) + (1-\epsilon)\frac{d\hat{P}_{1,1}}{dr} - \frac{d\epsilon}{dr}\hat{P}_{1,1} + \Psi_b\frac{d^2}{dr^2}(P_{sym}+\hat{P}_{0,0}) - \frac{\Psi_b}{2}\Big(\frac{d^2\hat{P}_{2,2}}{dr^2} + \frac{3}{r}\frac{d\hat{P}_{2,2}}{dr}\Big)\Big], \tag{4.13}$$

$$\frac{\partial \hat{P}_{1,1}}{\partial t} = \kappa_{\parallel}\Big\{ -(1-\epsilon)[(1-\epsilon)\hat{P}_{1,1} + \Psi_b\frac{d}{dr}(P_{sym}+\hat{P}_{0,0})] + \frac{\Psi_b^2}{4}\Big(\frac{d^2\hat{P}_{1,1}}{dr^2} + \frac{1}{r}\frac{d\hat{P}_{1,1}}{dr} - \frac{1}{r^2}\hat{P}_{1,1}\Big) + \frac{3\Psi_b}{2}(1-\epsilon)\frac{d\hat{P}_{2,2}}{dr} + 3\Psi_b(1-\epsilon)\frac{\hat{P}_{2,2}}{r} - \Psi_b\frac{d\epsilon}{dr}\hat{P}_{2,2}\Big\} \tag{4.14}$$

and

$$\frac{\partial \hat{P}_{2,2}}{\partial t} = \kappa_{\parallel}\Big\{ -2(1-\epsilon)[2(1-\epsilon)\hat{P}_{2,2} + \frac{\Psi_b}{2}\Big(\frac{d\hat{P}_{1,1}}{dr} - \frac{1}{r}\hat{P}_{1,1}\Big)]$$

$$+\frac{\Psi_b}{2}\Big[\frac{1-\iota}{r}\hat{P}_{1,1}+\frac{\Psi_b}{r}\frac{d}{dr}(P_{sym}+\hat{P}_{0,0})+\frac{d\iota}{dr}\hat{P}_{1,1}-(1-\iota)\frac{d\hat{P}_{1,1}}{dr}\Big]$$
$$-\Psi_b\frac{d^2}{dr^2}(P_{sym}+\hat{P}_{0,0})+\frac{\Psi_b^2}{2}\Big(\frac{d^2\hat{P}_{2,2}}{dr^2}+\frac{1}{r}\frac{d\hat{P}_{2,2}}{dr}-\frac{4}{r^2}\hat{P}_{2,2}\Big)\Big\}. \tag{4.15}$$

In order to judge the achievement of the steady state of Eq.(4.11), we define a parameter of K_n for each mode number as

$$K_n=\int_0^1\{\hat{P}_{n,n}(r)\}^2 r dr. \tag{4.16}$$

We calculate the growth rate γ_n given by

$$\gamma_n=\frac{1}{K_n}\frac{dK_n}{dt} \tag{4.17}$$

and $d\gamma_n/dt$ every time step in the time evolution. When both conditions of

$$|\gamma_n|<\epsilon_p \quad and \quad \Big|\frac{d\gamma_n}{dt}\Big|<\epsilon_p \quad (\epsilon_p << 1) \tag{4.18}$$

are satisfied simultaneously for each mode, we judge that the steady state is achieved.

In the second step, Eq.(4.2) is solved with P fixed, which is obtained by the first step. To obtain the equilibrium including static magnetic island with the single mode of (m,n)=(1,1), we employ the modes in the range of $0\le n\le N_\Psi$ with $N_\Psi=1$ for $\tilde{\Psi}$. In this case, Eq.(4.4) is written as

$$\Psi(r,\theta,z)=\Psi_{sym}(r)+\Psi_b r\cos(\theta-z)+\hat{\Psi}_{0,0}(r)+\hat{\Psi}_{1,1}(r)\cos(\theta-z). \tag{4.19}$$

In this case, Jz is expressed as

$$Jz(r,\theta,z)=Jz_{sym}(r)+\hat{J}z_{0,0}(r)+\hat{J}z_{1,1}(r)\cos(\theta-z). \tag{4.20}$$

In this study, no current condition for cylindrical equilibrium, $Jz_{sym}=0$ is assumed. We also expand Eq.(4.2) in the Fourier series. The $n=0$ component of Eq.(4.2) is satisfied trivially in this case. The $n=1$ component is written as

$$-\mathbf{z}\cdot\nabla\tilde{J}z_{1,1}-[\Psi_{sym}+\tilde{\Psi}_{0,0},\tilde{J}z_{1,1}]-[\Psi^{ext}_{1,1}+\tilde{\Psi}_{1,1},\tilde{J}z_{0,0}]+\frac{1}{2\epsilon^2}[\Omega_{sym},\tilde{P}_{1,1}]=0, \tag{4.21}$$

where $[f,g]$ is the Poisson bracket which is defined as

$$[f,g]=\nabla f\times\nabla g\cdot\mathbf{z}. \tag{4.22}$$

Equation (4.21) has the solution of

$$\tilde{\Psi}_{1,1}=\tilde{J}z_{1,1}=0 \tag{4.23}$$

and $\tilde{\Psi}_{0,0}$ satisfying

$$\frac{d\hat{J}z_{0,0}}{dr} = -\frac{1}{2\epsilon^2\Psi_b r}\frac{d\Omega_{sym}}{dr}\hat{P}_{1,1}. \tag{4.24}$$

Thus, the force balance equation (4.2) is reduced to an ordinary differential equation for $\hat{\Psi}_{0,0}$. We obtain the solution for Ψ by solving Eq.(4.24) for $\hat{\Psi}_{0,0}$ and substituting it into Eq.(4.19).

The width of the magnetic island w_N is evaluated by using the solution of Ψ, where the subscript of N means the number of the iteration. The two steps described above are iterated until the width w_N is converged. When the change rate δw_N satisfies the condition,

$$|\delta w_N| < \epsilon_w \quad (\epsilon_w << 1), \tag{4.25}$$

we judge that the MHD equilibrium is obtained, where δw_N is defined as

$$\delta w_N = \frac{w_N - w_{N-1}}{w_{N-1}}. \tag{4.26}$$

The island width is calculated from the shape of the magnetic island. The shape can be drawn by tracing the field line equations given by

$$\frac{dr}{dz} = \frac{B_r}{B_z} \tag{4.27}$$

and

$$\frac{d\theta}{dz} = \frac{B_\theta}{rB_z}. \tag{4.28}$$

In the case of the helical symmetry with the mode numbers of (m, n), the magnetic island shape can be drawn in an efficient way rather than tracing the Poincaré plots. We express the solution for Eqs.(4.27) and (4.28) as $(r(z), \theta(z))$ for the initial condition of $(r(z_0), \theta(z_0))$ at $z = z_0$. In the change of the z direction, the magnetic islands rotate $(m/n)(z - z_0)$ in the θ direction with keeping the shape. We can obtain the island shape at the cross section of $z = z_0$ by plotting the line of $(r(z), \theta(z) - (m/n)(z - z_0))$. This procedure corresponds to subtracting the phase $(m/n)(z - z_0)$ in θ direction from the solution $\theta(z)$. Figure 4.2 shows magnetic surface at $z = 0$, which corresponds to the separatrix of the static island for $\Psi_b = 2.0 \times 10^{-3}$. Blue line and red dots indicate the line of $(r(z), \theta(z) - (m/n)(z))$ and the Poincaré plots, respectively. The Poincaré plots are on the line of $(r(z), \theta(z) - (m/n)(z))$. It is confirmed that magnetic surfaces are plotted continuously by utilizing the line.

In the case of the magnetic island with (m, n), there exist X-point and O-point at the points where the right hand side of Eq.(4.28) equals to m/n. When the mode

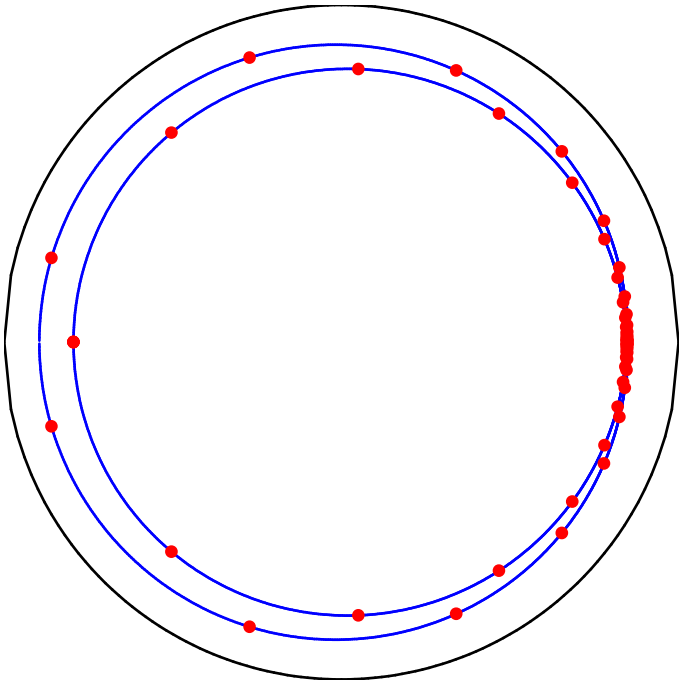

Figure 4.2: Magnetic surface at $z = 0$ corresponding to the separatrix of the static island for $\Psi_b = 2.0 \times 10^{-3}$. Blue line and red dots indicate the line of $(r(z), \theta(z) - (m/n)(z))$ and the Poincaré plots, respectively.

numbers are (m, n)=(1,1), Eq.(4.28) combined with Eqs.(2.4), (4.6), (4.19) and (4.23) become

$$\frac{d\theta}{dz} = \iota + \frac{\Psi_b}{r}\cos(\theta - z). \tag{4.29}$$

In the case of positive Ψ_b, there exist X-point at $\theta = 0$ and O-point at $\theta = \pi$ in the $z = 0$ cross section. The radial coordinates r's for X-point and O-point satisfy

$$\iota + \frac{\Psi_b}{r} = 1 \quad and \quad \iota - \frac{\Psi_b}{r} = 1, \tag{4.30}$$

respectively. Therefore, the radial positions of X-point, O-point and the rational surface with $\iota = 1$ are different because of the finite value of Ψ_b.

4.3.2 Resultant equilibrium

By using the method explained in Section 4.3.1, we obtain the MHD equilibria including static magnetic islands in a straight heliotron plasma. The pressure profile,

$$P_{sym}(r) = \beta_0(1 - r^4)^2, \quad \hat{P}_{n,n}(r) = 0 \ \ (0 \leq n \leq 2) \tag{4.31}$$

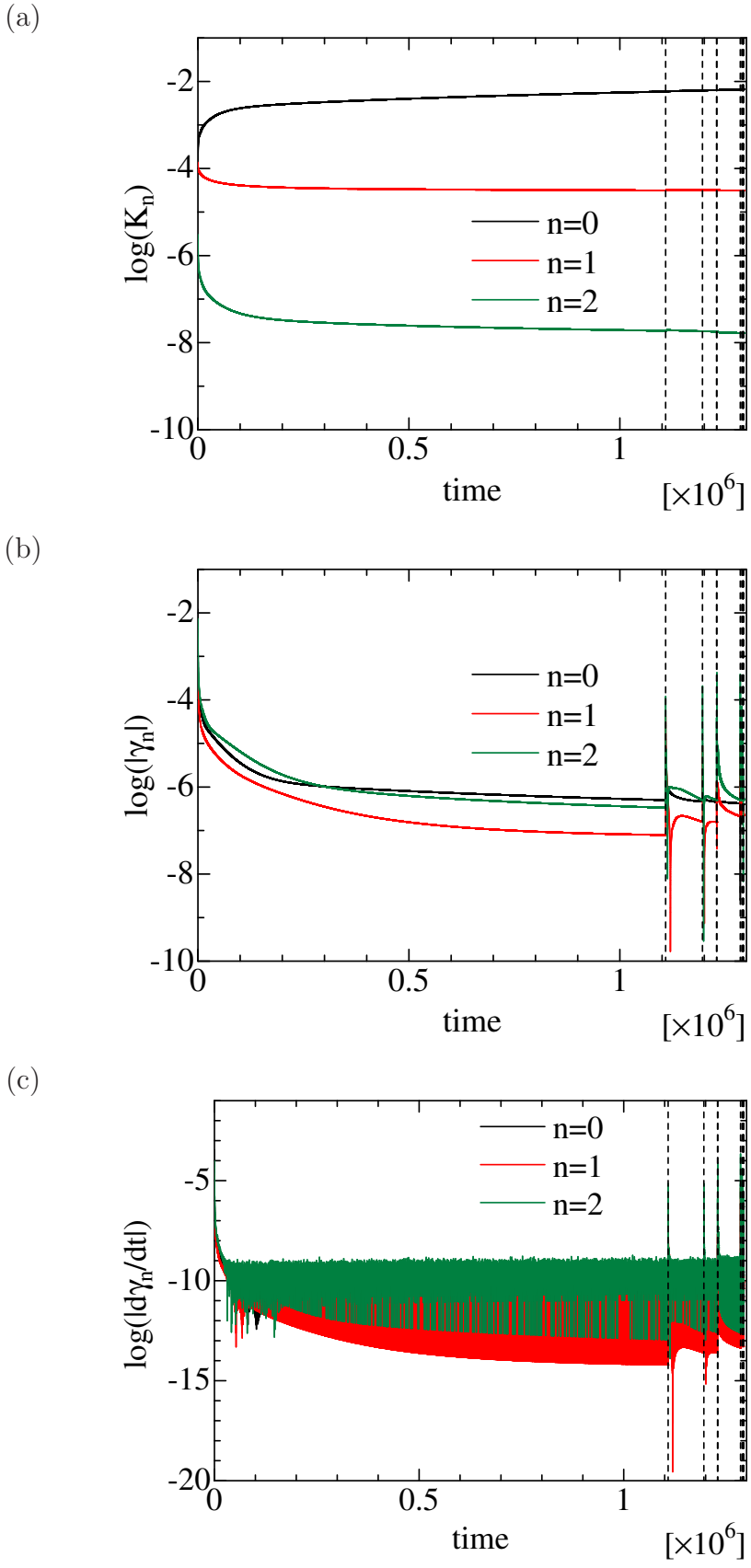

Figure 4.3: Time evolution of (a) K_n, (b) $|\gamma_n|$ and (c) $|d\gamma_n/dt|$ for $\kappa_\perp/\kappa_\parallel = 0$. Dashed lines indicate the times when the steady state condition is satisfied and the second step is conducted.

with $\beta_0 = 0.16\%$ is used for the initial condition. The profile of the initial rotational transform profile is shown in Fig.3.1(b). The profile of Ψ_{sym} is obtained by applying this profile to Eq.(4.6). The value of Ψ_b and the initial condition for $\hat{\Psi}_{m,n}$ are set to be $\Psi_b = 10^{-3}$ and $\hat{\Psi}_{m,n} = 0$, respectively. We employ $\epsilon_p = 5.0 \times 10^{-7}$ and $\epsilon_w = 10^{-6}$ as the convergence parameters.

Figure 4.3 shows the time evolution of K_n, $|\gamma_n|$ and $|d\gamma_n/dt|$ over the whole iteration. Dashed lines show the times when the steady state condition in the first step is achieved and the second step is conducted. It is found that the steady state of each component $\hat{P}_{n,n}$ is smoothly achieved for each iteration. Figure 4.4 shows w_N and $|\delta w_N|$ at the times of the dashed lines in Fig.4.3 as functions of N. As N increases, the island width becomes converged. The convergence condition is satisfied and the equilibrium is obtained at $N = 12$.

Figure 4.5 shows the profiles of the components of the equilibrium pressure $\hat{P}_{n,n}$. The component of $\hat{P}_{0,0}$ is dominant and $\hat{P}_{2,2}$ is much smaller than $\hat{P}_{1,1}$. The ratios of the maximum value of $|\hat{P}_{2,2}|$ to those of $|\hat{P}_{0,0}|$ and $|\hat{P}_{1,1}|$ are $|\hat{P}_{2,2}|/|\hat{P}_{0,0}| = 7.1 \times 10^{-4}$ and $|\hat{P}_{2,2}|/|\hat{P}_{1,1}| = 1.4 \times 10^{-2}$, respectively. This result confirms that $N_p = 2$ is adequate in the first step calculation.

Figure 4.6 (a) and (b) show the contour of the constant pressure and the magnetic surfaces at the $z = 0$ cross section in the resultant equilibrium. Since $\hat{P}_{2,2}$ is much smaller than $\hat{P}_{0,0}$ and $\hat{P}_{1,1}$ as described above, the contribution of $\hat{P}_{2,2}$ to the pressure contour is negligible. For this reason, we exclude $\tilde{P}_{2,2}$ in Eq.(4.12) when we plot the pressure contour in Fig.4.6(a). Figure 4.6 (a) and (b) show a good agreement between the pressure contour and the magnetic surfaces. The separatrix exists also in the pressure contour which corresponds to that of the magnetic island. Figure 4.6 (c) shows the relative error δC in the pressure along the field line. The definition of δC is given by

$$\delta C(r, \theta - z) = \frac{P(r, \theta - z) - P(r_0, \theta_0 - z_0)}{P(r_0, \theta_0 - z_0)}. \tag{4.32}$$

The relative error is evaluated along the field line of the total pressure without the component of $n = 2$. Since the phase angle $\theta - z$ varies along the field line, we evaluate δC as a function of $\theta - z$. The subscript ' 0 ' means the coordinates of the starting point of the field line. In Fig.4.6 (c), $\theta_0 = \pi$ and $z_0 = 0$ are used. The field lines corresponding to r_0= 0.329, 0.591, 0.781, 0.816 and 0.950 are chosen here. For fixed values of θ_0 and z_0, the radial coordinate r_0 identifies the magnetic surface on which the field line is traced. The field lines of r_0 =0.329, 0.591 and 0.781 are on the magnetic

surfaces inward of the separatrix (red, brown and green), $r_0 = 0.816$ on the separatrix (blue) and $r_0 = 0.950$ the surface outward of the separatrix (purple), respectively. Each line in Fig.4.6(c) corresponds to the magnetic surface with the same color in Fig.4.6(b). Figure 4.6(c) shows that the largest error of the pressure appears on the field line of the separatrix (blue). Even in the case, however, the value is quite small and less than 5.0×10^{-3}. Therefore, Eq.(4.1) is satisfied in a good accuracy.

Figure 4.7 (a) shows the equilibrium pressure profile along the line connecting $(r = 1, \theta = 0, z = 0)$ and $(r = 1, \theta = \pi, z = 0)$. Figure 4.7 (b) and (c) are the enlarged figures around the magnetic island at $\theta = 0$ and $\theta = \pi$, respectively. The pressure profiles of both cases with and without $\tilde{P}_{2,2}$ are plotted in Fig.4.7. However, the difference between the cases is too small to be distinguished because $|\hat{P}_{2,2}|$ is much less than others as shown in Fig.4.5. The pressure profile is flat not only at the O-point but also at the X-point. This property is explained with the expression of the Fourier component of $\mathbf{B} \cdot \nabla P$. In the equilibrium, each Fourier coefficient of $\mathbf{B} \cdot \nabla P$ is zero. The $(m, n) = (1, 1)$ coefficient is given by

$$(\mathbf{B} \cdot \nabla P)_{1,1} = (1 - \iota)\hat{P}_{1,1} + \Psi_b \frac{d}{dr}(P_{sym} + \hat{P}_{0,0}) \tag{4.33}$$

under the condition of $\hat{P}_{n,n} = 0$ for $n \geq 2$. Since the first term equals to zero at the $\iota = 1$ surface, the relation of $d/dr(P_{sym} + \hat{P}_{0,0}) = 0$ must be satisfied. This equation indicates that the pressure profile is flat in the annular region near the surface involving both the O-point and the X-point.

In Fig.4.7 (b) and (c), the horizontal purple line shows the pressure value corresponding to the separatrix in the pressure contour shown in Fig.4.6 (a). These figures show that the pressure has the same value at the X-point and at the separatrix at $\theta = \pi$ of the magnetic surfaces. This result also confirms that the separatrix in the pressure contour coincides with the separatrix in the magnetic surfaces.

We confirm that the resultant pressure satisfies Eq.(4.1) in another way. We calculate an averaged pressure along the field line going through a given point Q defined as

$$\bar{P}_Q = \frac{\int \frac{P}{B} dl}{\int \frac{1}{B} dl} \tag{4.34}$$

by using the resultant pressure P. Here, dl is the length of the arc along the field line. Then, we replace the pressure with $\bar{P}_Q$ along the field line. It is followed that the pressure profile determined by $\bar{P}_Q$ automatically satisfies Eq.(4.1). This method is employed in the HINT code [21, 29]. Figure 4.8 shows the profiles of the resultant

pressure and the averaged pressure along field line with $\bar{P}_Q$. Red solid line and green dashed line show the profiles of the resultant equilibrium pressure and the averaged pressure, respectively. Good agreement is obtained, which confirms that the resultant pressure satisfies Eq.(4.1).

4.3.3 Pressure profile with perpendicular heat conductivity

In the magnetically confined plasma with a pressure gradient, the pressure is diffused following Eq.(2.3). The time scale of the parallel diffusion is much shorter than that of the perpendicular diffusion. Therefore, in the steady state, a static MHD equilibrium corresponding to the condition $\mathbf{B} \cdot \nabla P = 0$ is considered to be achieved in a short time as the lowest approximation. As the next approximation, we consider to include the perpendicular diffusion. In the steady state of this case, a flow consistent with the diffusion should be taken into account. However, the incorporation of such a flow is quite complicated because the flow is determined not only by the pressure equation but also other transport equations. Thus, we assume the steady state with no flow for the approximation. Furthermore, for the steady state including the perpendicular diffusion, a heat source S_P is needed in the pressure equation to compensate the decay of the total pressure. Here we also assume the source term corresponding to the form of $S_P = -\nabla_\perp^2 P_{sym}$ in the pressure equation. Then, the resultant equation is given by

$$\kappa_\perp \nabla_\perp^2 \tilde{P} + \kappa_\parallel (\mathbf{B} \cdot \nabla)(\mathbf{B} \cdot \nabla) P = 0. \tag{4.35}$$

By solving this equation together with Eq.(4.2), we can obtain a steady state with the perpendicular pressure diffusion with no flow including a static magnetic island. The solution is not an MHD equilibrium because the condition of $\mathbf{B} \cdot \nabla P = 0$ is not satisfied. However, we can obtain the contribution of the perpendicular diffusion on the MHD equilibrium from the solution. To solve the equations, we employ the diffusion equation given by

$$\frac{\partial P}{\partial t} = \kappa_\perp \nabla_\perp^2 \tilde{P} + \kappa_\parallel (\mathbf{B} \cdot \nabla)(\mathbf{B} \cdot \nabla) P \tag{4.36}$$

instead of Eq.(4.11) for the first step and utilize the same scheme as in the Subsection 4.3.2 for the second step.

Figure 4.9 shows the time evolution of K_n, $|\gamma_n|$ and $|d\gamma_n/dt|$ over all the iterations in the case with $\kappa_\perp/\kappa_\parallel = 10^{-7}$. In the first step, the steady state of Eq.(4.36) is obtained as in the case of $\kappa_\perp/\kappa_\parallel = 0$. As shown in Fig.4.4(b), the convergence for the island width is also obtained in the result of the two-step iteration. In the case

of $\kappa_\perp/\kappa_\parallel = 10^{-7}$, the equilibrium is obtained at $N = 6$. Similar time evolutions are obtained in the cases with $\kappa_\perp/\kappa_\parallel = 10^{-6}, 10^{-8}, 10^{-9}$ and 10^{-10} as shown in Fig.4.4(a). The island width in the equilibrium state decreases compared with the vacuum width in the case of $\kappa_\perp/\kappa_\parallel = 0$ while the island widths increase in the cases of $\kappa_\perp/\kappa_\parallel \neq 0$. Figure 4.10 shows the dependence of the equilibrium pressure profile along the line connecting $(r = 1, \theta = 0, z = 0)$ and $(r = 1, \theta = \pi, z = 0)$ on $\kappa_\perp/\kappa_\parallel$. As $\kappa_\perp/\kappa_\parallel$ increases, the pressure gradient at the X-point enhances. In the case with $\kappa_\perp/\kappa_\parallel = 10^{-7}$, the flat region almost disappears at the X-point. The local flat structure at the O-point is maintained for the finite value of $\kappa_\perp/\kappa_\parallel$, however, the width of the flat region decreases with the increase of $\kappa_\perp/\kappa_\parallel$.

In spite of that we do not take the diffusion for $P_{sym}(r)$ into account, the reduction of $P(r = 0)$ in the resultant equilibrium is seen in Fig.4.10(a). This is due to the fact that $\hat{P}_{0,0}$ has a negative finite value at $r = 0$ generated by the diffusion perpendicular to the field as shown in Fig.4.11. Two kinds of contribution of the perpendicular diffusion on $\hat{P}_{0,0}$ around the rational surface and the magnetic axis lead to the negative value of $\hat{P}_{0,0}(r = 0)$. As shown in Fig.4.5, the profile of $\hat{P}_{0,0}$ locally has a negative value region just inside the rational surface in the case of $\kappa_\perp/\kappa_\parallel = 0$. In the case of finite $\kappa_\perp/\kappa_\parallel$, the radial diffusion term works so as to reduce the curvature of the profile. It is followed that the region with the negative $\hat{P}_{0,0}$ is enlarged. On the other hand, in the region around the magnetic axis, $\hat{P}_{0,0}$ is almost zero in the case of $\kappa_\perp/\kappa_\parallel = 0$ as shown in Fig.4.5, because the island effect is limited to the region around the rational surface. In the cases of finite $\kappa_\perp/\kappa_\parallel$, the first term is dominant in Eq.(4.36), and therefore, $\hat{P}_{0,0}$ satisfies the equation of

$$(\nabla_\perp^2 \tilde{P})_{0,0} = \frac{d^2 \hat{P}_{0,0}}{d^2 r} + \frac{1}{r}\frac{d\hat{P}_{0,0}}{dr} = 0, \tag{4.37}$$

in this region. The solution of Eq.(4.37) which is regular at the axis is a constant. Therefore, the finite value of $\kappa_\perp/\kappa_\parallel$ makes the pressure profile constant around the axis. Since the solution of $\hat{P}_{0,0}$ has to be continuous between the regions around the rational surface and the axis, $\hat{P}_{0,0}$ has a finite and negative value at $r = 0$ as shown in Fig.4.11. That is, $P(r = 0)$ is decreased in the cases with finite value of $\kappa_\perp/\kappa_\parallel$. The absolute value of the decrease of $\hat{P}_{0,0}(r = 0)$ does not change monotonously for the increase of $\kappa_\perp/\kappa_\parallel$ as shown Fig.4.10(a). This is because the two contributions are almost in a trade-off relation. In the increase of $\kappa_\perp/\kappa_\parallel$, the maximum absolute value of $\hat{P}_{0,0}$ around the rational surface is decreased because of the reduction of the curvature of $\hat{P}_{0,0}$ while the contribution making $\hat{P}_{0,0}$ constant is enhanced.

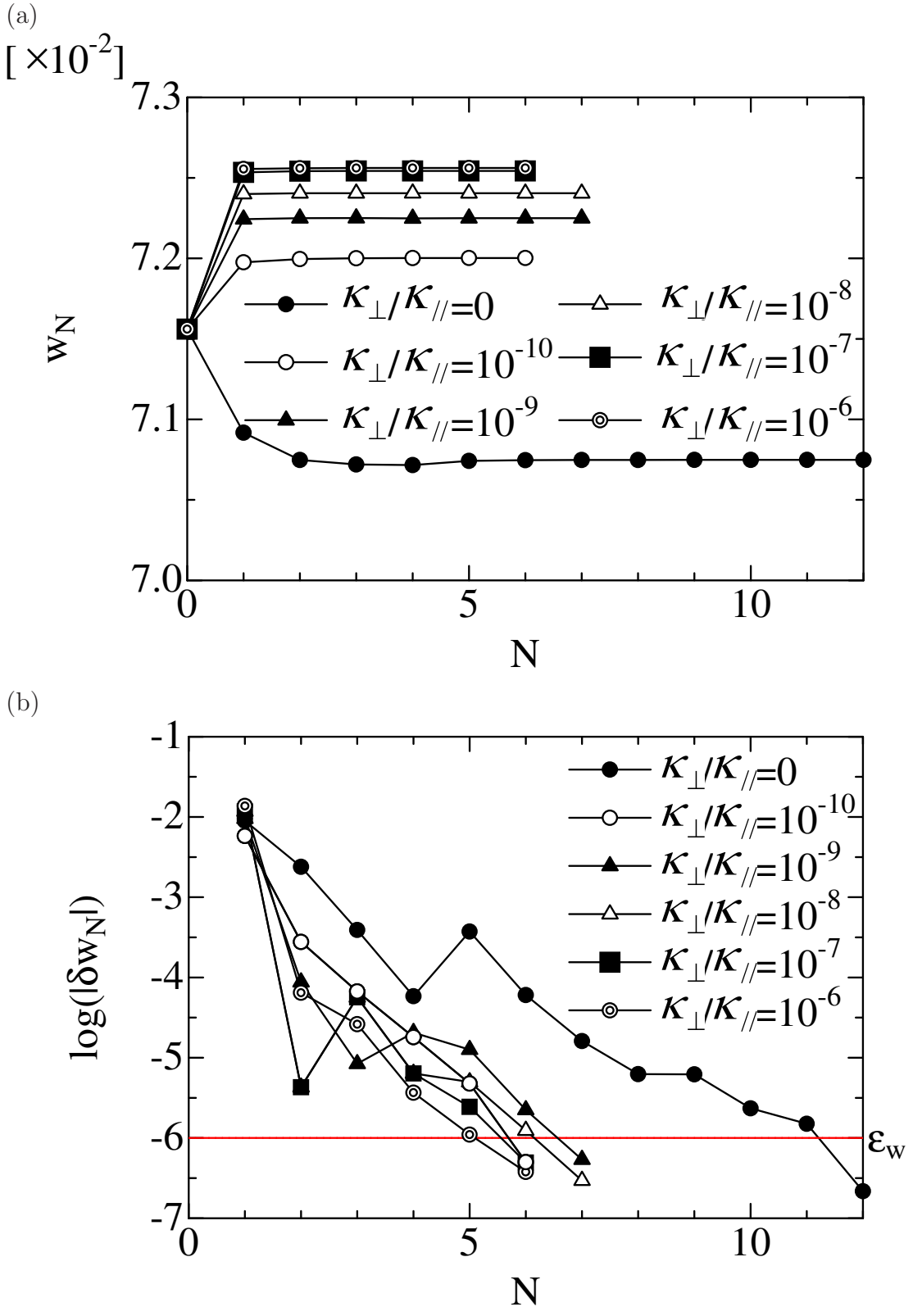

Figure 4.4: Variation of (a) w_N and (b) δw_N for the number of iteration N. The plot of $\kappa_\perp/\kappa_\parallel = 0$ corresponds to the case of Fig.4.3.

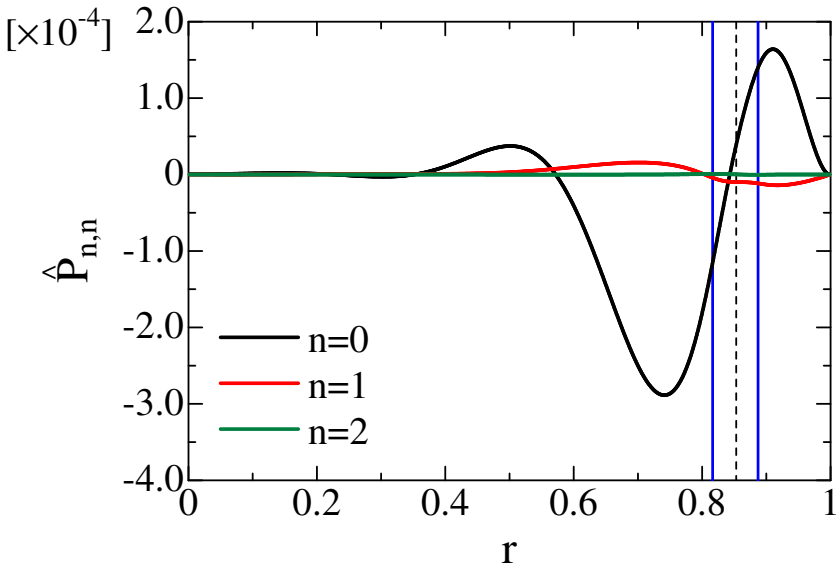

Figure 4.5: Profiles of $\hat{P}_{n,n}$. Dashed lines indicate the position of the rational surface. Blue lines indicate the position of the separatrix of the island at $\theta = \pi$.

(a)

(b)

(c)

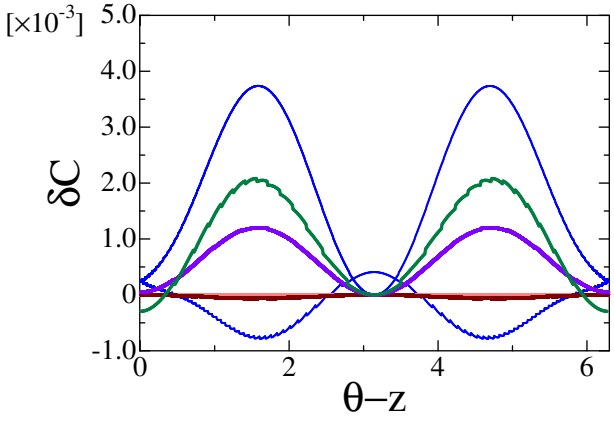

Figure 4.6: Plots of (a) pressure contour and (b) magnetic surfaces of the resultant equilibrium at $\beta_0 = 0.16\%$ on $z = 0$ cross section and (c) relative error of pressure along field lines. Each field line in (c) is on the surface with the same color in (b).

(a)

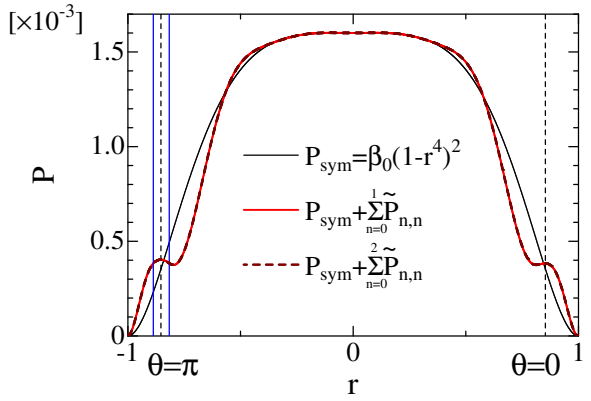

(b)

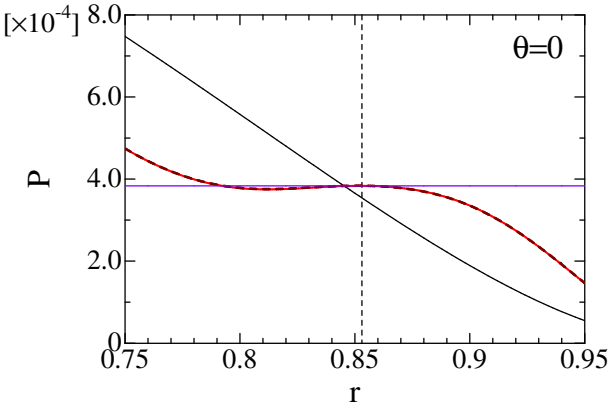

(c)

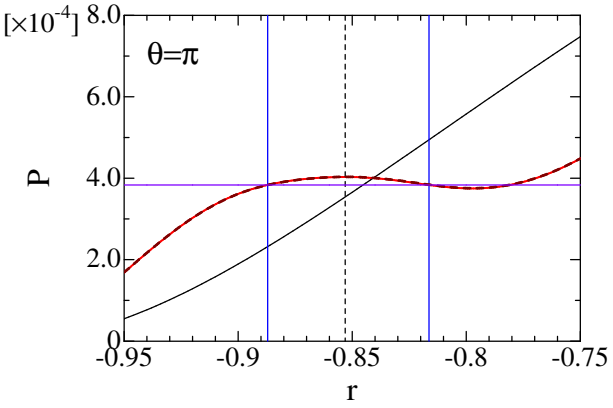

Figure 4.7: Profile of resultant equilibrium pressure (a) along the line connecting ($r = 1, \theta = 0, z = 0$) and ($r = 1, \theta = \pi, z = 0$) and its enlargements at (b) $\theta = 0$ and (c) $\theta = \pi$. Red solid line and brown dashed line show the profiles of $P_{sym} + \sum_{n=0}^{1} \tilde{P}_{n,n}$ and $P_{sym} + \sum_{n=0}^{2} \tilde{P}_{n,n}$, respectively. Black line shows the profile of P_{sym}. Vertical dashed lines indicate the position of the rational surface. Blue lines indicate the positions of the separatrix of the magnetic island at $\theta = \pi$. Green line indicates the position of the O-point. Horizontal purple line indicates the value of pressure at the separatrix in the pressure contour surfaces in Fig.4.6(a), $P = 3.942 \times 10^{-4}$. Brown line includes $\tilde{P}_{2,2}$.

(a)

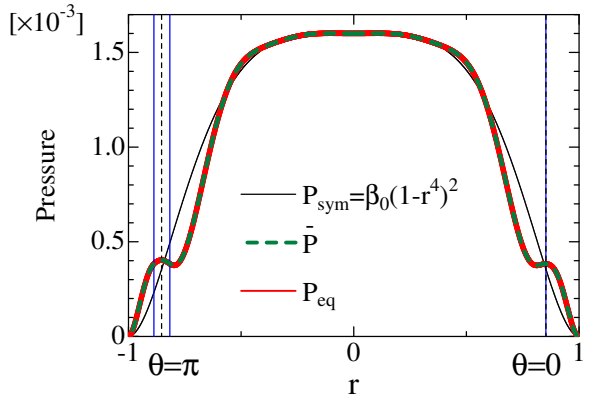

(b)

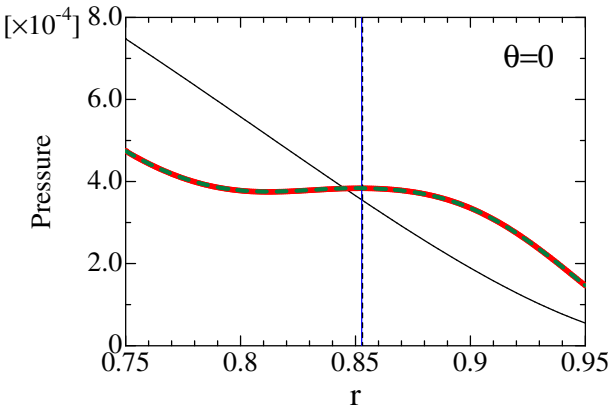

(c)

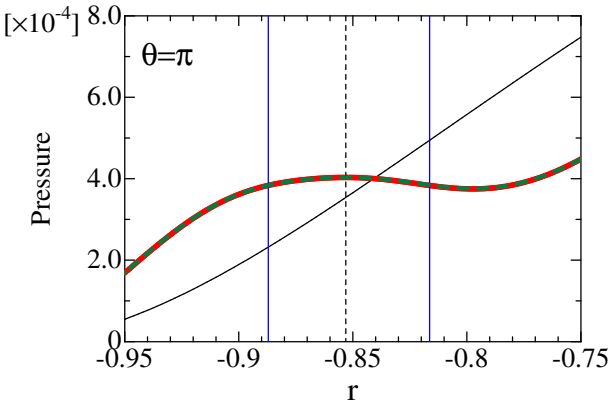

Figure 4.8: Profiles of the resultant equilibrium pressure and the averaged pressure along field line (a) along the line connecting $(r = 1, \theta = 0, z = 0)$ and $(r = 1, \theta = \pi, z = 0)$ and its enlargements at (b) $\theta = 0$ and (c) $\theta = \pi$. Red solid line and green dashed line show the profiles of the resultant equilibrium pressure and the averaged pressure, respectively. Black line shows the profile of P_{sym}. Vertical dashed lines indicate the position of the rational surface. Blue lines indicate the positions of the separatrix of the magnetic island.

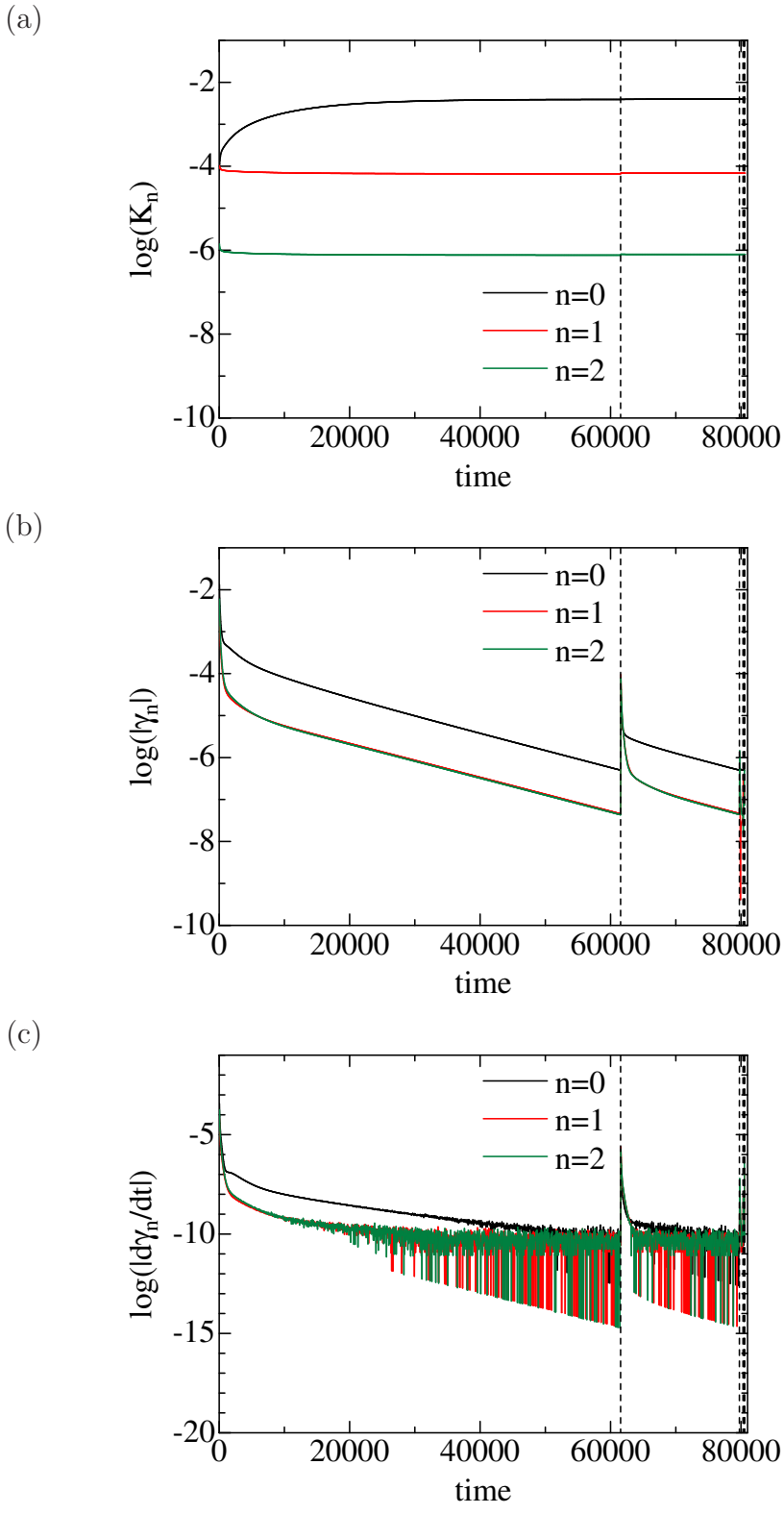

Figure 4.9: Time evolution of (a) K_n, (b) $|\gamma_n|$ and (c) $|d\gamma_n/dt|$ for $\kappa_\perp/\kappa_\parallel = 10^{-7}$. Dashed lines indicate the times when the steady state condition is satisfied and the second step is conducted.

(a)

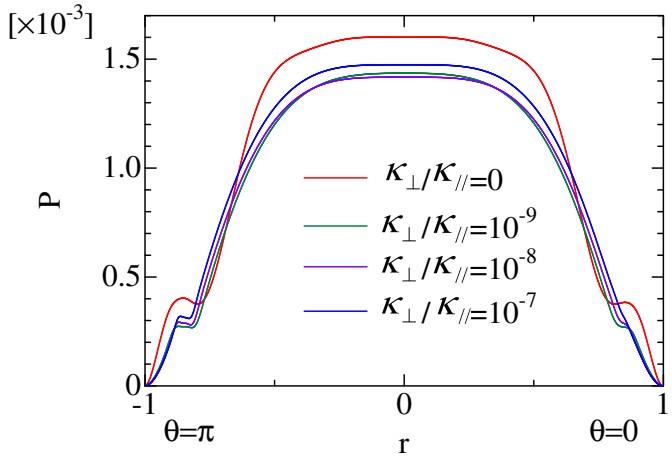

(b)

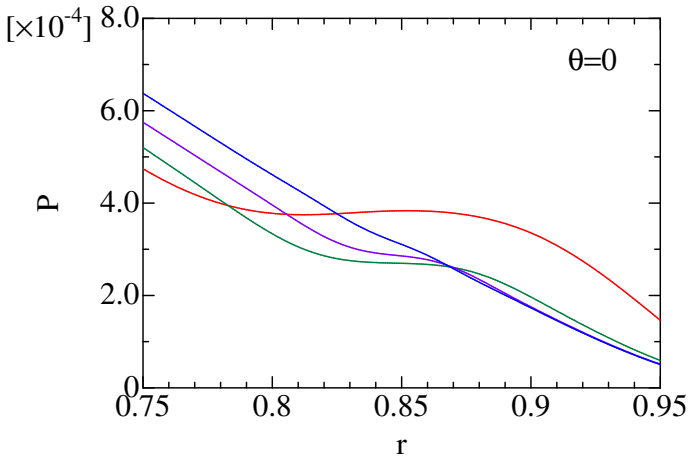

(c)

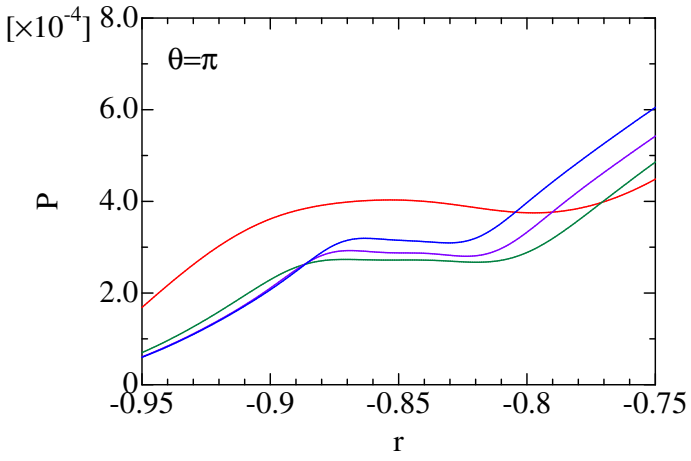

Figure 4.10: Profiles of resultant pressure (a) along the line connecting $(r = 1, \theta = 0, z = 0)$ and $(r = 1, \theta = \pi, z = 0)$ and its enlargements at (b) $\theta = 0$ and (c) $\theta = \pi$ for $\kappa_\perp/\kappa_\parallel = 0$, 10^{-9}, 10^{-8} and 10^{-7}.

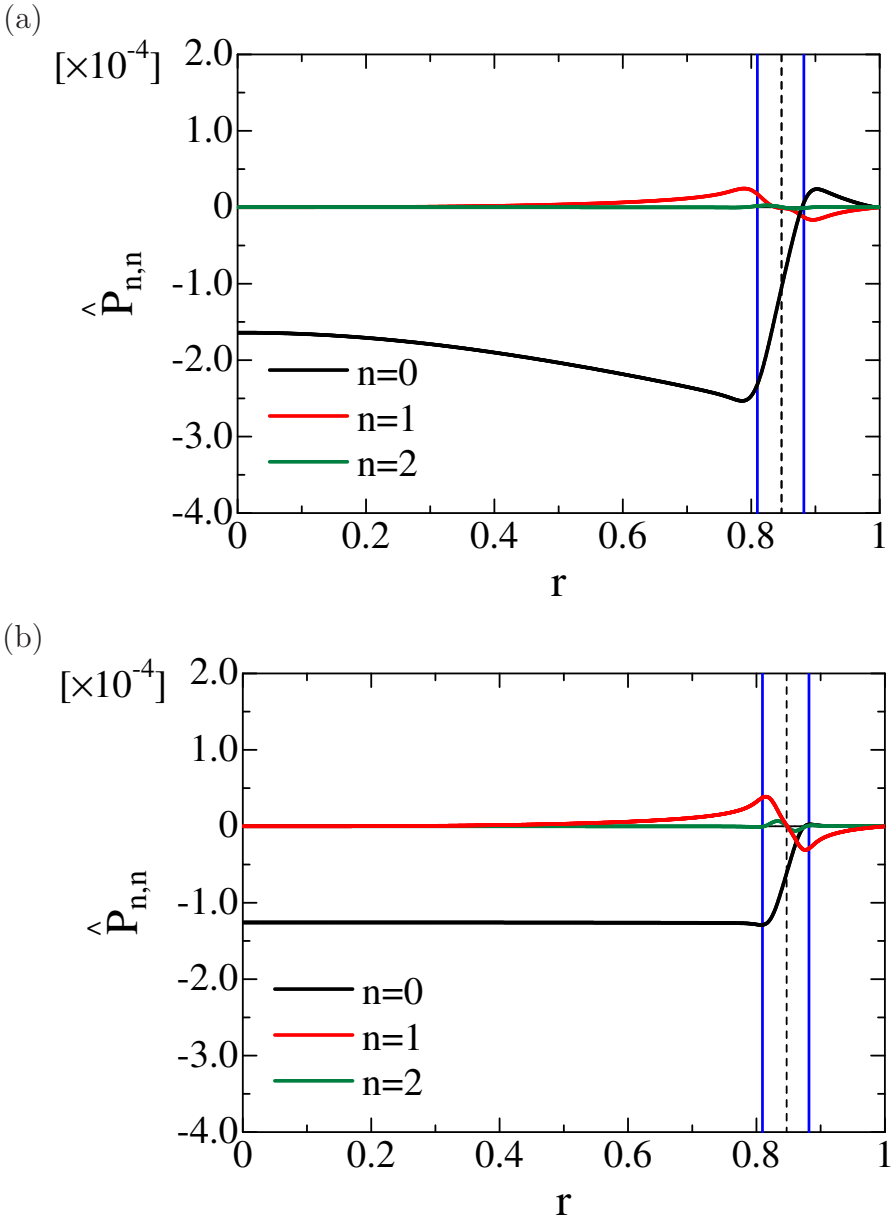

Figure 4.11: Profiles of $\hat{P}_{n,n}$ for (a) $\kappa_\perp/\kappa_\parallel = 10^{-9}$ and (b) $\kappa_\perp/\kappa_\parallel = 10^{-7}$. Dashed lines indicate the position of the rational surface. Blue lines indicate the position of the separatrix of the island at $\theta = \pi$.

4.4 Method by tracing field line

4.4.1 Averaged pressure along the field line

In the previous Section, Eq.(4.11) is employed to obtain the equilibrium pressure. However, the resultant pressure is flat at not only the O-point but the X-point. In this Section, we seek the equilibrium pressure with a finite gradient at the X-point by means of a field line tracing method.

One way to obtain the equilibrium pressure with a finite pressure gradient is the method averaging P_{sym} along the field line by using Eq.(4.34).

Figure 4.12 shows the profile of $\bar{P}$ for $\Psi_b = 1.0 \times 10^{-3}$. Here, $P_{sym}(r)$ is defined in Eq.(4.31). Red dots and black line show the averaged pressure $\bar{P}$ and P_{sym}, respectively. Vertical blue lines indicates the separatrix of the static island. Here, r_X, r_a and r_b indicate the radial coordinate of the X-point, the radial coordinates of the inside and outside of the separatrix at $\theta = \pi$, respectively. The averaged pressure $\bar{P}$ is discontinuous at the X-point. The reason is as follows. The field line which starts from $(r_0 < r_X, \theta = 0)$ reaches $(r_\pi < r_a, \theta = \pi)$, where r_0 and r_π denote the radial coordinate of the starting point and of the arrival point at $\theta = \pi$ of the field line. Since $P_{sym}(r_\pi)$ is larger than $P_{sym}(r_0)$, $\bar{P}(r_0) > P_{sym}(r_0)$ at $\theta = 0$ for $r_0 < r_X$. On the other hand, the field line which starts from $(r_0 > r_X, \theta = 0)$ reaches $(r_\pi > r_b, \theta = \pi)$. Since $P_{sym}(r_\pi)$ is less than $P_{sym}(r_0)$, $\bar{P}(r_0) < P_{sym}(r_0)$ at $\theta = 0$ for $r_0 > r_X$. When a field line traces the separatrix, the field line goes through both of $r = r_a$ and $r = r_b$. Therefore, both $\lim_{r_{0+} \to r_X} \bar{P}(r_0)$ and $\lim_{r_{0-} \to r_X} \bar{P}(r_0)$ do not equal to $\bar{P}(r_X)$. As a result, the averaged pressure $\bar{P}(r_0)$ is discontinuous at the X-point. For this reason, averaged field line method defined as Eq.(4.34) is not employed in this study.

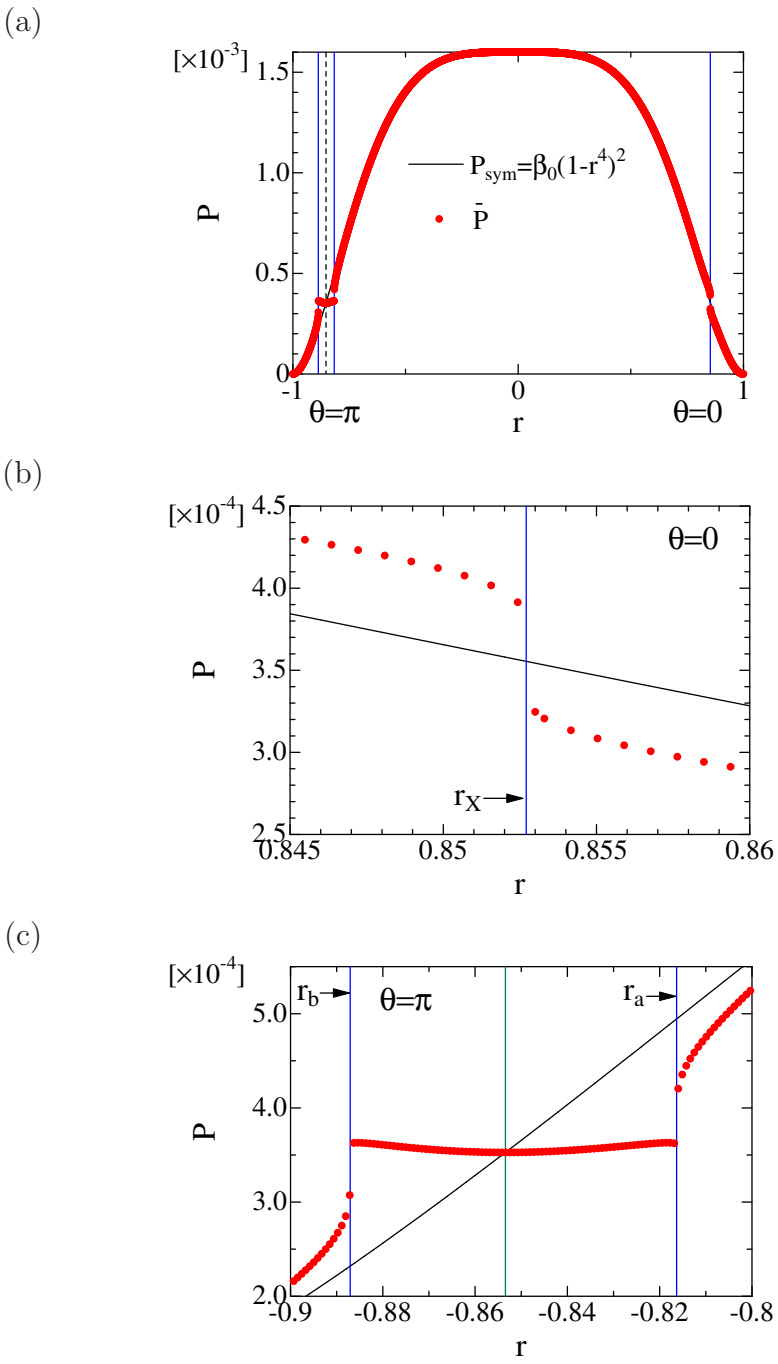

Figure 4.12: Profile of the averaged pressure along the field line (a) along the line connecting $(r = 1, \theta = 0, z = 0)$ and $(r = 1, \theta = \pi, z = 0)$ and its enlargements at (b) $\theta = 0$ and (c) $\theta = \pi$ for $\Psi_b = 1.0 \times 10^{-3}$ and $\beta_0 = 0.16\%$. Red dots and black line show the averaged pressure $\bar{P}$ and P_{sym}, respectively. Vertical blue lines show the positions of the separatrix of the magnetic island. Vertical green line shows the position of the O-point. Here, r_X, r_a and r_b are the radial coordinate of the X-point, the radial coordinates of the inside and outside of the separatrix at $\theta = \pi$, respectively.

4.4.2 Calculation procedure with field line tracing method

In Section 4.3, we obtain an MHD equilibrium consistent with a static island by utilizing a diffusion equation parallel to the field line for the pressure calculation. In this case, the resultant equilibrium pressure profile is flat at both the O-point and the X-point of the magnetic island. The equilibrium is useful for the study of the effect of the local annual flat structure of the pressure profile on the stability of the interchange mode, but not for the pressure profile which is steep at the X-point and flat at the O-point. Thus, we develop a numerical scheme to calculate equilibria with such pressure profile in this Section.

We solve Eqs.(4.1) and (4.2) in two separate steps as in Section 4.3. However, we develop a different method for each steps. In the first step, where Eq.(4.1) is solved for P with Ψ fixed, a field line tracing method is employed. We trace a field line from the initial point of (r_0, θ_0, z_0) and set the pressure as $P(r, \theta, z) = P_{sym}(r_0)$ along the field line to make the pressure constant. Here, $P_{sym}(r)$ is the pressure profile corresponding to the nested magnetic surfaces without magnetic islands. We fix θ_0 as $\theta_0 = \theta_X$ which is the azimuthal angle of the position of the X-point for given z_0. By changing r_0, we can trace every field line outside the separatrix. The pressure inside the separatrix of the island is set to the constant value of $P_{sym}(r_X)$.

In the second step, where Eq.(4.2) is solved for Ψ with P fixed, a relaxation process is utilized, which solves the following equations:

$$\frac{\partial \tilde{\Psi}}{\partial t} = -\mathbf{B} \cdot \nabla \tilde{\Phi} + \frac{1}{S} \tilde{J}_z, \tag{4.38}$$

$$\frac{\partial \tilde{U}}{\partial t} = -\mathbf{B} \cdot \nabla \tilde{J}_z + \frac{1}{2\epsilon^2} \nabla \Omega \times \nabla P \cdot \mathbf{z} + \nu \nabla_\perp^2 \tilde{U}. \tag{4.39}$$

We regard the steady state as the equilibrium state as in Ref. [19]. To accelerate the relaxation process, we drop the convection term in Eq.(2.2). In order to judge the achievement of the steady state, we observe the growth rates of the kinetic energy E_K and the magnetic energy E_M given by

$$\gamma_K = \frac{1}{E_K} \frac{dE_K}{dt} \quad and \quad \gamma_M = \frac{1}{E_M} \frac{dE_M}{dt}, \tag{4.40}$$

respectively, where

$$E_K = \frac{1}{2} \int |\nabla \tilde{\Phi} \times \mathbf{z}|^2 dV \; and \; E_M = \frac{1}{2} \int |\mathbf{z} \times \nabla \tilde{\Psi}|^2 dV. \tag{4.41}$$

When the conditions of

$$|\gamma_K| < \epsilon_\gamma \quad and \quad |\gamma_M| < \epsilon_\gamma, \tag{4.42}$$

are satisfied simultaneously, we judge that the steady state is achieved. Since we introduce a small value of $1/S$ for the numerical stability in Eq.(4.38) of this step, we also check the force balance condition of Eq.(4.2) by evaluating ΔF_N defined as

$$\Delta F_N = \frac{|F_B + F_P|}{|F_B| + |F_P|}, \tag{4.43}$$

where the subscript of N denotes the number of iteration. Here, F_B and F_P are given by

$$F_B = \int (-\mathbf{B} \cdot \nabla \tilde{J}_z) dV \; and \; F_P = \int \Big(\frac{1}{2\epsilon^2} \nabla\Omega \times \nabla P \cdot \mathbf{z} \Big) dV, \tag{4.44}$$

respectively.

As in Section 4.3, the two steps described above are iterated until the condition of Eq.(4.25) is satisfied.

4.4.3 Resultant equilibrium

We employ the magnetic configuration parameters of $N_t = 10$ and $l = 2$, which correspond to the LHD configuration. We vary the value of Ψ_b from 0 to $+1.0 \times 10^{-3}$. In the case of positive Ψ_b, the X-point is located at $\theta_X = 0$ and $z = 0$. Hence, we set the initial point of the field line tracing as $\theta_0 = 0$ and $z_0 = 0$ in the first step. The pressure profile $P_{sym}(r)$ in Eq.(4.31) is used, and the central beta value of $\beta_0 = 1.5\%$ is employed. Since we use $P_{sym}(r)$ of Eq.(4.31) as the pressure at the initial point (r_0, θ_0, z_0) at each iteration, the profile at (r, θ_0, z_0) for any r, and therefore, the gradient at the X-point is fixed over the whole iterations. In the second step, dispassion parameters are set to be $S = 10^2$ and $\nu = 10^{-6}$. We employ $\epsilon_\gamma = 10^{-6}$ and $\epsilon_w = 10^{-4}$ as the convergence parameters.

Figure 4.13 shows the resultant equilibrium pressure for $\Psi_b = 1.0 \times 10^{-3}$. We can obtain an equilibrium pressure profile which is steep at the X-point and flat at the O-point with the present scheme. Figure 4.14 shows the variations of ΔF_N, δw_N and w_N in the iterations for several Ψ_b's. In the final states, $\Delta F_N < 10^{-2}$ is satisfied as shown in Fig.4.14 (a), which indicates that the equilibrium is obtained in a good accuracy. Figure 4.14 (b) shows that the island width is converged in the finite number of iteration for each Ψ_b. The converged equilibrium island width is larger than the vacuum width w_0 as shown in Fig.4.14 (c). The contour of the constant pressure coincides with the

magnetic surfaces as shown in Fig.4.15. That is, the equilibrium pressure has the same structure as that of the island. Figure 4.16 shows the dependence of the island width on Ψ_b. The island width is increased by the finite beta. The increment is increased with Ψ_b.

4.5 Discussions

The equilibrium pressure profile obtained in Section 4.4 is steep at the X-point and flat at the O-point as shown in Fig.4.13. On the other hand, the equilibrium pressure profile obtained in Section 4.3 is flat at not only the O-point but also the X-point as shown in Fig.4.7. The difference in the pressure gradient at the X-point is attributed to the continuity of the pressure gradient across the separatrix except the X-point. The pressure gradient in Fig.4.13 is discontinuous across the separatrix which is obtained with the field line tracing method explained in Section 4.4. This discontinuity is inevitable for the existence of the finite gradient at the X-point. In Section 4.3, in order to obtain the pressure satisfying Eq.(4.1), we calculate the steady state of Eq.(4.11). In the right hand side of Eq.(4.11), the derivatives in r and θ directions are included. The continuity of the derivatives are naturally guaranteed in the numerical calculation. Therefore, the pressure gradient is continuous even at the separatrix. This continuity makes the profile at the X-point flat.

The situation that the continuous pressure gradient across the separatrix leads to the flat structure at the X-point can be confirmed also with the field line tracing scheme. We start the field line tracing from the initial point of $(r_0, \theta_0 = \pi, z_0 = 0)$ instead of $(r_0, \theta_0 = 0, z_0 = 0)$ used in the calculation for the pressure profile with steep gradient at the X-point. We assume $P_{sym}(r)$ which is plotted with the purple solid line in the region of $-1 \leq r \leq 0$ at $\theta = \pi$ in Fig.4.17 instead of Eq.(4.31). Here, P_{sym} is defined as

$$P_{sym}(r) = \beta_0 \left\{ \frac{1-(1-r_s^4)^2}{r_a^8}(r_a^4 - r^4)^2 + (1-r_s^4)^2 \right\} \quad (0 \leq r \leq r_a), \tag{4.45}$$

$$P_{sym}(r) = \beta_0 (1-r_s^4)^2 \quad (r_a < r < r_b), \tag{4.46}$$

$$P_{sym}(r) = \beta_0 \frac{(1-r_s^4)^2}{(1-r_b)^4} \left\{ (1-r_b)^2 - (r-r_b)^2 \right\}^2 \quad (r_b \leq r \leq 1), \tag{4.47}$$

where $\beta_0 = 1.5\%$ is employed. The gradient of this profile is continuous at the separatrix. In this case, we obtain the profile plotted with the red solid line in the region

of $0 \leq r \leq 1$ at $\theta = 0$ in Fig.4.17 as the result of the field line tracing method. This result shows that the gradient at the X-point is zero for the continuous gradient at the separatrix. This result also means that the present field line tracing method can generate the equilibrium solutions with which the pressure profile is flat at the X-point as well.

4.6 Summary

To study the effect of the (m, n)=(1,1) static island on the interchange mode, the equilibrium code, FLEC, is developed. An MHD equilibrium including a static magnetic island for the reduced MHD equations is obtained in a straight heliotron configuration by means of the code. The equilibrium equations to be solved are the coupled equations for the poloidal flux and the pressure. The equations are solved by iterating two numerical steps. In the first step, the equation of $\mathbf{B} \cdot \nabla P = 0$ is solved with the poloidal flux fixed so that the pressure constant along the field line is obtained. In the second step, the force balance equation for the poloidal flux, which is derived from the vorticity equation, is solved with the pressure fixed. The equations are solved by iterating two numerical steps.

We have developed two kinds of numerical scheme to solve the equilibrium equations. In one scheme, we employ the Fourier series in the formulation. A diffusion equation parallel to the field line and an ordinary equation are utilized for the first step and the second steps, respectively. In the first step, the steady state solution of the diffusion equation corresponds to the pressure constant along the field line. Three Fourier components of $\hat{P}_{0,0}, \hat{P}_{1,1}$ and $\hat{P}_{2,2}$ are necessary at least to obtain the steady state. In the final equilibrium pressure, $\hat{P}_{2,2}$ is negligibly small compared with other components at $\beta_0 = 0.16\%$, and therefore, it is not necessary in the second step. Nevertheless, $\hat{P}_{2,2}$ is needed for the sufficient steady state solution in the first step. In the second step, the force balance equation for the poloidal flux, which is derived from the vorticity equation, is solved with the pressure fixed. Since $\hat{P}_{2,2}$ and higher pressure components can be neglected, the Fourier series of the equation is truncated up to $n = 1$. In this case, the condition of $\tilde{\Psi}_{1,1} = 0$ and an ordinary differential equation for $\tilde{\Psi}_{0,0}$ are derived from the force balance equation. Therefore, only $\tilde{\Psi}_{0,0}$ is updated with the solution of the ordinary equation in the second step.

In the resultant equilibrium, we obtain a pressure profile which corresponds to the island structure. A separatrix is seen also in the pressure contour plot, however, the

pressure gradient is zero at the O-point and the X-point. Therefore, local flattening appears at not only the O-point but also the X-point. The equilibrium depends on the symmetry part of the pressure and the poloidal flux, P_{sym} and Ψ_{sym}, which are used as the initial condition, even if the magnetic field is almost vacuum one.

It is noted that this scheme of the second step cannot be applied to higher beta cases as it is. At the low beta case such as $\beta_0 = 0.16\%$, we obtain a satisfying accuracy in the calculation with only a small number of the Fourier series for $\tilde{\Psi}$ and $\tilde{P}$. This is attributed to the fact that the solution of the magnetic field is close to the vacuum field. At higher beta, the deviation of the magnetic island shape from the vacuum one is enhanced, which degrades the accuracy of the approximation with the small number of the Fourier modes. Therefore, higher components are necessary in the second step for keeping the accuracy. In this case, the force balance equation becomes coupled equations for multiple number of $\tilde{\Psi}_{n,n}$, not a single ordinary differential equation.

It is also obtained with this scheme that the pressure gradient is enhanced at the X-point as the perpendicular diffusion coefficient increases. A pressure profile flattened only at the O-point not the X-point can be obtained for a sufficiently large coefficient. The pressure at the axis is also affected by the perpendicular diffusion so as to be decreased through the change in the radial profile of $\tilde{P}_{0,0}$. The present result is obtained under the assumption of no flow steady state with a special type of heat source. Precise analysis with more realistic flow and heat source remains as a future work.

In the other scheme, a field line tracing method and a relaxation method are utilized for the first and the second steps, respectively, for the solution with the pressure profile with a finite gradient at the X-point. In the first step, we calculate the pressure along a field line by replacing with a fixed value at a given azimuthal angle. By setting the azimuthal angle as that including the X-point, θ_X, we obtain an equilibrium with a finite pressure gradient at the X-point. Therefore, this scheme guarantees the finite pressure gradient at the X-point. The resultant equilibrium shows that the island width is increased by the finite beta value.

We conclude from the results of the two schemes that there exist two kinds of equilibrium solutions depending on the gradient at the X-point, finite or zero. The difference of the equilibria is related to the continuity of the pressure gradient at the separatrix of the island except the X-point. The gradient at the X-point can be finite in the case where a discontinuous pressure gradient is allowed, while the gradient at the X-point must be zero in the case where only a continuous pressure gradient is allowed. In the former case, the solution is determined uniquely if the radial pressure

profile at $\theta = \theta_X$ is specified. Since the pressure gradient is discontinuous at the separatrix, the second derivative of the radial pressure profile is infinite. On the other hand, in the latter case, the second derivative is finite. By rounding the radial pressure profile at the separatrix in the former solution or giving a finite second derivative to the former profile, we can obtain the latter solution. In this case, there exist various solutions depending on the shape of the roundness or the value of the second derivative. Therefore, the former solution can be considered as a special case of the latter case and the two solutions may be considered as a bifurcation. In the scheme of the field line tracing and the relaxation, it is assumed that the pressure is flat inside the separatrix in the present scheme. If a pressure profile corresponding to the magnetic surfaces inside the separatrix is incorporated, the freedom of the solution is increased.

It is interesting to obtain an equilibrium with a stochastic magnetic field by multi-helicity islands. However, the scheme developed here cannot be applied to the calculation of the equilibrium including a stochastic region. In the scheme of the parallel diffusion and the ordinary equation, a lot of Fourier mode are required for the expression of the stochastic region. Therefore, the scheme should be significantly modified so that such many modes can be treated. In the scheme of the field line tracing and the relaxation, we fix a radial pressure profile at a given azimuthal position so that the solution should have the profile at the position. This treatment is possible only for the cases with radially separated islands. In the stochastic case, it is impossible to predict the pressure profile to be fixed at any azimuthal position before the calculation.

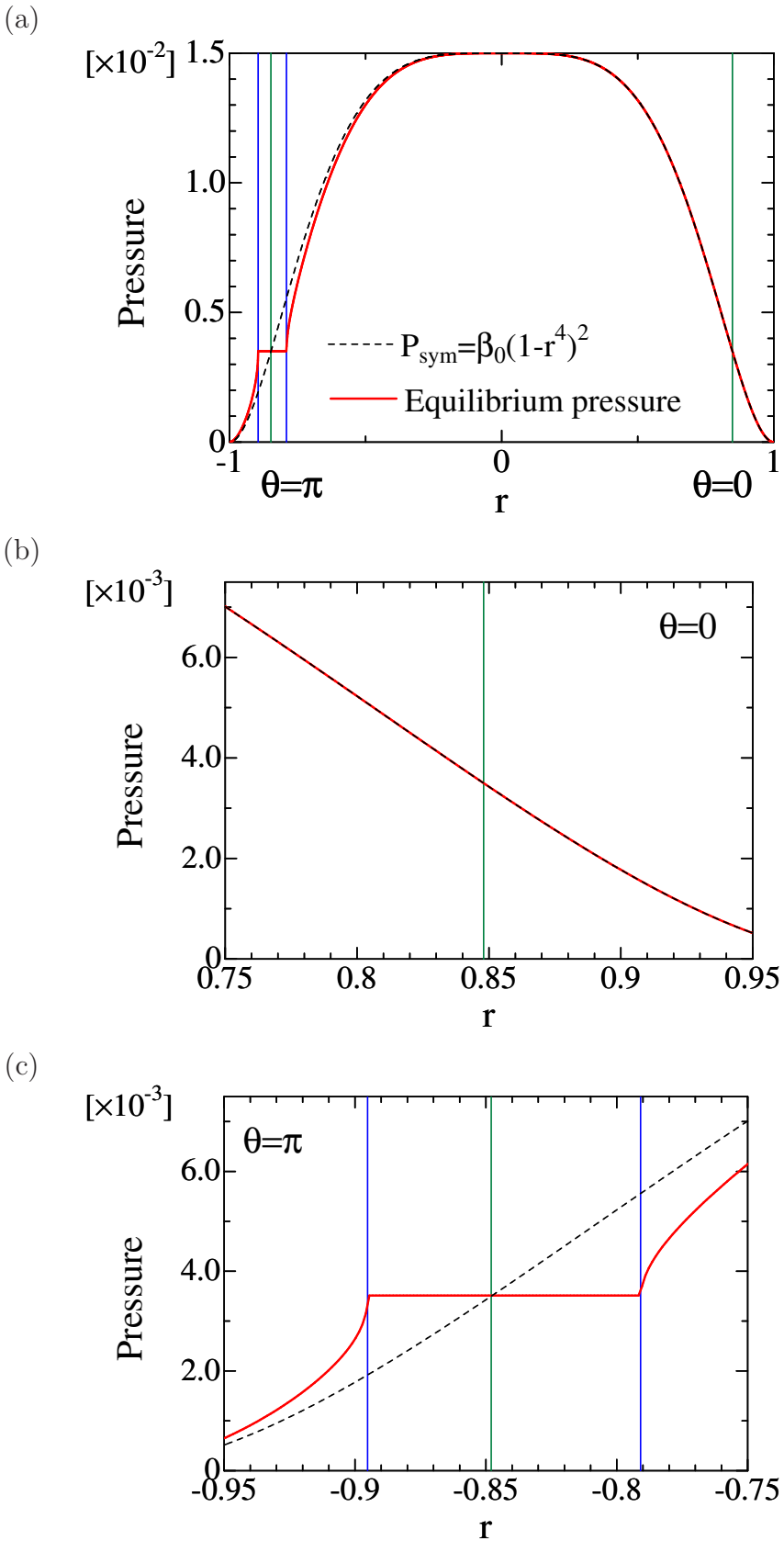

Figure 4.13: Equilibrium pressure profile (a) along the line connecting $(r = 1, \theta = 0, z = 0)$ and $(r = 1, \theta = \pi, z = 0)$ and its enlargements at (b) $\theta = 0$ and (c) $\theta = \pi$ for $\Psi_b = 1.0 \times 10^{-3}$ and $\beta_0 = 1.5\%$. Blue lines indicate the position of the separatrix of the island at $\theta = \pi$. Green lines indicate the position of the rational surface.

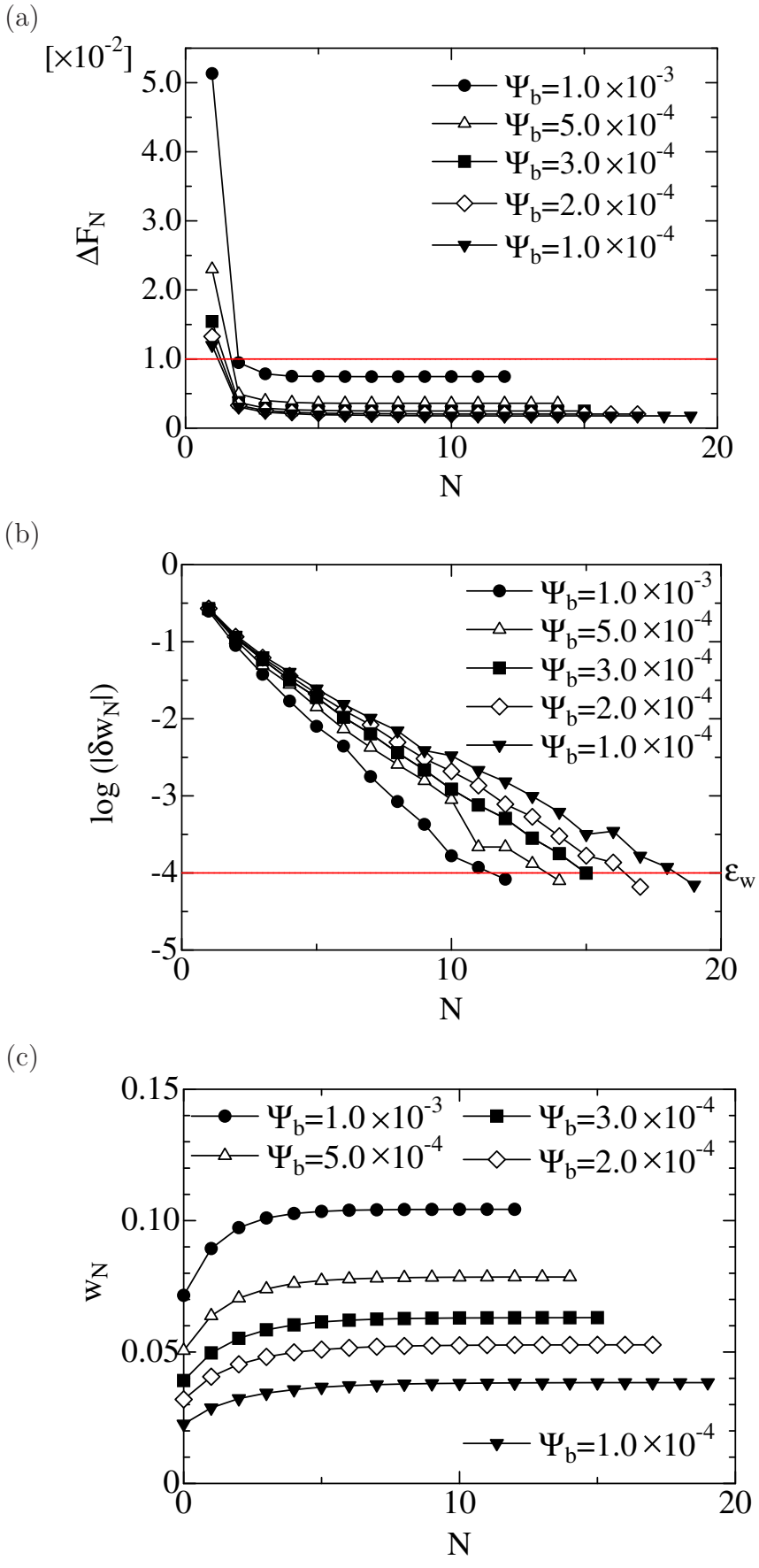

Figure 4.14: Variation of (a) ΔF_N, (b) δw_N and (c) w_N for the number of iteration N.

(a)

(b)

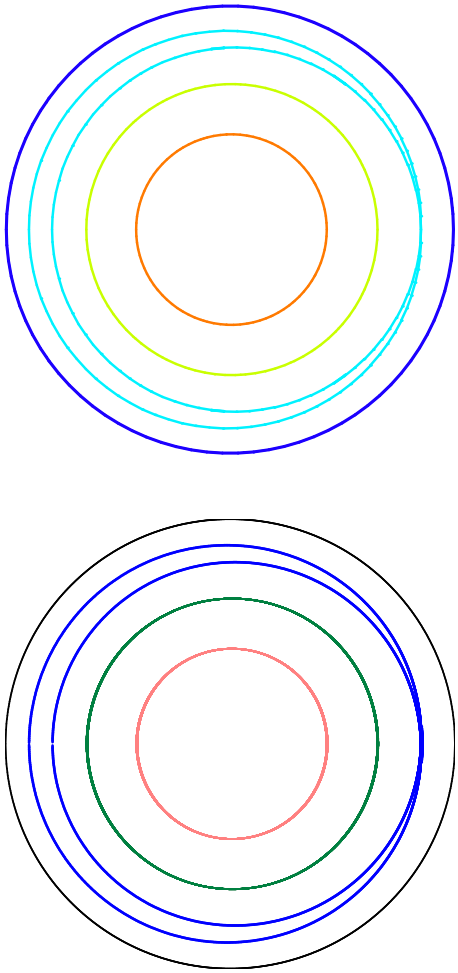

Figure 4.15: Plots of (a) contour of constant pressure and (b) magnetic surfaces for $\Psi_b = 10^{-3}$ and $\beta_0 = 1.5\%$. The island width is 1.04×10^{-1}.

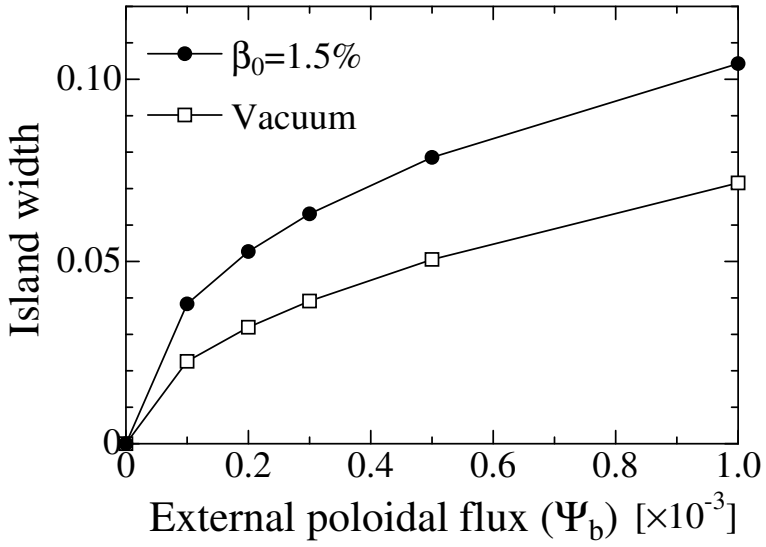

Figure 4.16: Dependence of equilibrium island width on Ψ_b.

(a)

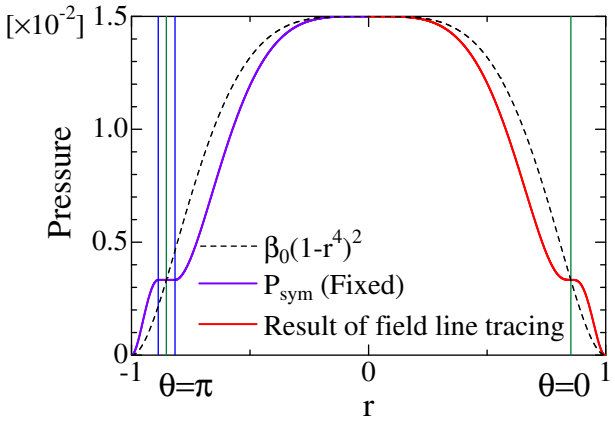

(b)

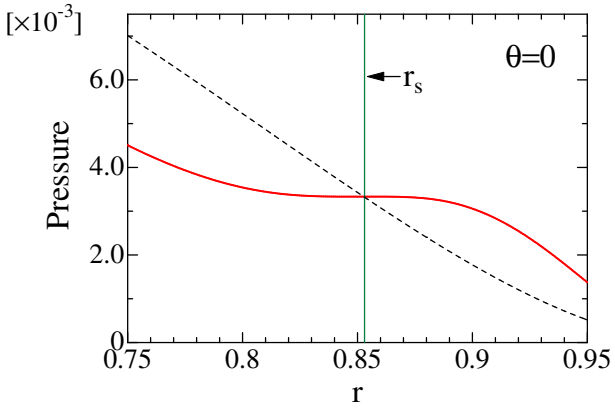

(c)

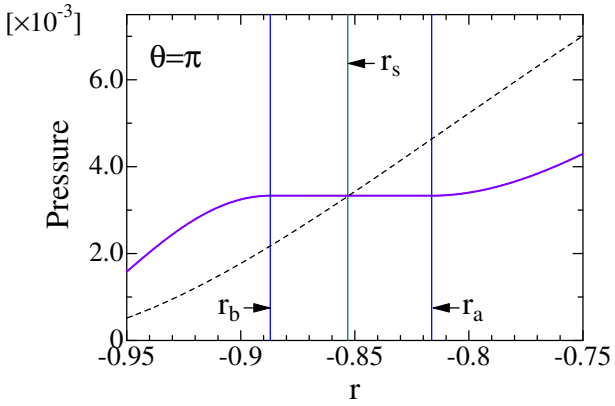

Figure 4.17: Pressure profile (a) along the line connecting $(r = 1, \theta = 0, z = 0)$ and $(r = 1, \theta = \pi, z = 0)$ and its enlargements at (b) $\theta = 0$ and (c) $\theta = \pi$ for $\Psi_b = 1.0 \times 10^{-3}$ and $\beta_0 = 1.5\%$. Purple and red lines show the assumed profile of $P(r_0, \theta_0 = \pi, z_0 = 0)$ with continuous gradient at the separatrix and the profile obtained by the tracing field lines starting from $(r_0, \theta_0 = \pi, z_0 = 0)$, respectively. Blue lines indicate the position of separatrix of island at $\theta = \pi$. Green lines indicate the position of the rational surface.

Chapter 5

Stability of Interchange Modes in Equilibrium including Static Island

5.1 Introduction

In this Chapter, the effect of the static island with the mode number (m, n)=(1,1) on the interchange mode with same mode number is studied. For this study, the equilibria with the pressure consistent with static magnetic islands obtained in Chapter 4 are utilized.

In Chapter 4, two kinds of solutions are obtained. One is the solution with a locally flat pressure profile at the X-point and the other is the solution with a finite pressure gradient at the X-point. In the former case, the flat structure in the pressure profile is almost annular around the separatrix. Ichiguchi et al. [22,23] numerically examined the linear stability of the ideal interchange mode for the equilibria with locally flat pressure profiles in such annular region around the resonant surface. They showed that the local flat structure reduces the growth rate of the mode and the mode is stabilized where the radial width of the flat structure is beyond a quarter of the half-width of the stream function obtained for the equilibrium pressure profile without local flat structure. Thus, we study whether the interchange mode can be stabilized by the local flat structure of the pressure profile even in the case where the finite gradient is kept at the X-point. For this study, we employ the equilibria obtained with the scheme of the field line tracing and the relaxation in Chapter 4. We examine the dependence of the linear growth rate and the nonlinear saturation level on the island width by utilizing the NORM code [9]. The island structure can be also affected by the nonlinear evolution of the interchange

mode as in the case of Chapter 3. Therefore, we also study the change of the island width and the phase.

This Chapter is organized as follows. In Section 5.2, the island effect on the linear stability is showed. We show that the interchange mode can be stabilized for the equilibrium with substantial island width. In Section 5.3, the nonlinear interaction between static islands and interchange modes is discussed. We show that the island width is increased or decreased by the nonlinear saturation of the interchange modes as in the case of Chapter 3. Summary is given in Section 5.4.

5.2 Island effect on linear stability

The effect of the static island on the interchange mode is studied by using the equilibrium obtained in Chapter 4. For this purpose, the reduced MHD equations in the expression of

$$\frac{\partial \tilde{\Psi}}{\partial t} = -\mathbf{B}_{eq} \cdot \nabla \tilde{\Phi} - \tilde{\mathbf{B}} \cdot \nabla \tilde{\Phi} + \frac{1}{S} \tilde{J}_z, \tag{5.1}$$

$$\frac{d\tilde{U}}{dt} = -\mathbf{B}_{eq} \cdot \nabla \tilde{J}z - \tilde{\mathbf{B}} \cdot \nabla (Jz_{eq} + \tilde{J}z) + \frac{1}{2\epsilon^2} \nabla\Omega \times \nabla \tilde{P} \cdot \mathbf{z} + \nu \nabla_\perp^2 \tilde{U} \tag{5.2}$$

and

$$\frac{d\tilde{P}}{dt} = \mathbf{z} \times \nabla \tilde{\Phi} \cdot \nabla P_{eq} + \kappa_\perp \nabla_\perp^2 \tilde{P} + \kappa_\parallel \{ (\mathbf{B}_{eq} \cdot \nabla)(\mathbf{B}_{eq} \cdot \nabla) \tilde{P} \tag{5.3}$$

$$+ (\mathbf{B}_{eq} \cdot \nabla)(\tilde{\mathbf{B}} \cdot \nabla)(P_{eq} + \tilde{P}) + (\tilde{\mathbf{B}} \cdot \nabla)(\mathbf{B}_{eq} \cdot \nabla) \tilde{P} + (\tilde{\mathbf{B}} \cdot \nabla)(\tilde{\mathbf{B}} \cdot \nabla)(P_{eq} + \tilde{P}) \}$$

are employed. In this Chapter, equilibrium quantities have the dependence of not only r but also θ and z. We express the equilibrium quantities with the Fourier series as follows:

$$\Psi_{eq}(r,\theta,z) = \Psi_{sym}(r) + \Psi^{ext}_{1,1}(r,\theta,z) + \Psi^J(r,\theta,z),\ \Psi^J(r,\theta,z) = \sum_{n=0,m=n}^{N_{eq}} \hat{\Psi}^J_{m,n}(r) \cos(m\theta - nz) \tag{5.4}$$

$$P_{eq}(r,\theta,z) = P_{sym}(r) + P^J(r,\theta,z),\ P^J(r,\theta,z) = \sum_{n=0,m=n}^{N_{eq}} \hat{P}^J_{m,n}(r) \cos(m\theta - nz), \tag{5.5}$$

where the superscript of "J" refers the variation of the equilibrium quantity due to the static island. Here, Ψ^J corresponds to $\tilde{\Psi}$ in Eq.(4.4). For the maximum number of Fourier series $N_{eq} = 15$ is used. As in previous Chapter 4, the same parameters of $N_t = 10$, $l = 2$ and $\beta_0 = 1.5\%$ are employed. Since $\mathbf{B}_{eq}$ and P_{eq} satisfy

$$\mathbf{B}_{eq} \cdot \nabla P_{eq} = 0, \tag{5.6}$$

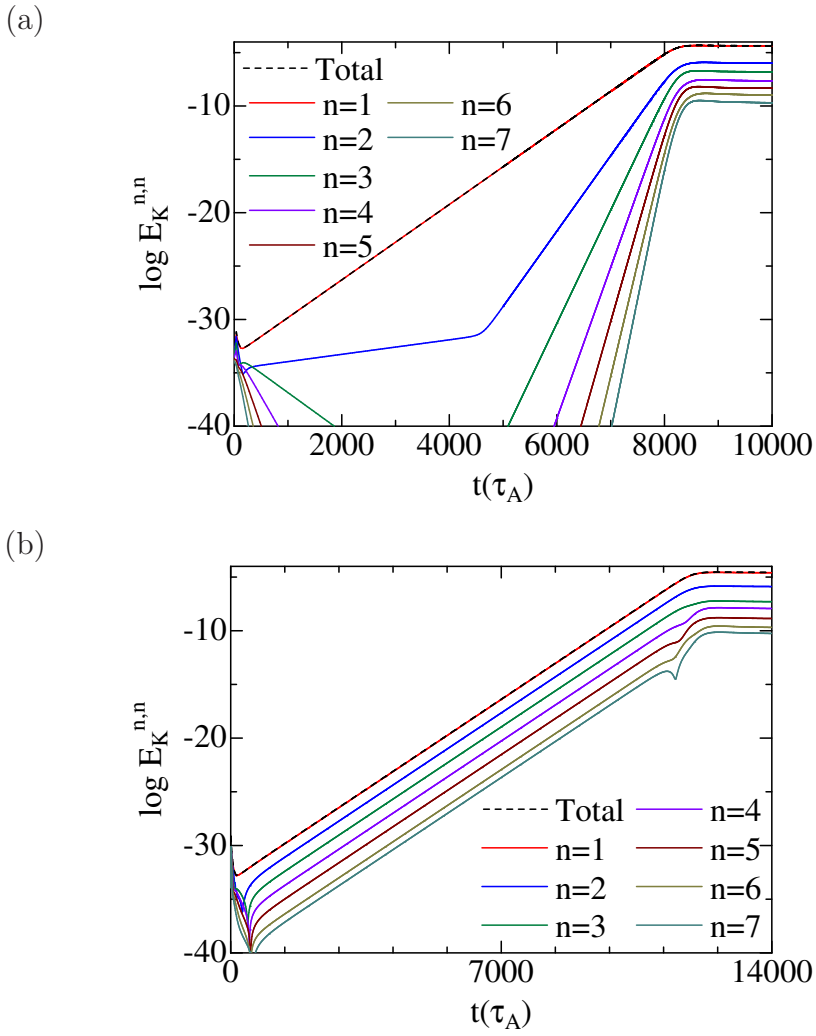

Figure 5.1: Time evolutions of kinetic energy for (a) $w_i = 0$ ($\Psi_b = 0$) and $\sigma = +1$ and (b) $w_i = +2.8 \times 10^{-2}$ ($\Psi_b = +5.0 \times 10^{-5}$) and $\sigma = +1$.

where $\mathbf{B}_{eq}$ is given by Eq.(2.13), the parallel diffusion term Q given by Eq.(3.21) becomes

$$Q = \kappa_{\parallel}\{(\mathbf{B}_{eq} + \tilde{\mathbf{B}}) \cdot \nabla\}(\tilde{\mathbf{B}} \cdot \nabla)P_{eq}. \tag{5.7}$$

Therefore, Q does not give any initial perturbations even in the case $\Psi_b \neq 0$ if $\tilde{\mathbf{B}} = 0$. Therefore, we provide an initial condition given by Eq.(2.19) for the present analysis. The dissipation parameters

$$S = 10^4, \nu = 8.5 \times 10^{-6}, \kappa_{\perp} = 2.0 \times 10^{-5}, \kappa_{\parallel} = 2.0 \tag{5.8}$$

are used so that (m, n)=(1,1) component is dominant.

Figure 5.1 shows the time evolutions of the kinetic energy for (a) $w_i = 0$ ($\Psi_b = 0$) and $\sigma = +1$ and (b) $w_i = +2.8 \times 10^{-2}$ ($\Psi_b = +5.0 \times 10^{-5}$) and $\sigma = +1$, where w_i

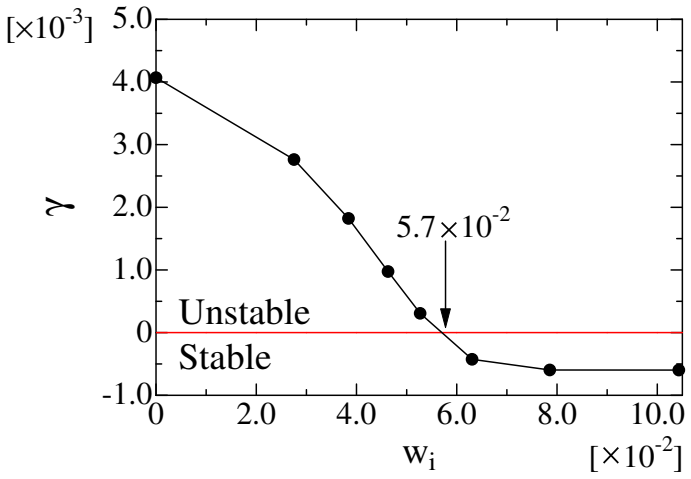

Figure 5.2: Dependence of γ in the linear region on w_i.

indicates the island width at $t = 0$ as in Chapter 3. The linear phase is obtained and the $(m, n) = (1, 1)$ component is dominant in the whole region for the both cases. There exists the difference feature between the cases of $w_i = 0$ and $w_i = +2.8 \times 10^{-2}$ in the linear growth rates of $E_K^{n,n}$. The growth rate of each component is almost the same in the case of $w_i = +2.8 \times 10^{-2}$. This feature is common for the cases of $w_i \neq 0$. This is attributed to the fact that the component of $(m, n) = (1, 1)$ is dominant and the relation of $|\hat{\Psi}^J_{1,1}| >> |\hat{\Psi}_{1,1}|$ is satisfied in the linear region, as discussed in Section 3.2.3. The steady state appears after the linear growth in these cases.

Figure 5.2 shows the dependence of γ in the linear region on w_i, where γ is given by Eq.(2.23). As w_i is increased, γ is decreased. The linear growth rate is independent of σ. We find that there exists the stabilization effect as well as Ref. [22,23] in spite of the existence of the steep pressure gradient at the X-point shown in Fig.4.13. Figure 5.2 also shows a marginally stable island width, which is $|w_i| = 5.7 \times 10^{-2}$ ($|\Psi_b| = 2.3 \times 10^{-4}$). Beyond the width, the mode is completely stabilized. Figure 5.3 shows the profiles of the normalized $\hat{\Phi}_{1,1}$ for $w_i = 0$ ($\Psi_b = 0$) and $w_i = +4.6 \times 10^{-2}$ ($\Psi_b = +1.5 \times 10^{-4}$). The sign of the eigenfunctions change depending on σ as in the case of Fig.3.3. The half-width of the stream function, w_H, is 6.5×10^{-2} for $w_i = 0$ ($\Psi_b = 0$) and 6.6×10^{-2} for $w_i = +4.6 \times 10^{-2}$ ($\Psi_b = +1.5 \times 10^{-4}$). Here, w_H is normalized by the plasma radius. Here, we define the relative change of w_H

$$\delta w_H = \frac{|w_H(w_i) - w_H(w_i = 0)|}{w_H(w_i = 0)}. \tag{5.9}$$

The value of δw_H is $1.5 \times 10^{-2} << 1$ for $w_i = +4.6 \times 10^{-2}$ ($\Psi_b = +1.5 \times 10^{-2}$), which means w_H is almost independent of w_i. We find that the interchange mode can be

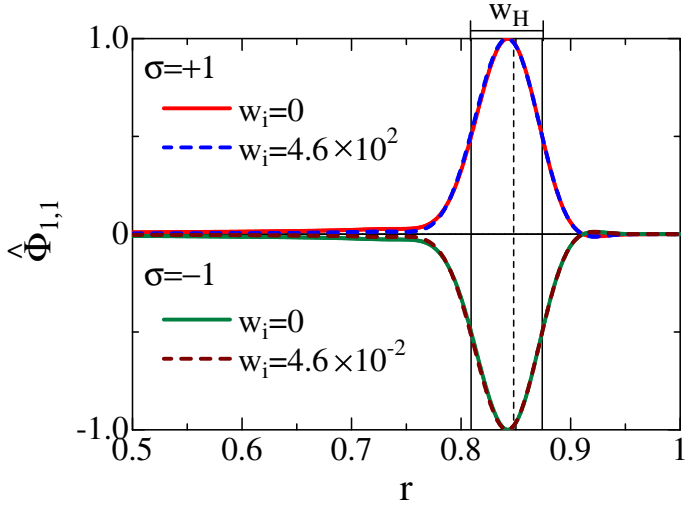

Figure 5.3: Normalized $\hat{\Phi}_{1,1}$ for $w_i = 0$ ($\Psi_b = 0$) and $w_i = +4.6 \times 10^{-2}$ ($\Psi_b = +1.5 \times 10^{-4}$). Vertical dashed line shows the position of rational surface. The half-width w_H is 6.5×10^{-2} for $\Psi_b = 0$. Vertical black solid lines indicate the position of half value of the normalized $\hat{\Phi}_{1,1}$ for $\Psi_b = 0$.

stabilized with $w_i \geq 0.88 w_H$ ($w_i = 0$). Compared with the annual fattening case, the marginal width is much broader than that of Ref. [22, 23].

5.3 Nonlinear interaction between static magnetic islands and interchange modes

As shown in Fig.5.1, the steady state appears after linear growth when the interchange modes are unstable. The island structure and the pressure profile are changed by nonlinear saturation of the interchange modes. In this Section, we discuss the property of the changes.

Figure 5.4 (a) shows the dependence of the saturation level of the kinetic energy E_K on w_i evaluated in the steady state where the condition of $|\gamma| < 10^{-5}$ is satisfied. In the increase of w_i, E_K is decreased. This dependence is similar to that of the linear growth rate as shown in Fig.5.2. Figure 5.4 (b) shows the profile of $\hat{\Phi}_{1,1}$ in the steady state. As w_i is increased, the absolute value of $\hat{\Phi}_{1,1}$ is decreased. Figure 5.4 (c) shows the dependence of δw_H in the steady state on w_i. Even in the steady state, $\delta w_H(w_i = 0)$ is $3.0 \times 10^{-2} << 1$, and therefore, the half-width is almost independent of w_i. Thus, the decrease of E_K in the steady state is attributed to the decrease of the absolute value

of $\hat{\Phi}_{1,1}$.

We evaluate the island width in the steady state. Figure 5.5 shows the dependence of the island width on Ψ_b. The sign of the island width indicates the phase of the island as shown in Figs.3.9 and 3.23. The diamonds show the island width in vacuum. Blue circles show w_i in the equilibrium. Blue squares show the marginal island width ($|w_i| = 5.7 \times 10^{-2}$). Red circles and green triangles show the island width in the steady state w_s for $\sigma = +1$ and $\sigma = -1$, respectively. In the region $|w_i| \geq 5.7 \times 10^{-2}$, the island width does not change because the interchange modes are stable. In the region $|w_i| < 5.7 \times 10^{-2}$, there are two cases of the change depending on σ. One is the increase of the island width and the other is the decrease of the width as in the case of Fig.3.9.

The island width and the pressure profile are changed by the nonlinear saturation. We see the changes for $w_i = 0$ ($\Psi_b = 0$) at first. Figure 5.6 (a) shows magnetic surfaces for $w_i = 0$ ($\Psi_b = 0$) and $\sigma = +1$ at $t = 10000\tau_A$. In this case, two O-points appear in the magnetic surfaces. One is the O-point located at $\theta = \pi$ shown by the blue line. The other is the O-point located at $\theta = 0$ shown by the green line. This is a mixed structure of the $m = 1$ and the $m = 2$ islands. However, the island width with the O-point located at $\theta = \pi$ is $+5.2 \times 10^{-2}$ and the other is -5.8×10^{-3}. Since the ratio is 0.11, the $m = 1$ island is dominant. The flow pattern of the vortices calculated from $\tilde{\Phi}$ at $t = 10000\tau_A$ is plotted in Fig.5.6 (b). The radial flow at $\theta = 0$ and $\theta = \pi$ is weak but finite. In the case of $\sigma = -1$, the phase of the magnetic surfaces is opposite and the direction of the flow is reversed. Figure 5.7 shows the pressure profile along the line connecting the points of $(r = 1, \theta = 0, z = 0)$ and $(r = 1, \theta = \pi, z = 0)$ at $t = 0$ and $t = 10000\tau_A$ for $w_i = 0$ ($\Psi_b = 0$) and $\sigma = \pm 1$. The deformation by the $m = 1$ interchange mode is observed around the resonant surface with $\iota = 1$. This deformation is generated by the convection of the radial flow. The equilibrium pressure inside rational surface is higher than that outside rational surface. The flow direction is radially outward at $\theta = 0$ and inward at $\theta = \pi$ for $\sigma = +1$ as shown in Fig.5.6 (b). Therefore, the plasma with the higher pressure inside the rational surface is carried to outside of the rational surface at $\theta = 0$ and the plasma with the lower pressure outside the rational surface is carried to inside at $\theta = \pi$ for $\sigma = +1$. As a result, the pressure is increased at $\theta = 0$ and decreased at $\theta = \pi$ for $\sigma = +1$. This mechanism is the same for $\sigma = -1$.

Next, we examine the case of $w_i \neq 0$ ($\Psi_b \neq 0$). Figure 5.8 (a) and (b) show magnetic surfaces for $w_i = +2.8 \times 10^{-2}$ ($\Psi_b = +5.0 \times 10^{-5}$) and $\sigma = +1$ at $t = 0$ and $t = 14000\tau_A$, respectively. In the time evolution, the island width of the (m, n)=(1,1)

island is increased and the small island with the O-point located at $\theta = 0$ is generated by corresponding to the $(m, n) = (2, 2)$ island. Figure 5.8 (c) shows the flow pattern for $w_i = +2.8 \times 10^{-2}$ ($\Psi_b = +5.0 \times 10^{-5}$) and $\sigma = +1$ at $t = 14000\tau_A$. The flow direction is radially outward at the X-point and inward at the O-point of the initial static island. Figure 5.9 (a) and (b) show magnetic surfaces for $w_i = +2.8 \times 10^{-2}$ ($\Psi_b = +5.0 \times 10^{-5}$) and $\sigma = -1$ at $t = 0$ and $t = 14000\tau_A$, respectively. Figure 5.9 (c) shows the flow pattern for $w_i = +2.8 \times 10^{-2}$ ($\Psi_b = +5.0 \times 10^{-5}$) and $\sigma = -1$ at $t = 14000\tau_A$. In this case of the time evolution, the width of the (m, n)=(1,1) island is decreased and the phase of the island is changed so that the O-point is located at $\theta = 0$. The flow direction is radially inward at the X-point and outward at the O-point of the initial static island. The island width increases when the flow direction is radially outward at the X-point of the initial static island and the island width decrease when the flow direction is radially inward at the X-point. Therefore, the mechanism of the change of the island is the same as that in Chapter 3.

Figure 5.10 shows the variation of the pressure profile along the line connecting the points of $(r = 1, \theta = 0, z = 0)$ and $(r = 1, \theta = \pi, z = 0)$ between $t = 0$ and $t = 14000\tau_A$ for $w_i = +2.8 \times 10^{-2}$ ($\Psi_b = +5.0 \times 10^{-5}$) and $\sigma = \pm 1$. The pressure is increased at $\theta = 0$ and decreased at $\theta = \pi$ at the rational surface for $\sigma = +1$. The pressure is increased at $\theta = \pi$ and decreased at $\theta = 0$ at the rational surface for $\sigma = -1$. The change of the pressure is due to the convection of the radial flow as in the case of $\Psi_b = 0$. This feature is also same as in the case of Chapter 3. In both cases, the flat structure in the separatrix is kept in the nonlinear saturation.

5.4 Summary

The effect of the static magnetic island with the mode number of $(m, n) = (1, 1)$ on the resistive interchange mode with the same mode number is studied by using the equilibrium including the static island with a finite pressure gradient at the X-point. The linear growth rate is decreased with the increase of the island width. The interchange mode is stabilized by the static island with a substantial width in spite of the existence of the pressure gradient at the X-point. The marginal island width is 88% of the half-width of the stream function obtained in the case without the static island. The marginal island width is broader than that in the case of the annual flattening pressure profile.

When the interchange mode is unstable for the small island width, the steady state

due to the nonlinear saturation is obtained after the linear growth. The amplitude of the stream function in the steady state is decreased with the increase of the static island width. On the other hand, the half-width of the mode is almost independent of the static island width even in the steady state. The decrease of the amplitude of the stream function leads to the reduction of the kinetic energy in the steady state. This seems to be consistent with the experiment by Yamada et al. [30]. They studied the stabilization effect of the static island generated by the LID coil current on the (m, n)=(1,1) interchange mode in the configuration with the plasma aspect ratio of $A_p = 8.3$. They showed that the pressure gradient at the resonant surface is decreased and the magnetic fluctuation is reduced as the LID coil current is increased.

The island width and the phase of the island are changed by the nonlinear saturation of the interchange mode. The flow generated by the interchange mode brings the local variation in the pressure profile through the convection. The radially inward and the outward flows increase and decrease the pressure, respectively. The island width increases when the flow direction is radially outward at the X-point of the initial equilibrium island and the island width decreases when the flow direction is radially inward at the X-point. The relation between the change of the island width and the radial direction of the flow is consistent with the driven reconnection of the field lines as discussed in Chapter 3. In the present study, we observed a small $(m, n) = (2, 2)$ structure of the island. This result depends on the choice of the dissipation parameters. If we would take the parameters so that the linear growth rate of $(m, n) = (2, 2)$ mode should be much smaller than that of the $(m, n) = (1, 1)$ mode, the structure would disappear.

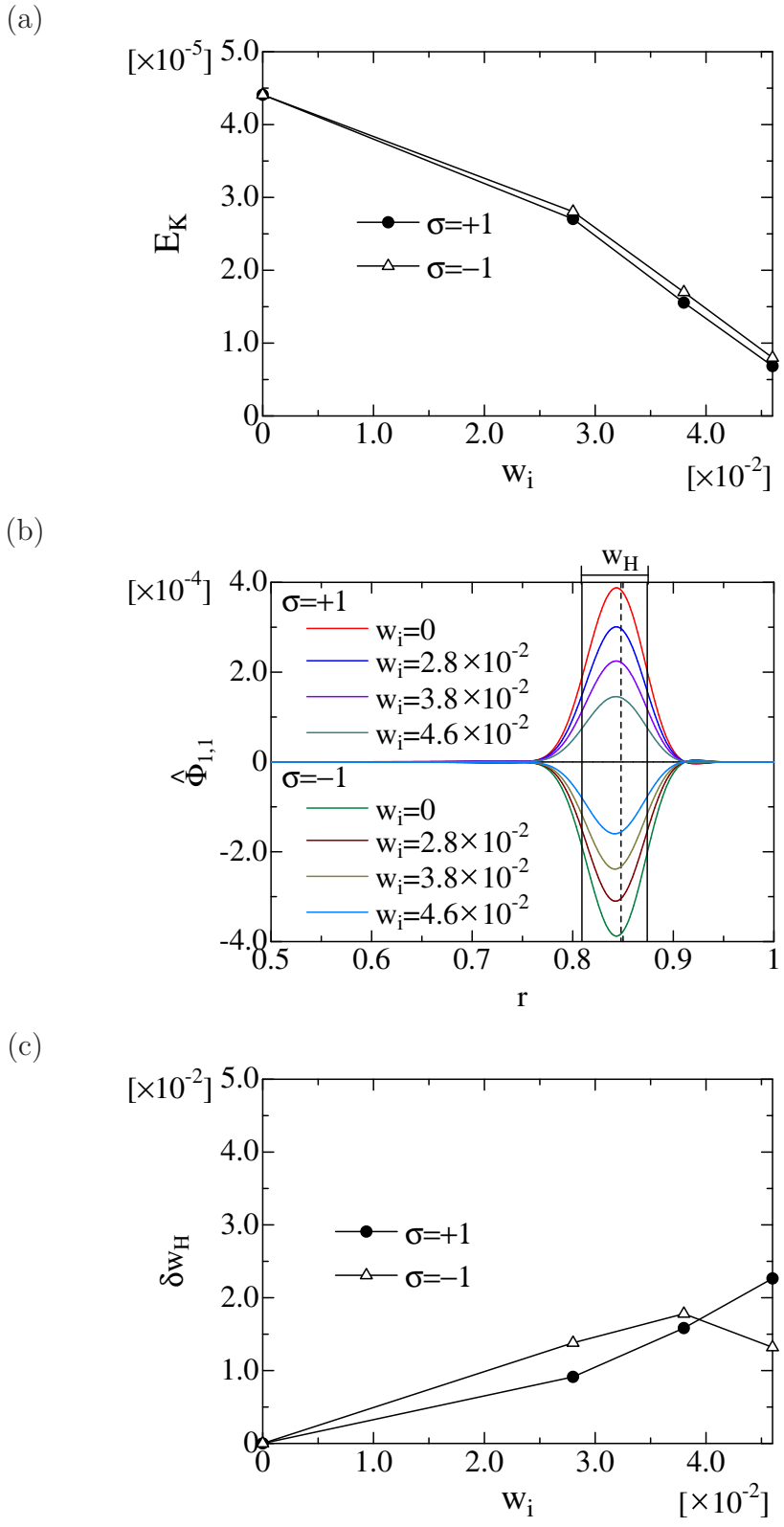

Figure 5.4: (a) Dependence of the kinetic energy in the steady state on w_i, (b) profiles of $\hat{\Phi}_{1,1}$ in the steady state. Vertical black solid lines indicate the position of half value of $\hat{\Phi}_{1,1}$ in the steady state for $\Psi_b = 0$. (c) Dependence of δw_H on w_i.

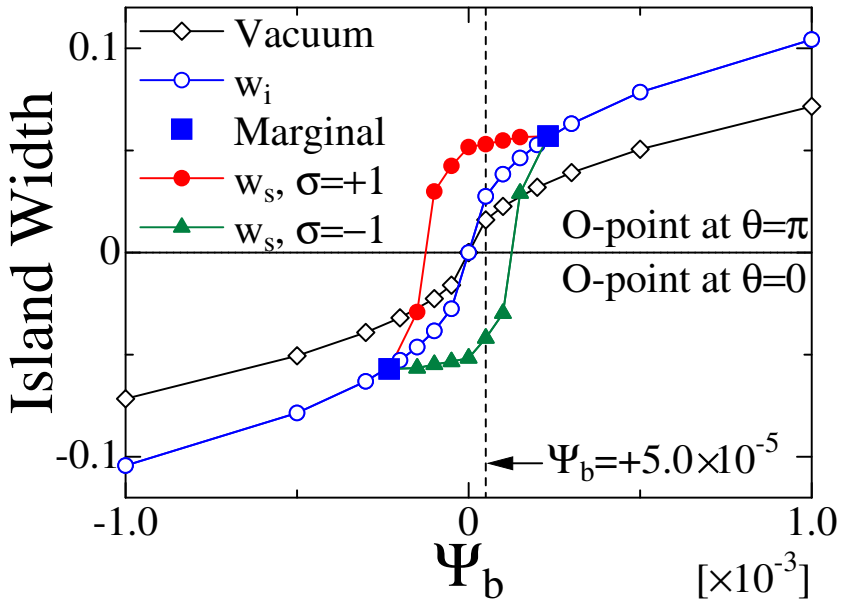

Figure 5.5: Dependence of island width on Ψ_b. Positive values correspond to the island with the O-point at $\theta = \pi$. Negative values correspond to the island with the O-point at $\theta = 0$. Diamonds show the island width in vacuum. Blue circles and squares show w_i and the marginal width, respectively. Red circles and green triangles show the island width after saturation of interchange modes for $\sigma = +1$ and $\sigma = -1$, respectively.

(a)

(b)

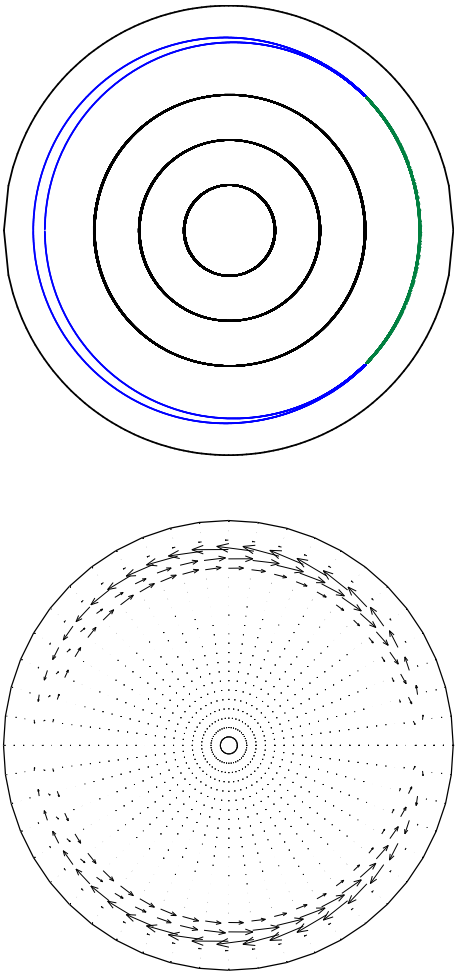

Figure 5.6: (a) Magnetic surfaces and (b) flow pattern at $t = 10000\tau_A$ for $w_i = 0$ ($\Psi_b = 0$) and $\sigma = +1$.

(a)

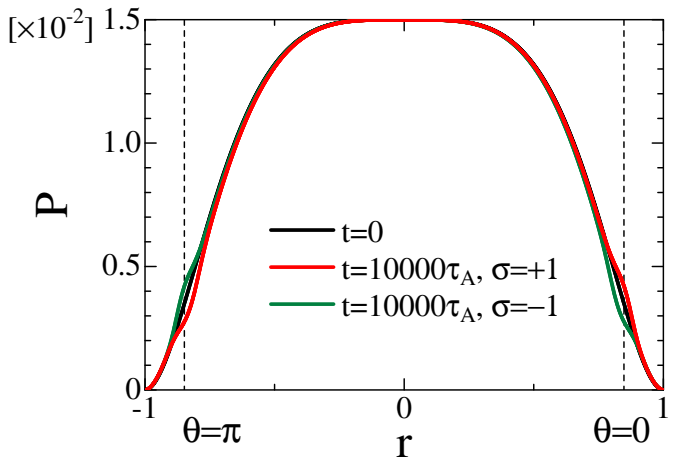

(b)

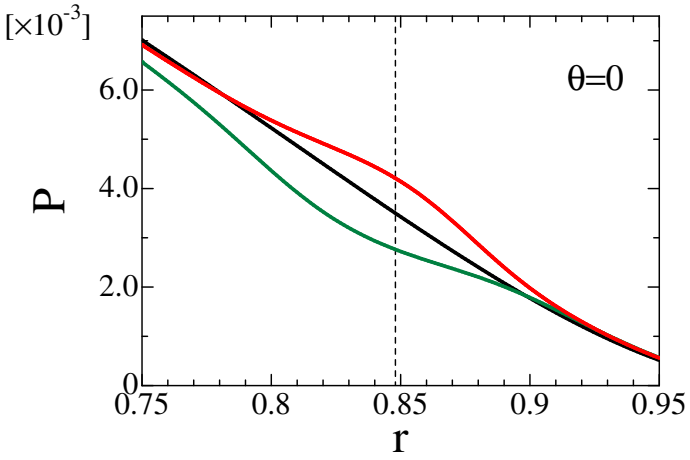

(c)

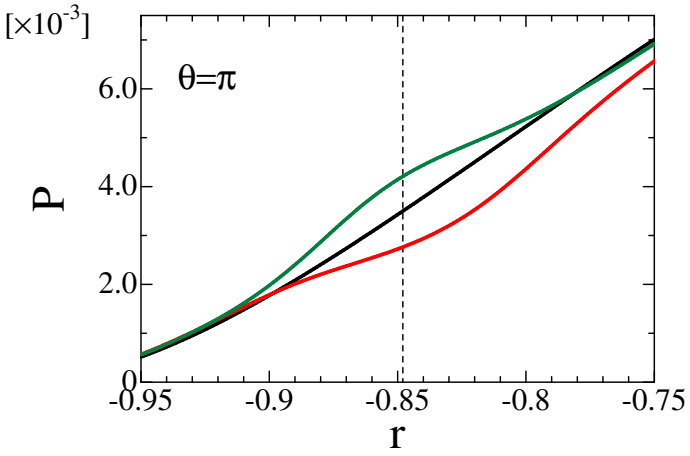

Figure 5.7: Profile of pressure (a) along the line connecting $(r = 1, \theta = 0, z = 0)$ and $(r = 1, \theta = \pi, z = 0)$ and its enlargements at (b) $\theta = 0$ and (c) $\theta = \pi$ for $w_i = 0$ ($\Psi_b = 0$) and $\sigma = \pm 1$. Black solid line shows the equilibrium pressure profile. Red and green solid line show the pressure profile in the steady state ($t = 10000\tau_A$) for $\sigma = +1$ and $\sigma = -1$, respectively. Vertical dashed lines indicate the position of the rational surface.

(a)

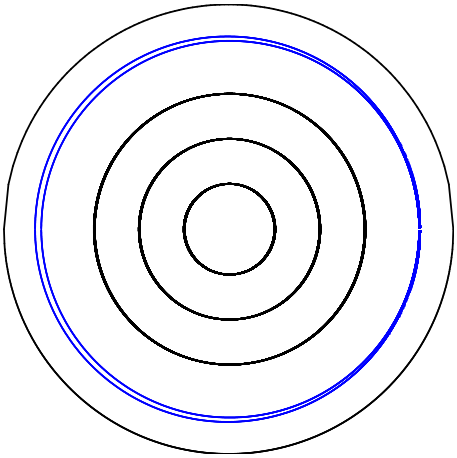

(b)

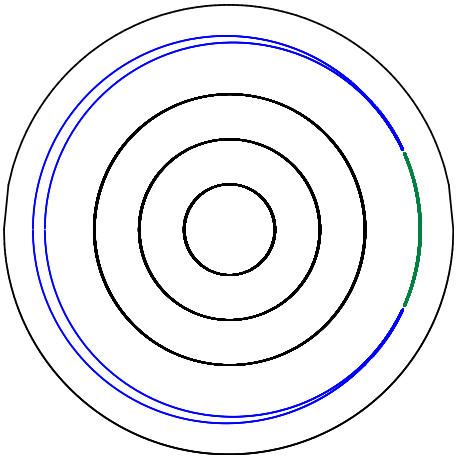

(c)

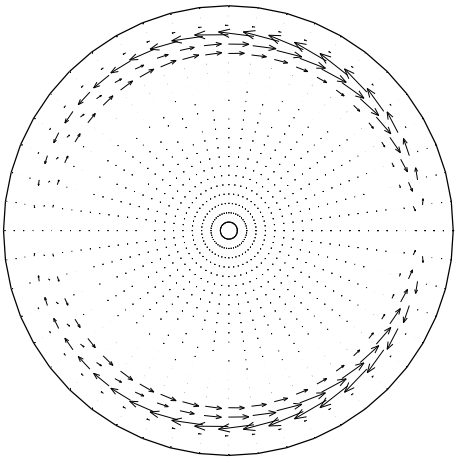

Figure 5.8: Magnetic surfaces at (a) $t = 0$ and (b) $t = 14000\tau_A$ and (c) flow pattern at $t = 14000\tau_A$ for $w_i = +2.8 \times 10^{-2}$ ($\Psi_b = +5.0 \times 10^{-5}$) and $\sigma = +1$.

(a)

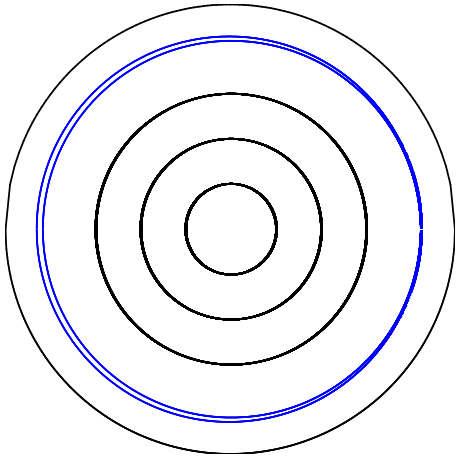

(b)

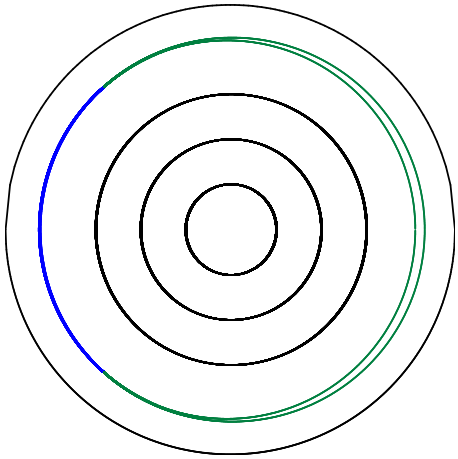

(c)

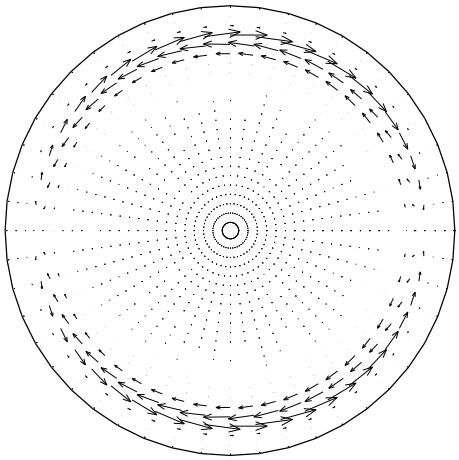

Figure 5.9: Magnetic surfaces at (a) $t = 0$ and (b) $t = 14000\tau_A$ and (c) flow pattern at $t = 14000\tau_A$ for $w_i = +2.8 \times 10^{-2}$ ($\Psi_b = +5.0 \times 10^{-5}$) and $\sigma = -1$.

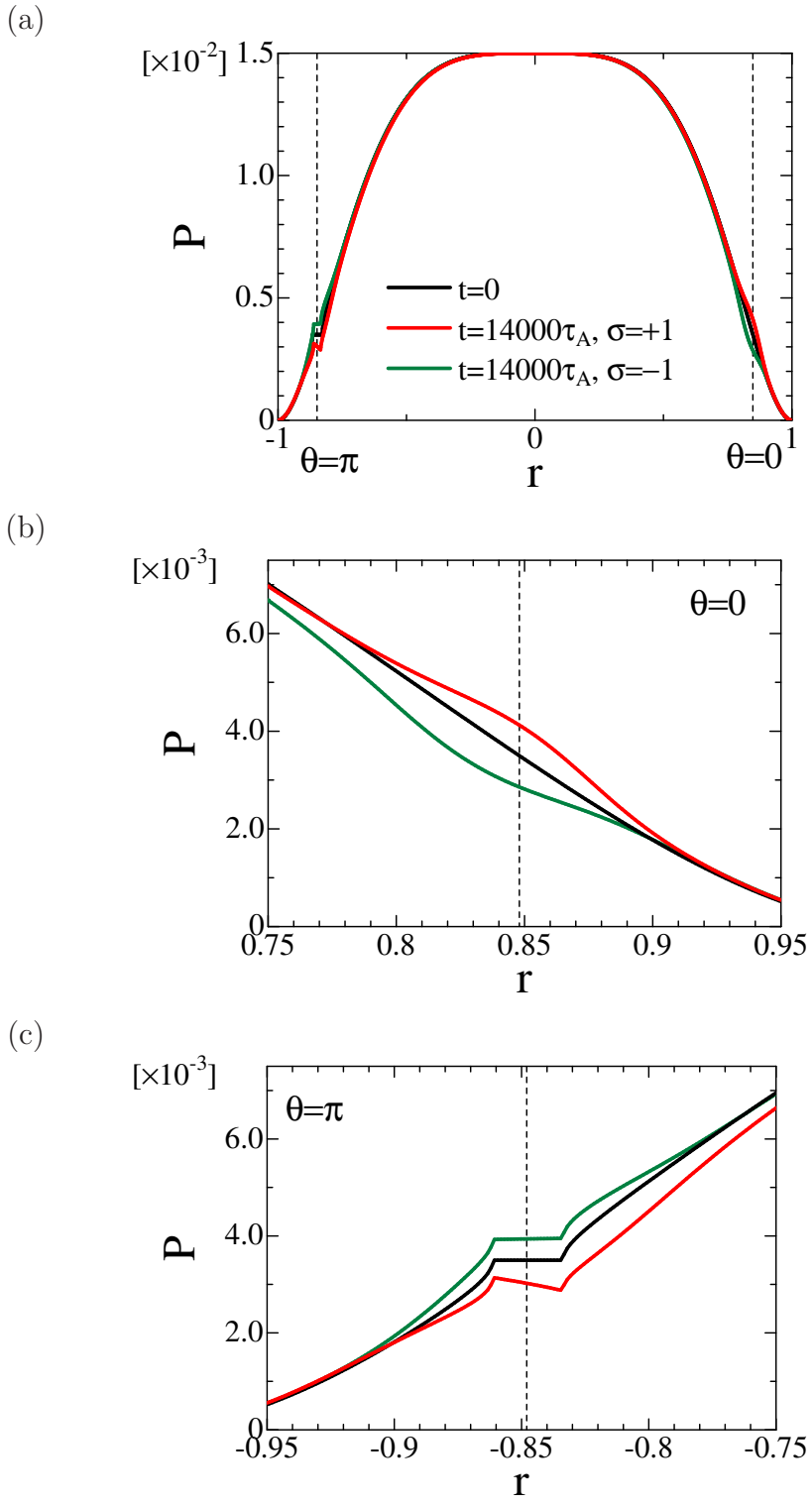

Figure 5.10: Profile of pressure (a) along the line connecting $(r = 1, \theta = 0, z = 0)$ and $(r = 1, \theta = \pi, z = 0)$ and its enlargements at (b) $\theta = 0$ and (c) $\theta = \pi$. Black solid line shows the equilibrium pressure profile. Red and green solid line show the pressure profile in the steady state ($t = 14000\tau_A$) for $w_i = +2.8 \times 10^{-2}$ ($\Psi_b = +5.0 \times 10^{-5}$) and $\sigma = \pm 1$, respectively. Vertical dashed lines indicate the position of the rational surface.

Chapter 6

Conclusions

The interaction between the static magnetic island with mode number of $(m, n) = (1, 1)$ and the resistive interchange mode with the same mode number is studied by utilizing the reduced MHD equations in straight heliotron configurations. The single heliciity perturbations are employed and the poloidal uniform flow is not included. We assume a high resistivity and choose appropriate dissipation coefficients so that the (m, n)=(1,1) mode has the largest growth rate. Two aspects of the interaction are studied by using different MHD equilibria. One is the effect of the interchange mode on the change of the static island and the other is the effect of the existence of the static island on the growth of the interchange mode.

The former aspect of the interaction is studied by using the equilibrium with the pressure profile corresponding to nested magnetic surfaces. The growth of the interchange mode is obtained as in the case without the static island. The linear growth rate of each component is almost the same. This is attributed to the fact that the component of $(m, n) = (1, 1)$ is dominant and each mode couples with the $(m, n) = (1, 1)$ component of the equilibrium. It is also obtained that the stream function after the nonlinear saturation is almost constant for the variation in the external poloidal flux. Both solutions corresponding to the increase and the decrease of the island width in the nonlinear evolution of the interchange mode are obtained when the parallel diffusion of the equilibrium pressure is neglected. In this case, in spite of the nonlinear interaction, the poloidal flux corresponding to the island in the saturation phase is almost determined by the linear sum of the poloidal flux for the vacuum static island and the poloidal flux generated by the interchange mode without the static island. In the case with the effect of the parallel diffusion, only the increase of the island is obtained. This results from the fact that the parallel diffusion term generates the component of the

interchange mode which increases the poloidal flux at the resonant surface.

For the study of the latter aspect of the interaction, a numerical code solving MHD equilibria including the static island based on the reduced MHD equations is developed. The equilibrium is obtained as a solution of coupled equations for the pressure and the poloidal flux. We develop two different schemes based on a two-step procedure. One is the scheme utilizing a parallel diffusion equation and an ordinary equation. The other is the scheme utilizing a field line tracing and a relaxation method. The former scheme gives a solution with a locally flat pressure profile at not only the O-point but also the X-point. In this case, the pressure gradient is continuous at the separatrix. The latter scheme can also give a solution of which the pressure profile is flat at the O-point and steep at the X-point. In this case, the pressure gradient is discontinuous at the separatrix of the island. The island width of the equilibrium is increased due to the finite beta.

The latter aspect of the interaction is studied by utilizing the equilibria with a finite gradient at the X-point. Since it is already known that the annular flat structure of the pressure profile has a stabilizing contribution to the interchange mode. We examine the equilibrium with the steep pressure gradient at the X-point. The stability dependence on the island width is analyzed. The linear growth rate is decreased with the increase of the island width. The mode is completely stabilized when the island width exceeds a marginal value in spite of the existence of the pressure gradients at the X-point. The marginal island width is 88% of the half-width of the stream function obtained for the equilibrium without a static island. The marginal width is broader than that in the case of the annual flattening. When the interchange mode is unstable with the static island, the steady state is obtained due to the nonlinear saturation after the linear growth. The amplitude of the stream function in the steady state is decreased with the increase of the static island width, while the half-width is almost independent of the island width. Therefore, the saturation level of the kinetic energy decreases with the increase of the static island. This tendency seems to be consistent with the experimental result [30] that the magnetic fluctuation is reduced when the local flat structure in the pressure profile is observed in the increase of the amplitude of the resonant error field generated by the LID coils.

We also examine the behavior of the island in the nonlinear evolution of the mode for the equilibrium including the static island. Both solution of the increase and the decrease of the island width exist. The island width increases when the flow direction is radially outward at the X-point of the initial static island, while the island width

decrease when the flow direction is radially inward at the X-point. The relation between the radial direction of the flow and the change of the island width is consistent with the driven reconnection of the field lines. These features are common with the case of the nested magnetic surface equilibrium studied for the former aspect.

Following points are considered as future works. In this study, the effect of the uniform poloidal flow is not included. If the effect is included, the islands are possible to rotate by the flow due to interchange modes. The effect can affect the results in the island behavior and the mode stability. As another future work, it is consider to employ multiple helicity perturbations. Single helicity perturbation $m/n = 1$ is employed in order to see the same mode interaction clearly. When the multiple helicity perturbations are employed, the interchange modes at rational surfaces different from the island surface can be excited. If such modes grow substantially, they can interact the island indirectly through the change in the structure of the magnetic field and the pressure profile. In the equilibrium with the steep gradient at the X-point, the pressure gradient at the rational surface $\iota = 1$ is zero except the X-point. However, the gradient just outside of the separatrix is increased by the existence of the static island. The increase of the gradient can destabilize the interchange mode at the surfaces in the vicinity of the island. Actually, Watanabe et al. [31] studied the effect of the static island with mode number of $(m, n) = (1, 1)$ on the MHD activity experimentally. The (m, n)=(3,4) fluctuation was observed by the enhancement of the static island. Incorporating the effect is necessary for the comprehensive understanding of the stabilizing contribution of the static islands.

Appendix A

Improvement of the NORM code

To study the effect of the interchange mode on the static island, the boundary condition of Eq.(3.5) has to be satisfied even in the finite beta plasma where the interchange mode develops. However, the boundary condition of Eq.(3.5) was not incorporated in the original NORM code. Therefore, the improvement of the NORM code is needed to follow the time evolution of the mode including the static island. The procedure of the improvement of the NORM code is as follows.

In Chapter 3, the static island is introduced by satisfying the boundary condition given by Eq.(3.5). We assume that the same external poloidal flux always exists at $r = 1$ even in the finite beta plasma. This assumption is also employed in Ref. [12–14]. To introduce static islands, we need to change the initial condition and the boundary condition of $\hat{\Psi}_{1,1}$ because $\hat{\Psi}_{1,1}(r = 1) = 0$ is used in the time evolution in the original NORM code. At first, we change the initial condition as follows. In the case with $(m, n) = (1, 1)$, Eq.(2.14) is given by

$$\frac{d^2\hat{\Psi}_{1,1}}{dr^2} + \frac{1}{r}\frac{d\hat{\Psi}_{1,1}}{dr} - \frac{\hat{\Psi}_{1,1}}{r^2} = \hat{J}z_{1,1}. \tag{A.1}$$

Since the second-order accurate central-difference scheme is employed as the radial derivative in the NORM code, Eq.(A.1) can be written by

$$\nabla_\perp^2 \hat{\Psi}_{1,1(i)} = L_i\hat{\Psi}_{1,1(i-1)} + C_i\hat{\Psi}_{1,1(i)} + R_i\hat{\Psi}_{1,1(i+1)} = \hat{J}_{z\ 1,1(i)}, \tag{A.2}$$

where L_i, C_i and R_i are given by

$$L_i = \frac{1}{(\Delta r)^2}(1 - \frac{1}{2i}), \quad C_i = \frac{-1}{(\Delta r)^2}(2 + \frac{1}{i^2}), \quad R_i = \frac{1}{(\Delta r)^2}(1 + \frac{1}{2i}). \tag{A.3}$$

Here, i and Δr mean the number of each grid point and the grid size, respectively. By

using the boundary conditions of

$$\hat{\Psi}_{1,1}(r=0)=0 \tag{A.4}$$

and

$$\hat{\Psi}_{1,1}(r=1)=\Psi_b. \tag{A.5}$$

Equation (A.2) for $i=1$ and $i=N_g-1$ are given by

$$C_1\hat{\Psi}_{1,1(1)}+R_1\hat{\Psi}_{1,1(2)}=\hat{J}_{z\ 1,1(1)} \tag{A.6}$$

and

$$L_{N_g-1}\Psi_{1,1(N_g-2)}+C_{N_g-1}\Psi_{1,1(N_g-1)}+R_{N_g-1}\Psi_b=J_{z\ 1,1(N_g-1)}, \tag{A.7}$$

respectively. Here, N_g is the total number of grid points. The matrix corresponding to $(A.2),(A.6),(A.7)$ is as follows.

$$\begin{pmatrix} C_1 & R_1 & 0 & & \cdots & & 0 \\ 0 & L_2 & C_2 & R_2 & 0 & \cdots & \vdots \\ \vdots & 0 & \ddots & \ddots & \ddots & \ddots & \\ & \cdots & \ddots & \ddots & \ddots & \ddots & 0 \\ & \cdots & & 0 & L_{N_g-2} & C_{N_g-2} & R_{N_g-2} \\ 0 & & \cdots & & 0 & L_{N_g-1} & C_{N_g-1} \end{pmatrix} \begin{pmatrix} \hat{\Psi}_{1,1(1)} \\ \vdots \\ \\ \\ \hat{\Psi}_{1,1(N_g-2)} \\ \hat{\Psi}_{1,1(N_g-1)} \end{pmatrix} = \begin{pmatrix} \hat{J}_{z\ 1,1(1)} \\ \vdots \\ \\ \\ \hat{J}_{z\ 1,1(N_g-2)} \\ \hat{J}_{z\ 1,1(N_g-1)}-R_{N_g-1}\Psi_b \end{pmatrix} \tag{A.8}$$

In Eq.(A.8), the term $R_{N_g-1}\Psi_b$ of LHS in Eq.$(A.7)$ is moved to RHS. The new subroutine solving Eq.(A.8) for the initial condition of $\hat{\Psi}_{1,1}$ with the recurrence formula [32] is developed in the NORM code.

Next, we consider to incorporate the boundary condition of Eq.(A.5) in the case of $t>0$. In the NORM code, Eq.(2.9) is integrated by Crank Nicolson method and the improved Euler's method. This method is composed of two steps. The first step of the method for Eq. (2.9) is given by

$$\frac{\Psi_{(i)}^{j+\frac{1}{2}}-\Psi_{(i)}^{j}}{(\Delta t/2)}=-\mathbf{B}_{(i)}^{j}\cdot\nabla\Phi_{(i)}^{j}+\frac{1}{S}\left(\frac{1}{2}\nabla_{\perp}^{2}\Psi_{(i)}^{j}+\frac{1}{2}\nabla_{\perp}^{2}\Psi_{(i)}^{j+\frac{1}{2}}\right), \tag{A.9}$$

where Δt and j are the time step size and the number of time step, respectively. Equation $(A.9)$ becomes

$$\left(1-\frac{1}{2}\frac{1}{S}\frac{\Delta t}{2}\nabla_{\perp}^{2}\right)\Psi_{(i)}^{j+\frac{1}{2}}=\Psi_{(i)}^{j}+\frac{\Delta t}{2}\left(-\mathbf{B}_{(i)}^{j}\cdot\nabla\Phi_{(i)}^{j}+\frac{1}{2}\frac{1}{S}\nabla_{\perp}^{2}\Psi_{(i)}^{j}\right). \tag{A.10}$$

Equation (A.10) has the same structure as Eq.(A.2) if $\nabla_\perp^2$ is replaced with $\left(1-\frac{1}{2}\frac{1}{S}\frac{\Delta t}{2}\nabla_\perp^2\right)$ and J_z is replaced with RHS of Eq.(A.10). Therefore, by substituting L_i', C_i' and R_i' defined as

$$L_i' = -\frac{1}{4}\frac{\Delta t}{S}L_i, \quad C_i' = 1-\frac{1}{4}\frac{\Delta t}{S}C_i, \quad R_i' = -\frac{1}{4}\frac{\Delta t}{S}R_i, \tag{A.11}$$

into Eq.(A.8) for L_i, C_i and R_i and using $\frac{1}{4}\frac{1}{S}\Delta t R_{N_g-1}\Psi_b$ for $-R_{N_g-1}\Psi_b$, the boundary condition of Eq.(A.5) for first step is satisfied even the case of $t>0$. In the second step, equation corresponding to (A.10) is given by

$$\left(1-\frac{1}{2}\frac{1}{S}\Delta t\nabla_\perp^2\right)\Psi_{(i)}^{j+1} = \Psi_{(i)}^{j} + \Delta t\left(-\mathbf{B}_{(i)}^{j+\frac{1}{2}}\cdot\nabla\Phi_{(i)}^{j+\frac{1}{2}} + \frac{1}{S}\frac{1}{2}\nabla_\perp^2\Psi_{(i)}^{j}\right). \tag{A.12}$$

By replacing $\Delta t/2$ of Eq.(A.10) with Δt and using $\frac{1}{2}\frac{1}{S}\Delta t R_{N_g-1}\Psi_b$ for $-R_{N_g-1}\Psi_b$, the boundary condition of Eq.(A.5) for the second step is satisfied for $t>0$ as well as for the first step.

Appendix B

Development of the FLEC code

To study the effect of the static island on the interchange mode, MHD equilibrium including the static island is required. Therefore, the FLEC code solving the coupled equations given by Eqs. (4.1) and (4.2) is developed. The coupled equations are solved iteratively by means of the two steps as shown in Fig.4.1. The FLEC code is composed of two parts. One is the method utilizing parallel diffusion and the other is the field line tracing method. In this Appendix, the details of the schemes are explained.

B.1 Numerical scheme of method utilizing parallel diffusion

In this method, we employ the Fourier series for $\tilde{P}(r,\theta,z)$ and $\tilde{\Psi}(r,\theta,z)$ as expressed in Eqs.(4.9) and (4.10), respectively. The boundary conditions of $\tilde{P}$ and $\tilde{\Psi}$ at $r=0$

$$\left.\frac{d\hat{f}_{0,0}}{dr}\right|_{r=0} = 0 \quad and \quad \hat{f}_{n,n}(r=0) = 0 \ \ (n \neq 0) \tag{B.1}$$

are employed, where f corresponds to $\tilde{P}$ and $\tilde{\Psi}$. The boundary condition of $\tilde{P}$ and $\tilde{\Psi}$ at $r=1$

$$\hat{f}_{n,n}(r=1) = 0 \tag{B.2}$$

is employed.

In the first step, Eqs.(4.13)-(4.15) are solved. The expression of the right hand side of Eq.(4.13)-(4.15) in the central finite difference form, $DP_{n,n}$ is given

$$DP_{1,1}(t) = \frac{\kappa_{\parallel}\Psi_b}{2}\Big[\frac{1-\iota_{(i)}}{r_{(i)}}\hat{P}_{1,1(i)} + \frac{\Psi_b}{r_{(i)}}\frac{P_{sym(i+1)} + P_{0,0(i+1)} - P_{sym(i-1)} - P_{0,0(i-1)}}{2\Delta r}$$

$$+(1-\text{ɬ}_{(i)})\frac{\hat{P}_{1,1(i+1)}-\hat{P}_{1,1(i-1)}}{2\Delta r}-\frac{\text{ɬ}_{(i+1)}-\text{ɬ}_{(i-1)}}{2\Delta r}\hat{P}_{1,1(i)}$$
$$+\Psi_b\frac{P_{sym(i+1)}-2P_{sym(i)}+P_{sym(i-1)}+\hat{P}_{0,0(i+1)}-2\hat{P}_{0,0(i)}+\hat{P}_{0,0(i-1)}}{\Delta r^2}$$
$$-\frac{\Psi_b}{2}\Big(\frac{\hat{P}_{2,2(i+1)}-2\hat{P}_{2,2(i)}+\hat{P}_{2,2(i-1)}}{\Delta r^2}+\frac{3}{r}\frac{\hat{P}_{2,2(i+1)}-\hat{P}_{2,2(i-1)}}{2\Delta r}\Big)\Big], \tag{B.3}$$

$$DP_{2,2}(t)=\kappa_{\parallel}\Big\{-(1-\text{ɬ}_{(i)})\big[(1-\text{ɬ}_{(i)})\hat{P}_{1,1(i)}+\Psi_b\frac{P_{sym(i+1)}-P_{sym(i-1)}+\hat{P}_{0,0(i+1)}-\hat{P}_{0,0(i-1)}}{2\Delta r}\big]$$
$$+\frac{\Psi_b^2}{4}\Big(\frac{\hat{P}_{1,1(i+1)}-2\hat{P}_{1,1(i)}+\hat{P}_{1,1(i-1)}}{\Delta r^2}+\frac{\hat{P}_{1,1(i+1)}-\hat{P}_{1,1(i-1)}}{2r_{(i)}\Delta r}-\frac{\hat{P}_{1,1(i)}}{r_{(i)}^2}\Big)$$
$$+\frac{3\Psi_b}{2}(1-\text{ɬ}_{(i)})\frac{\hat{P}_{2,2(i+1)}-\hat{P}_{2,2(i-1)}}{2\Delta r}+3\Psi_b(1-\text{ɬ}_{(i)})\frac{\hat{P}_{2,2(i)}}{r_{(i)}}-\Psi_b\frac{\text{ɬ}_{(i+1)}-\text{ɬ}_{(i-1)}}{2\Delta r}\hat{P}_{2,2(i)}\Big\} \tag{B.4}$$

and

$$DP_{3,3}(t)=\kappa_{\parallel}\Big\{-2(1-\text{ɬ}_{(i)})\big[2(1-\text{ɬ}_{(i)})\hat{P}_{2,2(i)}+\frac{\Psi_b}{2}\Big(\frac{\hat{P}_{1,1(i+1)}-\hat{P}_{1,1(i-1)}}{2\Delta r}-\frac{\hat{P}_{1,1(i)}}{r_{(i)}}\Big)\big]$$
$$+\frac{\Psi_b}{2}\Big[\frac{1-\text{ɬ}_{(i)}}{r_{(i)}}\hat{P}_{1,1(i)}+\frac{\Psi_b}{r_{(i)}}\frac{P_{sym(i+1)}+P_{0,0(i+1)}-P_{sym(i-1)}-P_{0,0(i-1)}}{2\Delta r}$$
$$+\frac{\text{ɬ}_{(i+1)}-\text{ɬ}_{(i-1)}}{2\Delta r}\hat{P}_{1,1(i)}-(1-\text{ɬ}_{(i)})\frac{\hat{P}_{(i+1)}-\hat{P}_{(i-1)}}{2\Delta r}\Big]$$
$$-\Psi_b\frac{P_{sym(i+1)}-2P_{sym(i)}+P_{sym(i-1)}+P_{0,0(i+1)}-2P_{0,0(i)}+P_{0,0(i-1)}}{\Delta r^2}$$
$$+\frac{\Psi_b^2}{2}\Big(\frac{\hat{P}_{2,2(i+1)}-2\hat{P}_{2,2(i)}+\hat{P}_{2,2(i-1)}}{\Delta r^2}+\frac{\hat{P}_{2,2(i+1)}-\hat{P}_{2,2(i-1)}}{2r_{(i)}\Delta r}-\frac{4}{r_{(i)}^2}\hat{P}_{2,2(i)}\Big)\Big\}. \tag{B.5}$$

Here, the subscript of ' i 'denotes the radial grid number. Equation (4.13)-(4.15) are integrated by the improved Euler's method as

$$P_{n,n}(t+\Delta t/2)=P_{n,n}(t)+\frac{\Delta t}{2}DP_{n,n}(t) \tag{B.6}$$

and

$$P_{n,n}(t+\Delta t)=P_{n,n}(t)+\Delta t\{DP_{n,n}(t+\Delta t/2)\}. \tag{B.7}$$

In the second step, $\tilde{\Psi}_{0,0}$ satisfying Eq.(4.24) is calculated from

$$\nabla_{\perp}^2\tilde{\Psi}_{0,0}=-\int\frac{1}{2\epsilon^2\Psi_b r}\frac{d\Omega_{sym}}{dr}\hat{P}_{1,1}dr. \tag{B.8}$$

The integration in the RHS of Eq.(B.8) is performed with the Simpson's rule. The LHS is represented as

$$\nabla_{\perp}^2\tilde{\Psi}_{0,0}=L_i\hat{\Psi}_{0,0}+C_i^0\hat{\Psi}_{0,0}+R_i\hat{\Psi}_{0,0}, \tag{B.9}$$

where C_i^0 is given by

$$C_i^0 = \frac{-2}{(\Delta r)^2}. \tag{B.10}$$

Equation (B.9) has the same structure as Eq.(A.2). Therefore, by replacing C_i with C_i^0, Eq.(B.9) can be solved with the same way in the case of Eq.(A.1).

B.2 Numerical scheme utilizing field line tracing method

In this method, we mainly utilize the real grids in the r and θ directions. In the first step, the pressure is calculated by field line tracing. Substituting Eqs.(4.3) and (4.4) into Eqs.(4.27) and (4.28), we obtain

$$\frac{dr}{dz} = \Psi_b \sin(\theta - z) - \frac{1}{r}\frac{\partial \tilde{\Psi}}{\partial \theta} \tag{B.11}$$

and

$$\frac{d\theta}{dz} = \boldsymbol{t}_{sym} + \frac{\Psi_b}{r}\cos(\theta - z) + \frac{1}{r}\frac{\partial \tilde{\Psi}}{\partial r}. \tag{B.12}$$

The equations are integrated by the 4th-order Runge-Kutta method given by

$$\phi^1 = \phi(z) + \Delta z h\{\phi(z)\}, \tag{B.13}$$

$$\phi^2 = \phi(z) + \Delta z h\left\{\frac{\phi(z) + \phi^1}{2}\right\}, \tag{B.14}$$

$$\phi^3 = \phi(z) + \Delta z h\left\{\frac{\phi(z) + \phi^2}{2}\right\}, \tag{B.15}$$

$$\phi^4 = \phi(z) + \Delta z h(\phi^3) \tag{B.16}$$

and

$$\phi(z + \Delta z) = \frac{1}{6}(\phi^1 + \phi^2 + \phi^3 + \phi^4), \tag{B.17}$$

where ϕ denotes r or θ and h corresponds to RHS in each equation of (B.11) and (B.12).

The second-order accurate central-difference scheme is employed for the derivatives of the radial and azimuthal direction. The values of $\boldsymbol{t}$ and $\tilde{\Psi}$ are calculated by means of the linear interpolation with the values at the nearest four grid points.

In the second step, we solve Eqs.(4.38) and (4.39). We utilize the improved Euler's method combined with the Crank-Nicolson method to solve Eq.(4.38). In this case,

the time evolution for one time step is composed of two steps. The formulation of this method for Eq.(4.38) is given by

$$\frac{\tilde{\Psi}(t+\Delta t/2)-\tilde{\Psi}(t)}{\Delta t/2} = -(\mathbf{B}\cdot\nabla\tilde{\Phi})(t) + \frac{1}{2}[\tilde{J}z(t)+\tilde{J}z(t+\Delta t/2)] \tag{B.18}$$

and

$$\frac{\tilde{\Psi}(t+\Delta t)-\tilde{\Psi}(t)}{\Delta t} = -(\mathbf{B}\cdot\nabla\tilde{\Phi})(t+\Delta t/2) + \frac{1}{2}[\tilde{J}z(t)+\tilde{J}z(t+\Delta t)]. \tag{B.19}$$

Equations (B.18) and (B.19) are represented as

$$\triangle^f\tilde{\Psi}(t+\Delta t/2) = -\frac{1}{(\Delta t/2)}2S\tilde{\Psi}(t) + 2S(\mathbf{B}\cdot\nabla\tilde{\Phi})(t) - \tilde{J}z(t) \tag{B.20}$$

and

$$\triangle^s\tilde{\Psi}(t+\Delta t) = -\frac{1}{\Delta t}2S\tilde{\Psi}(t) + 2S(\mathbf{B}\cdot\nabla\tilde{\Phi})(t+\Delta t/2) - \tilde{J}z(t), \tag{B.21}$$

where $\triangle^f$ and $\triangle^s$ are given by

$$\triangle^f = \nabla_\perp^2 - \frac{2S}{(\Delta t/2)}, \qquad \triangle^s = \nabla_\perp^2 - \frac{2S}{\Delta t}, \tag{B.22}$$

respectively.

The second-order accurate central-difference scheme is employed for the radial derivative and the azimuthal direction. Here, by utilizing helical symmetry of $n/m = 1$, the derivative in z direction is replaced as

$$\frac{\partial}{\partial z} = -\frac{\partial}{\partial\theta}. \tag{B.23}$$

Therefore, RHSs of Eqs.(B.20) and (B.21) A_1, A_2 are expressed as

$$A_{1(i)} = -\frac{1}{(\Delta t/2)}2S\tilde{\Psi}_{(i,k)}(t) + 2S\Big[\Big(r_{(i)}\not{\epsilon}_{(i)} - r_{(i)} + \Psi_b\cos\theta_k + \frac{\tilde{\Psi}_{(i+1,k)}-\tilde{\Psi}_{(i-1,k)}}{2\Delta r}\Big)\Big(\frac{\tilde{\Phi}_{(i,k+1)}-\tilde{\Phi}_{(i,k-1)}}{2\Delta\theta}\Big)$$

$$+\Big(\Psi_b\sin\theta_k - \frac{1}{r_{(i)}}\frac{\tilde{\Psi}_{(i,k+1)}-\tilde{\Psi}_{(i,k-1)}}{2\Delta\theta}\Big)\Big(\frac{\tilde{\Phi}_{(i+1,k)}-\tilde{\Phi}_{(i-1,k)}}{2\Delta r}\Big)\Big](t) - \tilde{J}z_{(i,k)}(t), \tag{B.24}$$

$$A_{2(i)} = -\frac{1}{\Delta t}2S\tilde{\Psi}_{(i,k)}(t) + 2S\Big[\Big(r_{(i)}\not{\epsilon}_{(i)} - r_{(i)} + \Psi_b\cos\theta_k + \frac{\tilde{\Psi}_{(i+1,k)}-\tilde{\Psi}_{(i-1,k)}}{2\Delta r}\Big)\Big(\frac{\tilde{\Phi}_{(i,k+1)}-\tilde{\Phi}_{(i,k-1)}}{2\Delta\theta}\Big)$$

$$+\Big(\Psi_b\sin\theta_k - \frac{1}{r_{(i)}}\frac{\tilde{\Psi}_{(i,k+1)}-\tilde{\Psi}_{(i,k-1)}}{2\Delta\theta}\Big)\Big(\frac{\tilde{\Phi}_{(i+1,k)}-\tilde{\Phi}_{(i-1,k)}}{2\Delta r}\Big)\Big](t+\Delta t/2) - \tilde{J}z_{(i,k)}(t), \tag{B.25}$$

respectively, where k and $\Delta\theta$ denote the grid number in the θ direction and the grid size in the θ direction, respectively. Here, $A_{1(i)}$ and $A_{2(i)}$ are expanded in the Fourier series given by

$$A_{1(i)} = \sum_{n=0}^{N_\theta - 1} \hat{A}_{1,n,n(i)} \cos(n\theta - nz), \quad A_{2(i)} = \sum_{n=0}^{N_\theta - 1} \hat{A}_{2,n,n(i)} \cos(n\theta - nz), \tag{B.26}$$

respectively. The poloidal flux $\tilde{\Psi}_{(i)}(t)$ is also expanded as

$$\tilde{\Psi}_{(i)}(t) = \sum_{n=0}^{N_\theta - 1} \hat{\Psi}_{n,n(i)}(t) \cos(n\theta - nz), \tag{B.27}$$

where N_θ is the total grid number in the θ direction. Here, $N_\theta = 45$ is employed in this study. Therefore, Eqs.(B.20) and (B.21) for each Fourier component can be expressed as

$$L_i \hat{\Psi}_{n,n(i+1)}(t + \Delta t/2) + S_i^1 \hat{\Psi}_{n,n(i)}(t + \Delta t/2) + R_i \hat{\Psi}_{n,n(i-1)}(t + \Delta t/2) = \hat{A}_{1,n,n(i)}, \tag{B.28}$$

$$L_i \hat{\Psi}_{n,n(i+1)}(t + \Delta t) + S_i^2 \hat{\Psi}_{n,n(i)}(t + \Delta t) + R_i \hat{\Psi}_{n,n(i-1)}(t + \Delta t) = \hat{A}_{2,n,n(i)}, \tag{B.29}$$

respectively. Here, L_i and R_i are given in Eq.(A.3), and S_i^1 and S_i^2 are given by

$$S_i^1 = \frac{-1}{(\Delta r)^2}(2 + \frac{n^2}{i^2}) - \frac{2S}{(\Delta t/2)}, \quad S_i^2 = \frac{-1}{(\Delta r)^2}(2 + \frac{n^2}{i^2}) - \frac{2S}{\Delta t} \tag{B.30}$$

respectively. As in the case of Appendix A, by solving Eqs.(B.28) and (B.29) with the recurrence formula under the boundary conditions

$$\tilde{\Psi}(r = 0, \theta, z) = \hat{\Psi}_{0,0}(r = 0) \quad and \quad \tilde{\Psi}(r = 1, \theta, z) = 0, \tag{B.31}$$

we obtain $\hat{\Psi}_{n,n(i)}(t + \Delta t/2)$ and $\hat{\Psi}_{n,n(i)}(t + \Delta t)$.

Equation (4.39) is solved with the improved Euler's method. The formulation for this equation is given by

$$\tilde{U}(t + \Delta t/2) = \tilde{U}(t) + \frac{\Delta t}{2}\Big[- (\mathbf{B} \cdot \nabla \tilde{J}_z)(t) + \frac{1}{2\epsilon^2} \nabla\Omega \times \nabla P \cdot \mathbf{z} + \nu \nabla_\perp^2 \tilde{U}(t)\Big] \tag{B.32}$$

and

$$\tilde{U}(t+\Delta t) = \tilde{U}(t) + \Delta t\Big[-(\mathbf{B}\cdot\nabla \tilde{J}_z)(t+\Delta t/2) + \frac{1}{2\epsilon^2}\nabla\Omega\times\nabla P\cdot\mathbf{z} + \nu\nabla_\perp^2 \tilde{U}(t+\Delta t/2)\Big] \tag{B.33}$$

and the boundary conditions for $\tilde{U}$ are

$$\tilde{U}(r = 0, \theta, z) = 0 \quad and \quad \tilde{U}(r = 1, \theta, z) = 0. \tag{B.34}$$

In order to solve Eqs.(4.38) and (4.39) simultaneously, we have to solve Eq.(2.14) to obtain $\tilde{\Phi}$. We utilize the Fourier series of $\tilde{U}$ and $\tilde{\Phi}$ given by

$$\tilde{U}(r,\theta,z) = \sum_{n=0,m=n}^{N_\theta-1} \tilde{U}_{m,n}, \quad \tilde{U}_{m,n} = \hat{U}_{m,n}(r)\sin(m\theta - nz), \tag{B.35}$$

and

$$\tilde{\Phi}(r,\theta,z) = \sum_{n=0,m=n}^{N_\theta-1} \tilde{\Phi}_{m,n}, \quad \tilde{\Phi}_{m,n} = \hat{\Phi}_{m,n}(r)\sin(m\theta - nz), \tag{B.36}$$

respectively. Then, Eq.(2.14) has the form of

$$\frac{d^2\hat{\Phi}_{m,n}}{dr^2} + \frac{1}{r}\frac{d\hat{\Phi}_{m,n}}{dr} - \frac{m^2}{r^2}\hat{\Phi}_{m,n} = \hat{U}_{m,n}. \tag{B.37}$$

In this case, Eq.(B.37) is represented as

$$L_i\hat{\Phi}_{m,n(i-1)} + C_i^m\hat{\Phi}_{m,n(i)} + R_i\hat{\Phi}_{m,n(i+1)} = \hat{U}_{m,n}, \tag{B.38}$$

where C_i^m is given by

$$C_i^m = \frac{-1}{(\Delta r)^2}(2 + \frac{m^2}{i^2}). \tag{B.39}$$

Equation (B.38) is also solved with the same way in the case of Eq.(A.1).

After we obtain the Fourier components of $\hat{\Psi}_{n,n(i)}(t+\Delta t)$ and $\hat{\Phi}_{n,n(i)}(t+\Delta t)$, we calculate the values at the real grid points, $\tilde{\Psi}_{(i,k)}(t+\Delta t)$ and $\tilde{\Phi}_{(i,k)}(t+\Delta t)$, which are used for the calculation of the next time step.

Bibliography

[1] F. L. Waelbroeck, Nucl. Fusion **49**, 104025 (2009).

[2] M.E. Fenstermacher, M. Becoulet, P. Cahyna, J. Canik, C.S. Chang, T.E. Evans, P. Gohil, S. Kaye, A. Kirk, Y. Liang, A. Loarte, R. Maingi, O. Schmitz, W. Suttrop and H.R. Wilson, Proceedings of 23rd IAEA Fusion Energy Conference, Daejon, Korea Rep. of Conference, 11-16 October 2010, ITR/P1-30.

[3] A. Komori, H. Yamada, S. Sakakibara, O. Kaneko, K. Kawahata, T. Mutoh, N. Ohyabu, S. Imagawa, K. Ida, Y. Nagayama, T. Shimozuma, K.Y. Watanabe, T. Mito, M. Kobayashi, K. Nagaoka, R. Sakamoto, N. Yoshida, S. Ohdachi, N. Ashikawa, Y. Feng, T. Fukuda, H. Igami, S. Inagaki, H. Kasahara, S. Kubo, R. Kumazawa, O. Mitarai, S. Murakami, Yuji Nakamura, M. Nishiura, T. Hino, S. Masuzaki, K. Tanaka, K. Toi, A. Weller, M. Yoshinuma, Y. Narushima, N. Ohno, T. Okamura, N. Tamura, K. Saito, T. Seki, S. Sudo, H. Tanaka, T. Tokuzawa, N. Yanagi, M. Yokoyama, Y. Yoshimura, T. Akiyama, H. Chikaraishi, M. Chowdhuri, M. Emoto, N. Ezumi, H. Funaba, L. Garcia, P. Goncharov, M. Goto, K. Ichiguchi, M. Ichimura, H. Idei, T. Ido, S. Iio, K. Ikeda, M. Irie, A. Isayama, T. Ishigooka, M. Isobe, T. Ito, K. Itoh, A. Iwamae, S. Hamaguchi, T. Hamajima, S. Kitajima, S. Kado, D. Kato, T. Kato, S. Kobayashi, K. Kondo, S. Masamune, Y. Matsumoto, N. Matsunami, T. Minami, C. Michael, H. Miura, J. Miyazawa, N. Mizuguchi, T. Morisaki, S. Morita, G. Motojima, I. Murakami, S. Muto, K. Nagasaki, N. Nakajima, Y. Nakamura, H. Nakanishi, H. Nakano, K. Narihara, A. Nishimura, H. Nishimura, K. Nishimura, S. Nishimura, N. Nishino, T. Notake, T. Obana, K. Ogawa, Y. Oka, T. Ohishi, H. Okada, K. Okuno, K. Ono, M. Osakabe, T. Osako, T. Ozaki, B.J. Peterson, H. Sakaue, M. Sasao, S. Satake, K. Sato, M. Sato, A. Shimizu, M. Shiratani, M. Shoji, H. Sugama, C. Suzuki, Y. Suzuki, K. Takahata, H. Takahashi, Y. Takase, Y. Takeiri, H. Takenaga, S. Toda, Y. Todo, M. Tokitani, H. Tsuchiya, K. Tsumori, H. Urano, E. Veshchev, F. Watanabe, T.

Watanabe, T.H. Watanabe, I. Yamada, S. Yamada, O. Yamagishi, S. Yamaguchi, S. Yoshimura, T. Yoshinaga and O. Motojima, Nucl. Fusion **49**, 104015 (2009).

[4] N. Ohyabu, A. Komori, H. Suzuki, T. Morisaki, S. Masuzaki, H. Funaba, N. Noda, Y. Nakamura, A. Sagara, N. Inoue, R. Sakamoto, S. Inagaki, S. Morita, Y. Takeiri, T. Watanabe, O. Motojima, M. Fujiwara and A. Iiyoshi, J. Nucl. Mater. **266-269**, 302 (1999).

[5] N. Ohyabu, Y. Narushima, Y. Nagayama, K. Narihara, T. Morisaki, A. Komori and LHD Experimental Group, Plasma Phys. Control. Fusion **47**, 1431 (2005).

[6] Y. Narushima, K.Y. Watanabe, S. Sakakibara, K. Narihara, I. Yamada, Y. Suzuki, S. Ohdachi, N. Ohyabu, H. Yamada, Y. Nakamura and the LHD Experimental Group, Nucl. Fusion **48**, 075010 (2008).

[7] K. Ichiguchi, J. Plasma Fusion Res. SERIES, **5**, 491 (2002).

[8] S. Sakakibara, K. Y. Watanabe, H. Yamada, Y. Narushima, K. Toi, S. Ohdachi, T. Yamaguchi, K. Narihara, K. Tanaka, T. Tokuzawa, K. Ida, O. Kaneko, K. Kawahata, A. Komori and the LHD Experimental Group, Plasma and Fusion Res. **1**, 003 (2006).

[9] K. Ichiguchi, N. Nakajima, M. Wakatani, B. A. Carreras and V. E. Lynch, Nucl. Fusion **43**, 1101 (2003).

[10] K. Ichiguchi and B. A. Carreras, J. Plasma Fusion Res. SERIES, **6**, 589 (2004).

[11] A. Ishizawa and N. Nakajima Phys. Plasmas **17**, 072308 (2010).

[12] T. Unemura, S. Hamaguchi and M. Wakatani, Phys. Plasmas **11**, 1545 (2004).

[13] L. Garcia, B. A. Carreras, V. E. Lynch, M. A. Pedrosa and C. Hidalgo, Phys. Plasmas **8**, 4111 (2001).

[14] L. Garcia, B. A. Carreras, V. E. Lynch and M. Wakatani, Nucl. Fusion **43**, 553 (2003).

[15] H. R. Strauss, Plasma Phys. **22**, 733 (1980).

[16] R. Chodura and A. Schlüter, J. Comput. Phys. **41** 68 (1981).

[17] T.C. Hender, B.A. Carreras, L. Garcia and J.A. Rome, J. Comput. Phys. **60** 76 (1985).

[18] A.H. Reiman and H. Greenside, Comput. Phys. Commun. **43**, 157 (1986).

[19] W. Park, D. A. Monticello, H. Strauss, and J. Manickam, Phys. Fluids **29** (4), 1171 (1986).

[20] K. Harafuji, T. Hayashi and T. Sato, J. Comput. Phys. **81**, 169 (1989).

[21] Y. Suzuki N. Nakajima, K.Y. Watanabe, Y. Nakamura and T. Hayashi, Nucl. Fusion **46**, L19 (2006).

[22] K. Ichiguchi, N. Nakajima, M. Okamoto, N. Ohyabu, T. Tatsuno, M. Wakatani and B. A. Carreras, J. Plasma Fusion Res. SERIES, **2**, 286 (1999).

[23] K. Ichiguchi, M. Wakatani, T. Unemura, T. Tatsuno and B. A. Carreras, Nucl. Fusion **41**, 181 (2001).

[24] Y. Nakamura, T. Matsumoto, M. Wakatani, S. A. Galkin, V. V. Drozdov, A. A. Martynov, Yu. Yu. Poshekhonov, K. Ichiguchi, L. Garcia, B. A. Carreras, C. Nührenberg, W. A. Cooper, J.L. Johnson, J. Comput. Phys. **128**, 43-57 (1996).

[25] S. Sakakibara, K. Y. Watanabe, S. Ohdachi, Y. Narushima, K. Toi, K. Tanaka, K. Narihara, K. Ida, T. Tokuzawa, K. Kawahata, H. Yamada, A. Komori and the LHD Experimental Group, Fusion Sci. Technol. **58**, 176 (2010).

[26] S. P. Hirshman, W. I. van RIJ, P. Merkel Comput. Phys. Commun. **43**, 143-155 (1986).

[27] G. Bateman, MHD Instabilities MIT, Cambridge, MA, 1978.

[28] M. Wakatani, Stellarator and Heliotron Devices (Oxford University Press, New York, 1998), p. 98.

[29] R. Kanno, T. Hayashi and M. Okamoto, Nucl. Fusion **45**, 588 (2005).

[30] H. Yamada, K.Y.Watanabe, S. Sakakibara, Y. Suzuki, S. Ohdachi, M.Kobayashi, H. Funaba and the LHD Experimental Group, Contrib. Plasma Phys. **50**, 480 (2010).

[31] F. Watanabe, K. Toi, S. Ohdachi, S. Sakakibara, S. Morita, K. Narihara, Y. Narushima, T. Morisaki, C. Suzuki, K. Tanaka, T. Tokuzawa, K.Y. Watanabe and the LHD Experimental Group, Nucl. Fusion **48**, 024010 (2008).

[32] K. Ichiguchi, Y. Nakamura, M. Wakatani, N. Yanagi and S. Morimoto, Nucl. Fusion **29**, 2093 (1989).

List of Publication

[1] Kinya Saito, Katsuji Ichiguchi and Nobuyoshi Ohyabu
"Interaction between static magnetic islands and interchange modes in a straight heliotron plasma with high resistivity"
Physics of Plasmas, Volume **17** 062504 (2010).

[2] Kinya Saito, Katsuji Ichiguchi and Ryuichi Ishizaki
"Effect of parallel diffusion of equilibrium pressure on interaction between interchange mode and static island"
Plasma and Fusion Research, Volume **6** 2403072 (2011).

[3] Kinya Saito, Katsuji Ichiguchi and Ryuichi Ishizaki
"Low beta MHD equilibrium including a static magnetic island for reduced MHD equations in a straight heliotron configuration"
Submitted to Plasma and Fusion Research.

[4] Kinya Saito, Katsuji Ichiguchi and Ryuichi Ishizaki
"Numerical calculation of MHD equilibria including static magnetic islands in a straight heliotron configuration by means of a field line tracing method"
Plasma and Fusion Research, Volume **7** 2403032 (2012).

[5] Kinya Saito, Katsuji Ichiguchi and Ryuichi Ishizaki
"Effects of static magnetic island on resistive interchange mode in a straight heliotron plasma"
to be submitted to Plasma and Fusion Research.